Subsystem Design in Aircraft Power Distribution Systems using Optimization

Sriram Chandrasekaran
Chairman: Dr. D. K. Lindner
The Bradley Department of Electrical and Computer Engineering

ABSTRACT

The research reported in this dissertation focuses on the development of optimization tools for the design of subsystems in a modern aircraft power distribution system. The baseline power distribution system is built around a 270V DC bus. One of the distinguishing features of this power distribution system is the presence of regenerative power from the electrically driven flight control actuators and structurally integrated smart actuators back to the DC bus. The key electrical components of the power distribution system are bidirectional switching power converters, which convert, control and condition electrical power between the sources and the loads. The dissertation is divided into three parts.

Part I deals with the formulation of an optimization problem for a sample system consisting of a regulated DC-DC buck converter preceded by an input filter. The individual subsystems are optimized first followed by the integrated optimization of the sample system. It is shown that the integrated optimization provides better results than that obtained by integrating the individually optimized systems.

Part II presents a detailed study of piezoelectric actuators. This study includes modeling, optimization of the drive amplifier and the development of a current control law for piezoelectric actuators coupled to a simple mechanical structure.

Linear and nonlinear methods to study subsystem interaction and stability are studied in Part III. A multivariable impedance ratio criterion applicable to three phase systems is proposed. Bifurcation methods are used to obtain global stability characteristics of interconnected systems. The application of a nonlinear design methodology, widely used in power systems, to incrementally improve the robustness of a system to Hopf bifurcation instability is discussed.

ACKNOWLEDGEMENTS

I would like to express my sincere gratitude to Dr. D. K. Lindner for being my advisor and serving as chairman of my doctoral committee. He has been an invaluable source of guidance, encouragement and support during my tenure as his student. I am indebted to Dr. Dushan Boroyevich for always willing to help, guide, motivate and challenge me at every stage of my work. I am grateful to Dr. Zafer Gurdal for his help and guidance as part of the AFOSR project.

I thank Dr. F.C. Lee for giving me an opportunity to work in CPES. I am grateful to Dr. William Baumann, Dr. Ali Nayfeh and Dr. Bob Rogers for serving on my doctoral committee.

Sincere thanks are due to Scott for significantly contributing towards obtaining the optimization results. In addition to being an excellent colleague he has been a great friend. I am grateful to Sergio and Kostya for their help and input while working on the AFOSR project. I thank my roommate my Gandhi for his friendship and all the good times we shared while we were at Tech.

I thank all my friends and colleagues in the lab for providing a wonderful working atmosphere in the lab. Over the past five years, I have been lucky to have found such great friends in Teresa, Matt, Carlos, Dimos, Francisco, Peter, Eric, Kevin, Johan, Alex, Nikola, Ivan, Sergio, Sam, Christophe, Christelle, Kalyan and Naveen to name only a few. I will always cherish the great times we shared while working together.

Finally, I would like to thank my parents, brother, sister-in-law and my two little nephews for their love, patience and support during my stay at Blacksburg.

The research reported in this dissertation was supported by the AFOSR under grant numbers F49620-97-1-0254 and made use of ERC Shared Facilities supported by the National Science Foundation under Award Number EEC-9731677.

To my dear friend, Jigna

TABLE OF CONTENTS

LIST OF FIGURES

LIST OF TABLES

1 INTRODUCTION

The research reported in this dissertation is concerned with systems related to the distribution and utilization of electrical power in power distribution systems of next generation aircraft. It is projected that in next generation transport aircraft, all power (except propulsion) will be distributed and processed electrically. In other words, electrical power will be utilized for driving aircraft subsystems currently powered by hydraulic, pneumatic or mechanical means including utility and flight control actuation, environmental control system, lubrication and fuel pumps, and numerous other utility functions. In addition, modern aircraft are also equipped with electrically driven, structurally integrated smart actuators that are used for active vibration control of wing surfaces in order to reduce fatigue and mechanical wear and tear. These concepts are embraced by what is known as the "More Electric Aircraft (MEA)" initiative. The MEA emphasizes the utilization of electrical power as opposed to hydraulic, pneumatic, and mechanical power for optimizing aircraft performance and life cycle cost. For example, hydraulically driven actuators would be replaced by electric motor driven pumps, and a pneumatically driven compressor for environmental control would be replaced by an electric motor driven compressor. Some expected benefits of moving to an MEA or "Power-By-Wire" secondary power systems are listed below:

Reduced design complexity
Fewer design components
Smaller certification workload
Lower flight test hours
Reduced procurement workload
Lower total component/system cost
Reduced parts count
Less tooling
Reduced production labor
Shorter checkout time
Less ground support equipment
Higher system reliability
Less spared inventory
Easier aircraft modification
Enhanced safety
Less environmental impact

Increasing use of electric power is seen as direction of technological opportunity for aircraft power systems based on rapidly evolving advancements in power electronics, fault tolerant electrical power distribution systems and electrically driven primary flight control actuator systems. The decision to convert to electrically driven subsystems depends on the overall cost and performance benefits. Thus reliable, high power density motors and motor drives with power ratings ranging from a few horsepower to hundreds of horsepower will be required. More importantly, the magnitude, quality, reliability, and fault tolerance of the electric power to be generated and distributed in the aircraft must be significantly greater than what the present state-of-the-art technology can provide. The aircraft power distribution system hence, plays a central role in the developing concepts of "Power-by-Wire" and "More Electric Aircraft". The MEA will need a highly reliable, fault tolerant, autonomously controlled electrical power system to deliver high quality power from the sources to the load.

For the purposes of this research, a baseline power distribution system architecture for a typical next generation transport aircraft was developed in collaboration with Lockheed Martin Control Systems. The proposed power distribution system is built around a 270V DC distribution bus. The key electrical subsystems in the baseline system are bidirectional power converters, which are responsible for the conversion, control and conditioning of electrical power between the sources and the loads. One of the distinguishing features of these power distribution systems is that, some of the loads such as flight control and smart actuators are capable of providing energy back to the power distribution system. The phenomenon of regenerative power represents a significant departure from the current state-of-the-art concepts in that, the power distribution system must be designed to allow for power flow in both the forward direction from the generator to the loads and in the reverse direction from the loads to other loads and the generator. In general, the process of regeneration can be characterized either as a transient disturbance on the DC bus or as a sustained oscillatory load disturbance. It would appear that regenerative power is a positive feature of a DC power distribution system because it would make more power available to the system, and/or it would increase the efficiency of the system. However, if the power distribution system is not designed to accept this power, the effects can be quite detrimental. The regenerative power can result in unacceptably high transient voltage swings or undesirable distortion due to the oscillatory load disturbances. These voltage disturbances on the bus can cause damage to other components designed to operate within set voltage limits (Mil Spec 704E) [1].

The principal objective of the proposed research effort is to develop optimization methods to facilitate the design of subsystems in next generation aircraft power distribution systems. Since the presence of regenerative energy from flight control actuators is a unique feature, it is critical that these optimization methods include an accurate characterization of the regenerative energy from the flight control actuators in order to account for their effects on the performance of the power distribution system. The concept of the "More Electric Aircraft" has been in existence for a little less than a decade, and a considerable amount of research effort has been devoted to the development of advanced technologies in power electronics, motor drives, actuation systems and generating equipment. However, design methodologies to appropriately integrate the different subsystems together and control their interactions have not received much attention. The research reported in this dissertation represents a step in this direction.

In summary, the use of optimization methods is demonstrated for the design of an interconnected system consisting of an input filter and a regulated DC-DC buck converter (called the sample system) and for the design of the drive amplifier for a piezoelectric actuator. The formulation of the optimization problem consists of model development, identification of design variables, definition of the optimization constraints and the objective function. The optimization formulation uses linear analysis methods to guarantee internal stability of individual systems and stability of the interconnected system. However, due to the nonlinear nature of the systems in the aircraft power distribution system, linear techniques provide on local stability information. Hence, a significant amount of effort has been devoted to the study of nonlinear stability and subsystem interaction analysis methods.

1.1 Scope of the Dissertation

This dissertation is essentially divided into three main parts. The scope of the research described in each of the three parts is described below.

1.1.1 Optimization of the Sample System

Part I focuses on the development of an optimization methodology for the design of a simple interconnected system called the sample power system which consists of an EMI input filter followed by a regulated DC-DC buck converter. The sample system is arrived at by simplifying the detailed model of an Electromechanical Actuator (EMA) drive controlling the spoiler surfaces of the aircraft. The origin and nature of regenerative power in the EMA drive are identified. The regenerative process is then equivalently represented in the sample system as a transient load disturbance on the buck converter. The buck converter is also loaded by a constant DC current to represent the steady state power drawn by the actuator. The optimization methodology developed, however, is quite general in that it can be extended with minor modifications to other subsystems in the power distribution system.

The approach followed here is to begin with the development of an optimization methodology for the individual subsystems of the sample system. The models of the individual subsystems account for the interactions with the other subsystems in the global system. Therefore, the methodology optimizes the performance of the local subsystems while accounting for global interactions. When the subsystems are considered jointly, the optimization formulations for each subsystem are such that they can be combined in a straightforward way to obtain an optimization methodology for the combined system. Applying this approach to the sample system, an optimization methodology is first formulated for the input filter. This methodology is then extended to the regulated DC-DC buck converter, taking into account the increase in complexity of the converter. The procedure is then extended to the sample system as a whole to address system wide design considerations. Stability of the global system is insured, and the effects of regenerative power flow are minimized. It is shown that optimizing the integrated system as a whole results in a lesser weight than integrating the individually optimized systems.

1.1.2 Piezoelectric actuators

The use of smart actuators in next generation aircraft has received increasing attention in the last few years. These actuators are built around so-called "smart materials." These materials include piezoelectric and electrostrictive materials that change their shape in response to an electric field, magnetorestrictive materials that change their shape in response to a magnetic field, and shape memory alloys that change their shape in response to heat. These materials have garnered some interest because they offer the possibility of solid state induced-strain actuators with the attendant benefits of high energy density and reliability. These actuators are of direct interest to this proposed research effort because the smart materials support bidirectional power flow.

The study of smart actuators in this research effort is limited to piezoelectric actuators used for active vibration control of aircraft surfaces. The study is motivated by the application of piezoelectric actuators for alleviating the "tail buffeting" problem in a twin tail aircraft [24]. The buffet loads acting on the tail surface cause excessive wear and tear that significantly reduce the lifetime of the aircraft and increase repair and maintenance costs. Piezoelectric actuators mounted at the root of the tail and on the surface are controlled to actively suppress the effect of the buffet loads on the tail surface. To this end, a substantial amount of work has been done in the field of modeling and control of piezoelectric actuators.

A detailed electromechanical model of a piezoelectric stacked actuator has been developed. This model can be directly coupled to a mechanical structure for active control of the structure. The model of the actuator consists of an anhysteretic nonlinearity between the polarization and the electric field. A simple mass-spring-damper system acted on by an external disturbance force is used as the mechanical structure coupled to the actuator.

A well defined optimization procedure is formulated for the design of a current controlled amplifier driving a piezoelectric actuator. A simple control law that requires the amplifier to drive a given reference current to be driven into the actuator is assumed.

The external disturbance force acting on the mechanical structure is assumed to be zero. A full bridge DC-AC inverter with an inductor on the AC side is chosen as the topology of the drive amplifier. The optimization formulation is used to determine the value of the inductance including its physical design and the DC bus voltage for a given switching frequency. A computationally inexpensive frequency domain technique is used to determine the switching ripple in the actuator current.

Finally, a novel current control law to actively damp the mechanical structure is proposed. This control law requires the current through the actuator to be proportional to the acceleration of the structure. As a result of this control law, the actuator acts as a energy sink in absorbing the real mechanical power fed to the structure from the external disturbance force and redirecting it back to the electrical source. Hence, there is a net flow of real electrical power from the actuator back to the DC bus. In addition, due to the capacitive nature of the actuator a significant amount of reactive power circulates between the actuator and the drive amplifier. A detailed frequency domain analysis of the closed loop performance of the system is presented. This includes a detailed description of the electromechanical power transfer characteristics between the actuator and the electrical source, namely the current controlled amplifier. The anhysteretic nonlinearity in the actuator is, however, neglected in this analysis in order to exemplify the dependence of the power flow characteristics on the parameters of the system. Guidelines to design the drive amplifier based on the peak voltage and the current requirements of the actuator are presented.

1.1.3 Subsystem Interaction & Stability Analysis

One of critical operational requirements of the power distribution system is the stability and robustness of the subsystems. The optimization methodology used to design subsystems includes constraints, which guarantee the stability of individual subsystems. In addition to ensuring the stability of individual subsystems, it is necessary to guarantee minimal interaction between interconnected subsystems and avoid unstable operation due to the integration of subsystems. The optimization formulation of the sample system described in Part I of the dissertation use the linear stability constraints to guarantee the internal stability of subsystems. The classical Middlebrook impedance ratio criterion is used to ensure stability of interconnected subsystems by requiring that the terminal impedances of the individual subsystems at the interconnection be sufficiently separated.

However, if the optimization methodology presented is to be extended to three phase systems and interfaces in the power distribution system, criteria that guarantee internal stability of each subsystem and minimal interaction between them need to be used. In addition, since a majority of the subsystems in the power distribution system are nonlinear, linear stability analysis techniques only guarantee stability in a small neighborhood of the equilibrium point. The third part of the dissertation is hence, devoted to development of linear and nonlinear stability analysis techniques that investigate local and global stability of subsystems.

The impedance ratio criterion is extended to a multivariable setting to make it applicable to three phase and single-phase AC interfaces. The multivariable impedance ratio criterion is defined in terms of the singular values of the terminal impedance matrices at the interconnection. The multivariable criterion is demonstrated in the study of the interaction between a three phase input filter and a three phase boost rectifier. This criterion, however, is based on linearized models and can only guarantee local stability.

Since regenerative power is quite a salient performance characteristic of the power distribution system, it is necessary to determine the stability of regulated power converter systems under the regenerative energy flow conditions. A simplified analysis is presented that proves that the stability of an interconnected system consisting of a regulated power converter and an input filter is unaffected if the load current, in steady state, is flowing in the reverse direction towards the source. Hence, it is more critical to guarantee stability in the forward direction of power flow than in the reverse direction.

Since linear analysis methods provide only local stability information in a small neighborhood of the equilibrium point and cannot predict the behavior the system under large signal disturbances, bifurcation methods are used to obtain information about the global stability behavior of the system. Bifurcation analysis techniques provide information about the nature, stability and multiplicity of the solutions of the system as a function of a bifurcation parameter. Specifically, bifurcation methods to study the interaction between an input filter and a regulated DC-DC buck converter and at the DC bus between a bus regulator and a regulated load converter system. The converters used in the bifurcation analyses are represented by their average models in order to study the low frequency system level stability properties. An extensive body of published research is available on the nonlinear stability of analysis of power converters at the switching frequency scale. However, these methods, when extended to the study of more complex systems and subsystem interactions become computationally untenable and lose practical utility and hence, are not pursued in this research. These bifurcation methods, despite providing information about the global stability characteristics of the system, are not immediately applicable to a design procedure and hence an optimization formulation.

To this end, a simple design methodology based on bifurcation methods and widely used in the field of utility power systems, is investigated. This design procedure involves the determination of an optimal direction of updating the design variables of a system such that potential instabilities due to bifurcations are avoided. A simple DC-DC boost converter, represented by its average model, with a multiloop controller is used to demonstrate this design methodology.

1.2 LITERATURE REVIEW

More Electric Aircraft

The More Electric Aircraft initiative was formally conceived in 1991 by the Air Force by the (1) Power Management and Distribution for the More Electric Aircraft program. This triggered intense research in the areas of power generation, transmission, distribution and utilization in the More Electric Aircraft [2,3]. Potential starter/generator technologies based on synchronous generator and switched reluctance machines were studied [4-8]. The architecture of the power distribution system, the nature of the distribution bus, whether it would be AC or DC, was studied in detail under the MADMEL program [9-12]. The development of advanced power electronic devices and converter technologies was pursued [13-17]. Actuator technologies based on advanced power electronics drives such as switched reluctance and induction motor drives were proposed to replace the pneumatic and hydraulic actuators in the present generation aircraft [18,19].

Optimization of DC Power Distribution Systems

The optimization of power electronic converters has received considerable attention in the past years. An abundance of literature exists on the optimization of switching power converters, a few of which are [20,21,22]. However, there has not been must published work on the subject of optimization of power distribution systems. In [23], an optimization-based approach was proposed for the design of an aircraft or space based power distribution system that minimized mass and hence monetary cost. The optimum voltage and power levels are various points of the power system were determined. However, the individual design of the power system components was not included in the analysis.

Piezoelectric Actuators

The study of piezoelectric actuators in this dissertation is motivated by the application of piezoelectric actuators for alleviating the "tail buffeting" problem in a twin tail aircraft [24]. The use of switching power amplifiers for driving piezoelectric actuators was discussed in [25-30]. High voltage switching amplifiers for piezoelectric actuators are discussed in [25,26]. The switching amplifiers for electrostrictors are reported in [27]. It has been noted that charge and current controlled amplifiers naturally reduce the distortion induced by the nonlinearities of the piezoelectric actuator [30,31]. A similar result for electrostrictor actuators has been reported in [28,29]. Optimization of drive electronics for piezoelectric actuators was addressed in [32]. However, a well-defined optimization procedure that takes into account the nonlinear characteristics of the actuator and yields physically meaningful designs of the individual components of the amplifier has not been proposed. The optimization formulation presented in this dissertation is a first step in this direction.

The analysis of power flow through the amplifier and actuator has been discussed by [28,29,33,34]. In was shown in [33] that actively damping the structure with a controlled piezoelectric actuator causes the mechanical power injected into the structure by the external disturbance source to be absorbed by the structure and funneled to the electrical source. We present similar results in a more general setting that show that the electrical power at the actuator terminals has a negative real component, which indicates that the actuator feeds electrical power back to the source. In [34], the open loop power flow between a linear amplifier and a piezoelectric actuator under the condition that the displacement of the structure is constant is discussed. The closed loop power flow between a switching amplifier and an electrostrictor actuator off-resonance is discussed in [28]. An analysis of the coupled electromechanical power flow between piezoceramic actuators and mechanical structures was presented in [35]. The use of impedance matching techniques to maximize the energy efficiency of the coupled mechanical system has been discussed in [28, 36].

Subsystem Interaction and Stability Analysis

The first studies on subsystem interaction in systems with power converters addressed the interaction between an input filter and a regulated power converter [37,38]. The methods proposed in these papers were based in linear analysis techniques that worked on small signal models of nonlinear systems linearized around a steady state operating point. The widely used impedance ratio criterion was proposed in [37]. This was extended to address input filter interaction in DC-DC converters based on various control strategies in [39-42]. However, very little effort was devoted to the study of input filter interaction in three phase AC-DC rectifiers where the system is multivariable in nature. A preliminary study was performed in [43], but the results presented therein were not applied to three phase AC-DC converters in general. In [44], a reduced order model for the three-phase rectifier was found and interaction was studied based on the same. The design of input filters for power factor correction circuits was introduced in [45]. The factors affecting the choice of the filter topology for power factor correction circuits were outlined. In [46], the three-phase converter was treated as a multivariable system and criteria for the stability of the interconnected filter-converter system were derived.

based on the eigenvalue loci and singular values of the relevant transfer function matrices. However, the analysis presented in [46] did not clearly identify the effects of the inclusion of the input filter on the performance indices of the system. A detailed analysis of the multivariable problem was conducted as part of this research and an extended impedance ratio criterion based on the singular values of the impedance matrices of the interconnected subsystems is proposed.

The stability analysis of distributed power systems was addressed in [46,49,50,51]. In [49], the impedance ratio criterion was used to ensure the local stability of the power distribution system. [52] presented the development of a hardware testbed to analyze subsystem interaction in shipboard power distribution systems. Nonlinear analysis methods for stability study were introduced in [50,51,53]. Bifurcation methods were predominantly used for stability analysis in these references.

1.3 ORGANIZATION OF THE DISSERTATION

The organization of the dissertation is as follows:

Part I consisting of Chapter 2 and 3, deals with the development of the optimization methodology for the sample system. The baseline power system architecture is introduced in Chapter 2. The origin and nature of regenerative power from flight control actuators is briefly discussed. A detailed model of the EMA is simplified to an interconnected system consisting of a DC-DC buck converter preceded by an EMI input filter. This is used as the sample system for the optimization methodology in Chapter 3.

The development of the optimization methodology for the sample system is presented in Chapter 3. The sample system consists of a regulated DC-DC buck converter preceded by an EMI input filter. The regenerative process is modeled as a transient load disturbance at the output of the buck converter. The optimization formulation of the input filter is described first. The identification of the design variables, definition of the constraints and the objective function are explained in detail.

This is followed by the optimization formulation for the design of the buck converter. The individual optimization methodologies are combined to yield the optimization formulation for the sample system. It is shown that optimizing the integrated system as a whole results in a lesser weight than integrating the individually optimized systems.

Part II of the dissertation deals with the modeling, optimization and control of the piezoelectric actuator. A detailed electromechanical model of the actuator coupled with a simple mechanical structure is developed in Chapter 4. The model includes the anhysteretic nonlinearity between the polarization and the electric field in the actuator.

The development of the optimization methodology for the design of a current controlled amplifier is discussed in Chapter 5. A simple control law requiring the amplifier to synthesize the given reference current into the actuator is assumed. The optimization formulation is used to determine the DC bus voltage and the physical design of the inductor. Optimization results are presented to illustrate the effectiveness of the proposed methodology.

Chapter 6 presents a control law, wherein actuator is used for actively damping the mechanical structure. The current flowing in the actuator is controlled to be proportional to the acceleration of the structure. A detailed analysis of the mechanical power flow between the actuator and the amplifier is presented. Guidelines to design the current controlled amplifier based on the peak current and voltage in the actuator are proposed.

Part III of the dissertation is devoted to development of techniques for the analysis of stability and interaction between interconnected subsystems. The interaction between a three phase input filter and a three phase boost rectifier is studied in Chapter 7. A multivariable impedance ratio criterion based on the singular values of terminal impedances is then proposed to guarantee stability and minimal interaction. Simplifying approximations that lend the criterion to physical insight are presented.

The discussion in Chapter 8 deals with the integrated stability analysis of a regulated power converter with an input filter under bidirectional power flow. The converter is modeled as a constant power load and a simplified but insightful analysis of stability is presented. It is shown that the forward direction of power flow is more critical to the stability of the system than the reverse direction.

The use of bifurcation methods to obtain global stability information about integrated systems is described in Chapter 9. Specifically, the interaction between an input filter and a regulated DC-DC buck converter and that between the bus regulator and a load converter in a simplified power system are presented. The results are compared with those obtained from linear analysis methods and their implications on the design of these subsystems are discussed.

A nonlinear design methodology, founded in the field of power systems, is applied, in Chapter 10, to incrementally improve the robustness of a nonlinear system by directing the system away from the onset of instability through a bifurcation. The method is demonstrated using the example of a regulated DC-DC boost converter. The potential incorporation of this design technique to an optimization formulation is discussed.

Conclusions and suggestions for further research are provided in Chapter 11.

PART I

OPTIMIZATION OF SAMPLE SYSTEM

2 BASELINE POWER SYSTEM ARCHITECTURE

2.1 INTRODUCTION

In this chapter, the baseline architecture of the power distribution system is described. The power distribution system is based on the proposed next generation 270V DC bus. The Electromechanical (EMA) and Electrohydraulic (EHA) actuators have been specifically developed for use with this type of DC power distribution system under the More Electric Aircraft initiative. This architecture also includes smart actuators, which consist of piezoelectric patches embedded or attached to the aircraft structure. The key electrical components of the power distribution system are bidirectional power converters for the conversion, control and conditioning of electrical power. One of the distinguishing features of this power distribution system is the regeneration of energy back to the electrical source from flight control actuators under certain operating conditions. This phenomenon of regeneration represents a significant departure from current power distribution systems where the power is allowed to flow only in one direction from the generator to the loads.

The baseline power system is introduced in section 2.2. The actuation loads namely the EMA and the EHA are described briefly in section 2.3. A brief description of the origin and nature of regenerative energy based on the EMA is presented in section 2.4. The detailed model of the EMA is then simplified to arrive at the sample system consisting of a regulated DC-DC buck converter preceded by an input filter in section 2.5. The regenerative process is represented as a transient load disturbance on the buck converter. The operating conditions of the sample system and a brief description of the models used for the filter and the converter are described.

2.2 BASELINE POWER DISTRIBUTION SYSTEM

The baseline power distribution system architecture was developed jointly with Lockheed Martin Control Systems (LMCS) and the following specifications were agreed upon:

1. *270 V DC* power bus with a *270 V* battery
2. Two Engine Starter/Generators (*500 kW* each) with Split/Parallel Bus
3. APU Channel Starter/Generator (*200 kW*)
4. Smart Load Management
5. Loads
   - Electric Actuation
   - Cargo Bay Pressurization
   - Negative Impedance Avionics Loads
   - Environmental Control System

The characteristics of aircraft electric loads in a typical commercial transport aircraft are given in Table 2.1.

Table 2.1. Characteristics of Aircraft Electric Loads

Load Group	**Characteristics of the Load**	**Percentage of Total Load**
Motor (ECS, Pumps)	• Mainly squirrel-cage induction motor at present. Brushless DC motor with power converter will compete with the induction motor • Fixed Frequency ac or dc with power converter; coarsely regulated, insensitive to waveform and transients for ac induction motor • Power Flow is bidirectional	Represents the largest portion of aircraft electrical loads
Heating	• Constant voltage ac;constant or variable frequency, or dc;tolerate low quality, coarsely regulated power • Power Flow in one direction	Represent large segment of electric loads in commercial transports
Lighting	• Incandescent lamps prefer low voltage ac or dc;tolerate transients and poor waveform • Power flow in one direction	
Electronics	• Closely regulated, clean dc or ac; input power ultimately transformed to low voltage dc for utilization • Power Flow in one direction	
Control	• Consists of relays, actuators, indicators and some lights and electronics. • Part of this load requires closely regulated power, ac or dc; the remainder can tolerate low quality power • Power Flow of actuator load is bidirectional	Represent a small portion of the total load, usually less than 5% of the total load

Conceptually, this system is shown in Figure 2.1. The power distribution system is built around a dual 270 V/500 kW DC bus with an APU and battery backup auxiliary bus. The starter/generator units generate three-phase AC power at 110V/400Hz. The key electrical components for the regulation of the power bus are the bidirectional power converters (BDC). The BDC between a starter/generator units and the corresponding DC distribution bus serves as the bus regulator converting the 110V/400Hz three-phase AC power to tightly regulated 270V DC in the face of load and source disturbances. Other

BDCs in the system process the power at the DC bus according to the requirements of the corresponding loads.

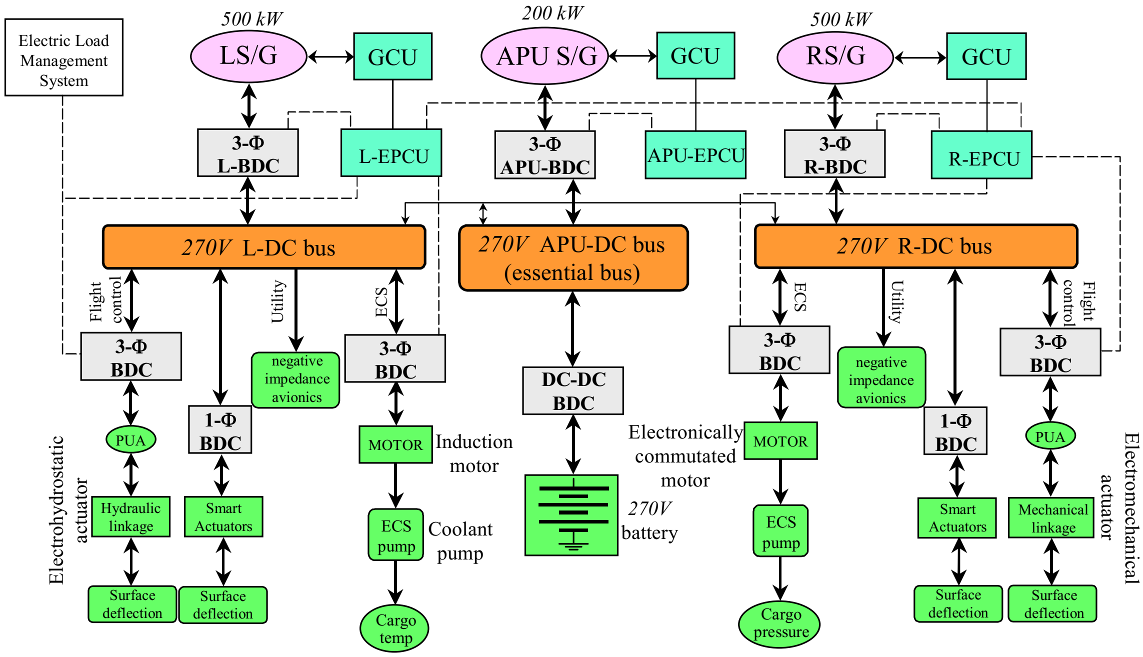

LS/G : Left-Starter Generator	GCU : Generator Control Unit	PUA : Power Unit Actuator
RS/G : Right-Starter Generator	EPCU : Electronic Power Control Unit	ECS : Environmental Control System
APU : Auxiliary Power Unit	BDC : Bidirectional Converter	

Figure 2.1. Baseline Power System Architecture

Models and parameters of EMA and EHA actuators were provided by LMCS. Also included are conventional motor loads associated with the ECS system. Novel piezoelectric actuators are also under consideration. The presence of BDCs represents a significant change in the properties of these next generation power distribution systems in that they transfer power in the forward direction from the generators to the loads and, under certain conditions, in the reverse direction back to the generators when the actuation loads operate in the regenerative mode. The origin and characteristics of this regenerative phenomenon and the consequent effects on the power distribution system are described in the following section.

2.3 ACTUATION LOADS

EHAs and EMAs

Electro-Hydraulic Actuators (EHAs) will drive the primary control surfaces of the airlifter. Two EHAs will drive each surface panel for the elevator, aileron, and flaperon, while three EHAs will drive the rudder. There will be a total of 15 EHAs driving the seven primary flight control surfaces. Figure 2.2 depicts the actuator location for each of the primary surfaces.

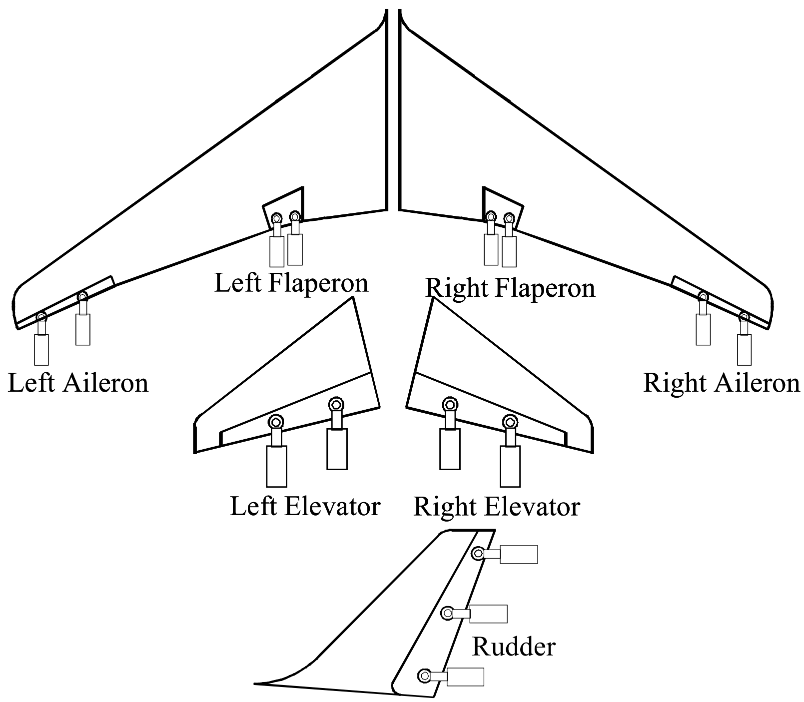

Figure 2.2. Primary Actuator Configuration, EHA

The secondary flight control surfaces consist of 14 spoiler panels. Electro-Mechanical Actuators (EMAs) will drive these panels. Each of these EMAs will have one output shaft connecting to a particular surface panel. This configuration differs from that of the primary surfaces, where two or three separate EHA RAM output shafts connect to the same control surface. Figure 2.3 depicts the secondary control surfaces and their actuator locations.

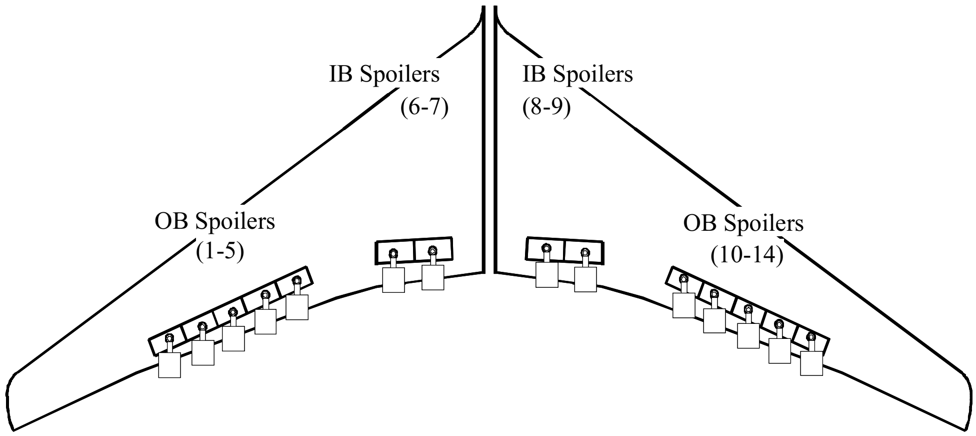

Figure 2.3. Secondary Actuator Configuration, EMA

The operating duty cycles of each of the deflection surfaces, associated hinge moments and power levels in hp are given in Table 2.2.

Table 2.2. Selected Actuator Duty Cycles for Regeneration Study

Flight Phase	**Elevator (EHA) 4 x 10 hp**	**Aileron (EHA) 4 x 10 hp**	**Flaperon (EHA) 4 x 9 hp**	**Rudder (EHA) 3 x 15 hp**	**Outboard Spoiler (EMA) 4 x 6 hp**	**Inboard Spoiler (EMA) 10 x 6 hp**	
Bypass Test on Ground	-15 to +10	+10 to – 10	-10 to +10	-15 to +10			Surface Deflection (deg)
	+210 to - 220	-230 to +230	-60 to +110	+1530 to - 1590			Hinge Moment (ft-lbs)
Control Check on Ground	-30 to +25	+15 to -30	+36 to -10	-25 to +25			Surface Deflection (deg)
	+1670 to – 1750	-90 to +90	+500 to – 1120	-4740 to 4940			Hinge Moment (ft-lbs)
Roll Maneuver		+6 to –9	+24 to +36		0 to +4.5	0 to +1.0	Surface Deflection (deg)
		-990 to – 350	-8520 to – 10420		0 to +154	0 to –324	Hinge Moment (ft-lbs)
Yaw Maneuver		+3 to –5	+30 to –36	-5.5 to +5.5			Surface Deflection (deg)
		-790 to – 510	-9610 to – 10140	+17610 to -14280			Hinge Moment (ft-lbs)
Landing Rollout		-30 to 0	-10 to 0		0 to +45	0 to +60	Surface Deflection (deg)
		+230 to 0	-370 to 0		-5310 to +492	-1035 to +1482	Hinge Moment (ft-lbs)

2.4 REGENERATIVE ENERGY

The operation of EMAs is briefly described in this section to identify the origin and nature of regenerative power from these flight control actuators. A block diagram of an EMA connected to the DC bus is shown in Figure 2.4.

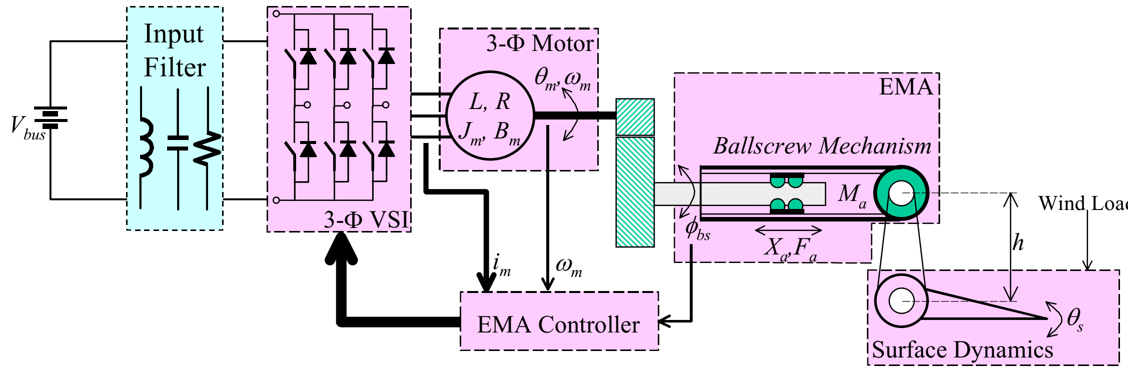

Figure 2.4. Electromechanical actuator system diagram.

The EMA is driven by a three-phase brushless DC or permanent magnet synchronous motor drive. A three-phase DC-AC inverter converts the 270V DC available on the DC bus to the three phase AC voltages required by the drive motor. The DC bus is represented by an ideal 270 V DC source. The inverter is preceded by an EMI input filter to attenuate the switching noise from reaching the DC bus. The control objective is to drive the surface in response to a deflection command θ_{ref} in the presence of a wind load disturbance. The origin of regenerative power is explained in the following.

Typical simulation results for the EMA are shown below in Figure 2.5. To start with, a surface deflection command to drive the surface from zero to a given reference position is issued. In response to this command, the drive motor accelerates the control surface to drive θ_s toward θ_{ref}. Positive values of bus current represent power drawn by the motor and negative values represent power regeneration. During the acceleration, the motor draws a large current. The motor speed steadies at its maximum allowable as the deflection increases linearly in the presence of the wind load. For the simulation results shown in Figure 2.5, the wind load is in the same direction as the motor torque. Hence, in order to maintain the linear surface deflection profile, the EMA controller makes the motor acts as a generator, absorb the energy from the wind load and siphon it back to the DC bus. This is represented by the large negative current at the DC bus.

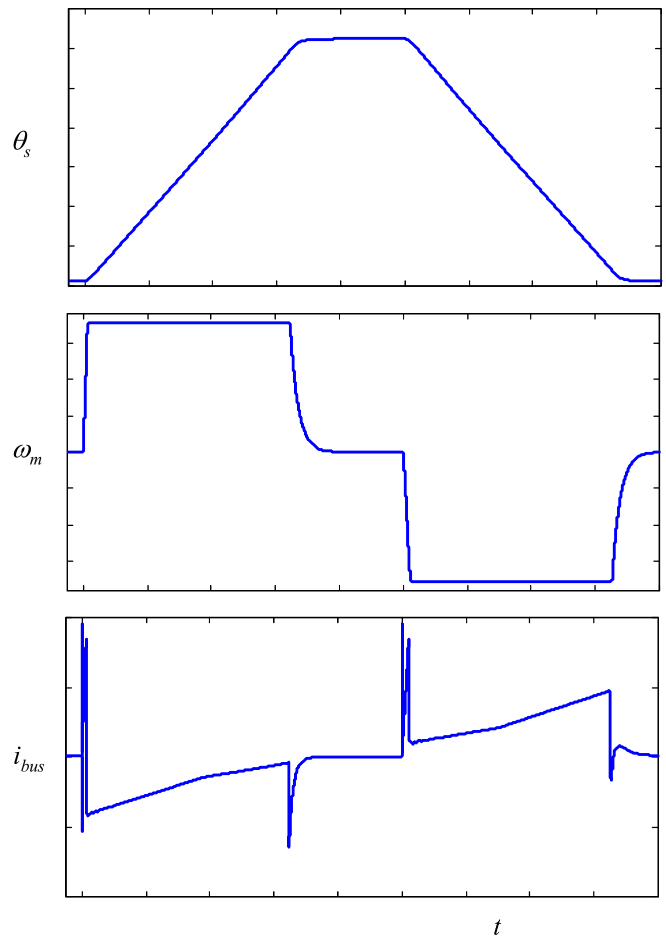

Figure 2.5. Simulation Results of the EMA

As the surface approaches its final commanded position, the motor brakes rapidly. This results in a surge of regenerative energy back to the DC bus as seen by the rapid negative excursion in the bus current. The same sequence of events is repeated when the surface is commanded to return to its original position. The motor accelerates in the opposite direction and the wind load opposes its motion thereby resulting in a large current being drawn from the bus. However, the rapid braking resulting the surge of regenerative energy toward the end of the operating cycle is the same as in the previous case. Hence, it can be seen that the regeneration of energy from these actuators is seen by the DC bus as (1) a slowly varying load disturbance due to the wind load and (2) a fast transient load disturbance due to the braking operation of the drive motor. Typical effects of such a disturbance on a regulated DC bus are transient voltage swings and possible instability. Simulation results are shown in Figure 2.6 to illustrate the transient voltage peaks due to regenerative process.

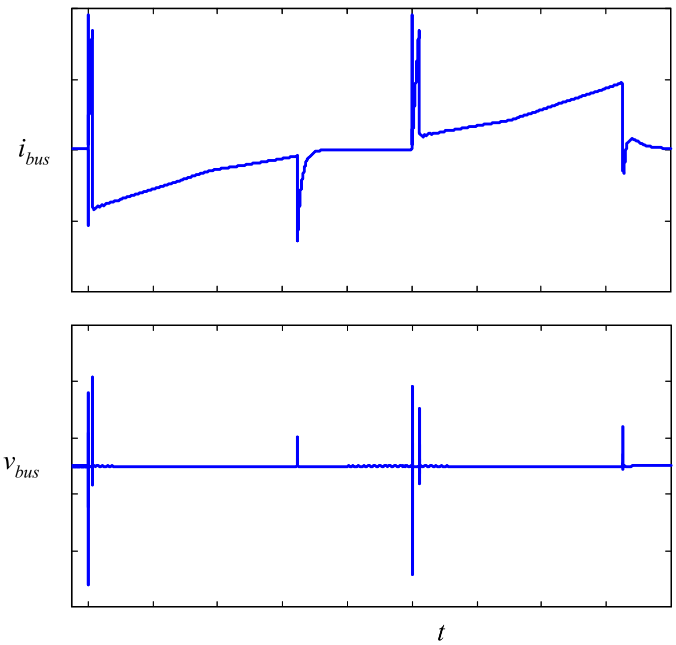

Figure 2.6. DC bus voltage response due to regeneration from EMA

It can be seen that DC bus is almost unaffected by the slow varying regenerative transient but suffers voltage spikes during the acceleration and braking operation of the motor. It is important that the magnitudes of these spikes are limited such that the safe and reliable operation of the other loads connected to the DC bus is not compromised. Limits on the transient voltage excursions on the DC bus are specified in the Mil Std-704E [1]. Hence, it is essential that the magnitude of the voltage spikes be well within these limits. In addition, if the propagation of the regenerative energy through the power distribution system can be clearly understood, methods to utilize the energy can be devised to increase the efficiency of the system.

2.4.1 Electromechanical Actuator Modeling

The EMA is driven by a three-phase brushless DC or permanent magnet synchronous motor drive (Figure 2.4). A three-phase voltage source inverter (VSI) converts the 270V DC available on the DC bus to the three phase AC voltages required by the drive motor. The motor is loaded by the actuator and the control surface as shown in Figure 2.1. The control surface is subjected to the wind load as described in the previous section. A multi-loop controller consisting of motor current, motor speed and actuator position feedback loop is used to control the three-phase inverter. The inverter-motor drive is typically modeled in rotating DQ-coordinates that are synchronized with the rotor position. This modeling approach essentially reduces the motor currents and voltages to DC and the resulting model approximately to that of a DC motor [65]. Consequently, the three phase inverter can be represented by a single phase bidirectional full bridge converter. The load torque on the motor is a function of the parameters of the actuator, the surface dynamics and the wind load acting on the control surface.

It was shown in the previous section that the wind load on the control surface results in a load torque that drives the motor as a generator, which in turn regenerates energy back to the DC bus when the control surface is commanded to move from zero a reference position. The wind load acting on the control surface and the position of the surface are shown in Figure 2.7. The wind load is defined as a function of the position of the control surface. The motor position and the equivalent load torque acting on the motor due to the wind load are shown in Figure 2.8.

From Figures 2.7 and 2.8, it can be seen that the dynamics of the control surface and those of the motor are sufficiently decoupled that positions of the control surface and the motor are linearly related. In addition, if the small transients at the edges of the load torque profile in Figure 2.8 are neglected, it can be assumed that the wind load on the surface and the load torque are linearly related.

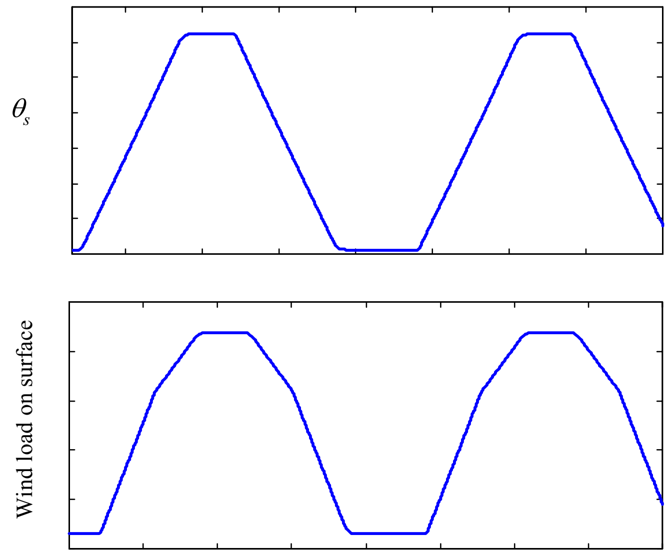

Figure 2.7. Control surface position and wind load

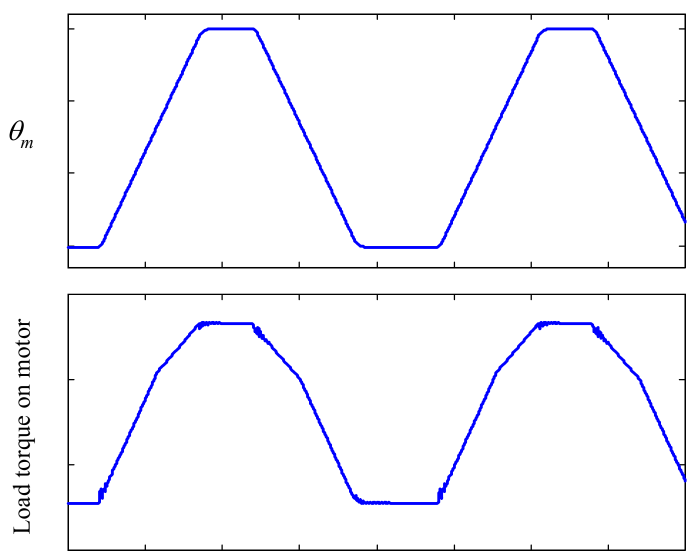

Figure 2.8. Motor position and load torque

Hence, the regenerative process can be captured with reasonable accuracy if the actuator and the dynamics of the control surface can be replaced by a time varying load torque defined as a function of the motor position. This results in considerable simplification of the model of the EMA. The controller of the EMA also needs to be replaced with an appropriate multiloop controller for the motor consisting of motor current, speed and position control loops.

A block diagram of the simplified EMA model with a separately excited DC motor with a load torque and a multiloop controller is shown in Figure2.9.

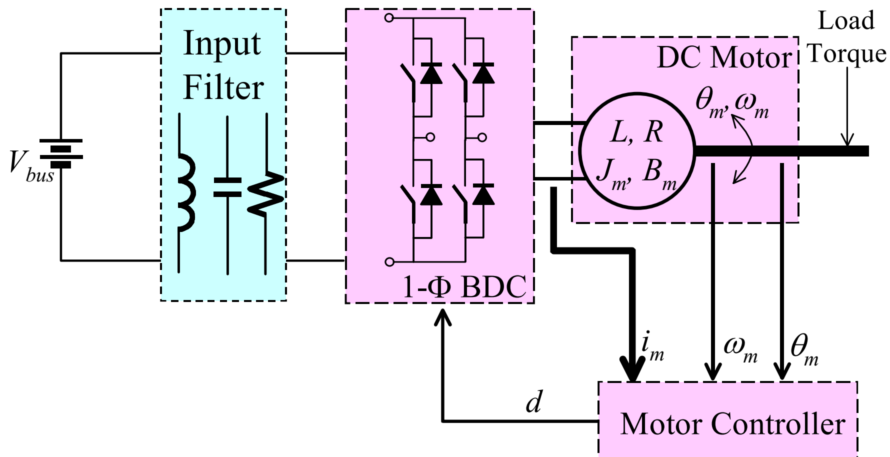

Figure 2.9. Block diagram of simplified EMA model

The dynamic equations of the separately excited DC motor are given below.

$$L_a \frac{di_a}{dt} = -R_a i_a - K_e \omega_m + dV_{bus}$$
$$J \frac{d\omega_m}{dt} = K_t i_a - B_m \omega_m - T_{ex} \tag{2.1}$$
$$\frac{d\theta_m}{dt} = \omega_m$$

where,

v_a - armature voltage,
i_a - armature current,
ω_m - armature angular speed,
T_{ex} - load torque applied to the motor shaft,
L_a - armature inductance,
R_a - armature resistance,
J_m - armature inertia,
B_m - friction coefficient,
K_e - back-emf constant,
K_t - electromagnetic torque constant,
d - duty cycle of the drive converter.

The duty cycle d, in Equation (2.1), as a function of the armature current, motor speed and position and the load torque T_{ex}, as a function of the motor position are defined as given below:

$$d = f(i_a, \omega_m, \theta_m)$$
$$T_{ex} = g(\theta_m) \tag{2.2}$$

The electrical equivalent circuit of Equation (2.1) is identical to that of a conventional bidirectional buck converter, which is representative of a majority of the bidirectional power converters in the aircraft power distribution system (Figure 2.1). An equivalent bidirectional buck converter representation of Equation (2.1) is shown in Figure 2.10.

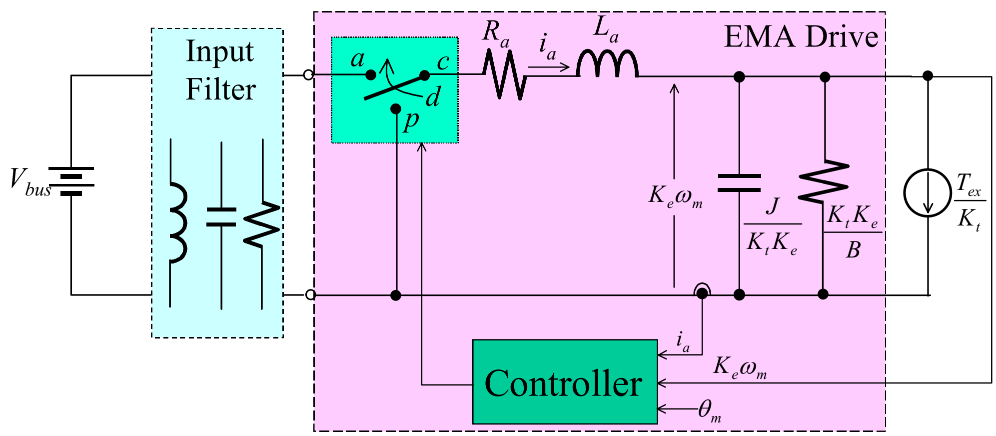

Figure 2.10. Equivalent buck converter representation of simplified EMA drive

Based on the simplifications mentioned above, the sample system is identified as a regulated DC-DC buck converter preceded by an EMI input filter. The optimization of the sample system is described in detail in the next chapter.

2.5 SUMMARY

The baseline power system architecture was introduced in this chapter. The bidirectional power converter was identified as the key electrical subsystem in the power distribution system. The EMA and EHA configurations, nature and origin of regenerative power from these actuators are described briefly. The detailed model of the EMA is reduced to a simple interconnected system consisting of a DC-DC buck converter preceded by an EMI input filter. This interconnected system leads to the identification of a sample system, which is optimized in the next chapter.

3 OPTIMIZATION OF THE SAMPLE SYSTEM

3.1 INTRODUCTION

The development of an optimization methodology for the sample power system is the subject of this chapter. Based on the simplifications presented in the previous chapter, the sample system is identified as an interconnection of a regulated DC-DC buck converter preceded by an input filter. The sample system captures the essential features of the optimization procedure. An optimization methodology is formulated for the filter. This optimization methodology is then extended to a regulated DC-DC buck converter, taking into account the increase in complexity of the converter. The procedure is then extended to the sample system to address system wide design considerations. Stability of the global system is insured, and the effects of regenerative power flow are minimized. In order to assess the validity of the results obtained from the optimizer, the optimal designs are compared to a filter built for a three-phase buck converter for a telecommunications application [54].

The sample system is introduced in section 3.2. The development of models for the input filter, buck converter and the inductor is described in section 3.3. The optimized design of the input filter as an independent subsystem is presented in section 3.4. The optimized design of the converter as an independent subsystem is then presented in section 3.5. The filter and converter are combined to form an interconnected system and optimized simultaneously in section 3.6. It is shown that optimizing the integrated system as a whole results in a lesser weight than integrating the individually optimized systems.

3.2 SAMPLE POWER SYSTEM

The sample system consists of an input filter followed by a regulated DC-DC buck converter and is shown in Figure 3.1.

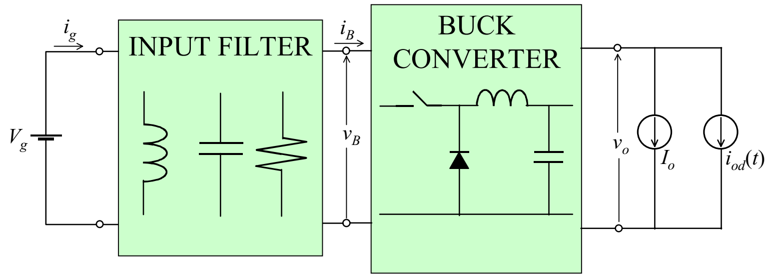

Figure 3.1. Block diagram of the sample system.

The power is supplied by the aircraft power bus, which is assumed to be a stiff DC source of $V_g = 270\text{V}$. The buck converter is representative of motor drives commonly found in aircraft power systems. The converter is loaded by a fixed DC current source I_o (to represent the average power drawn).

Switching converters, due to their high frequency switching behavior, inject an appreciable amount of high frequency noise into the system. This high frequency noise results in what is known as Electromagnetic Interference (EMI) between the converter and other interconnected systems. Input filters are added at the front end of these converters in order to prevent the switching noise from entering the source subsystem. Stringent EMI specifications exist that impose upper bounds on the input filter transfer characteristics at different frequency ranges as dictated by the specific application.

To account for the effect of regenerative power flow, the load disturbance $i_{od}(t)$ indicated in Figure 3.1 is represented by a pulse load with duration T_p as shown in Figure 3.2.

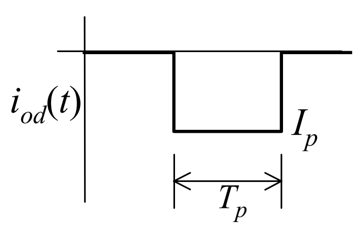

Figure 3.2. Load disturbance profile

The nominal operating conditions for the sample system are given in Table 3.1. The goal of the optimization is to design these two subsystems such that: 1) each subsystem meets its own performance specifications (to be described below), 2) the overall system is stable within prescribed stability bounds, 3) the effect of the transient disturbance source$i_{od}(t)$ at the output of the buck converter on the input voltage of the converter is limited, and 4) the overall weight of the system is minimized.

Table 3.1. Nominal Operating Conditions for Sample System

Variable	Description	Value
V_g	Filter input voltage	270 V
V_B	Filter output voltage	270 V
V_o	Converter output voltage	100 V
D	Converter duty cycle	V_o/V_g
I_o	Converter average load current	15A
I_B	Converter input current	$I_o(V_o/V_g)$
I_p	Peak value of pulse disturbance	-20 A
T_p	Duration of pulse disturbance	10 ms

The modeling of the input filter, buck converter and the inductor is described in the next section. The formulation of the optimization problems for the input filter, buck converter and the integrated sample system are then explained in the subsequent sections.

3.3 Model Development

The development of the models for the subsystems in the sample system is described in this section.

3.3.1 Input Filter

The schematic of the input filter used in the sample system is shown in Figure3.3. The DC bus is represented by an ideal DC voltage source of 270 V. The constant current source accounts for the nominal current load of the buck converter in the sample system discussed in the last section. The time varying current source accounts for the regenerative energy from the buck converter. This current source represents the dynamic coupling between various blocks of the power distribution system.

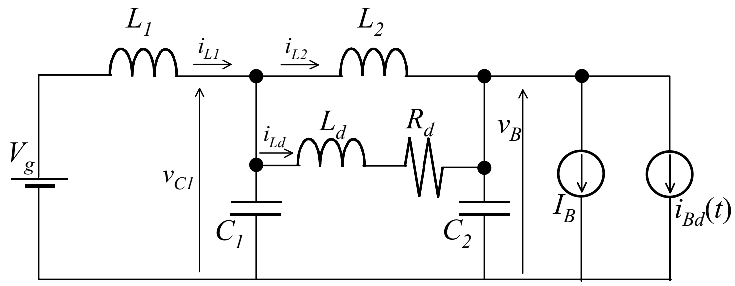

Figure 3.3. Schematic of input filter used in sample system.

Using network analysis, the state equations of the input filter can be obtained in a straightforward manner. The state equations are given by

$$\begin{aligned}
\frac{di_{L1}}{dt} &= \frac{1}{L_1}\left(V_g - v_{C1}\right) \\
\frac{di_{L2}}{dt} &= \frac{1}{L_2}\left(v_{C1} - v_B\right) \\
\frac{di_{Ld}}{dt} &= \frac{1}{L_d}\left(v_{C1} - v_B - R_d i_{Ld}\right) \\
\frac{dv_{C1}}{dt} &= \frac{1}{C_1}\left(i_{L1} - i_{L2} - i_{Ld}\right) \\
\frac{dv_B}{dt} &= \frac{1}{C_2}\left(i_{L2} + i_{Ld} - I_B - i_{Bd}\right)
\end{aligned} \tag{3.1}$$

3.3.2 Buck Converter

The schematic of the DC-DC buck converter is shown in Figure 3.4a. The switch-diode combination highlighted in Figure 3.4a is replaced by a single-pole double throw switch, known as the PWM switch, as shown in Figure 3.4b. The switch S is turned on (switch at position *a* in Figure 3.4b) and off (switch at position *b* in Figure 3.4b) at a fixed frequency to transform the input voltage v_B to a periodic square wave voltage v_L. The voltage v_L is then filtered by the *L*-*C* filter to obtain the output voltage v_o. The average value of the output voltage is varied by modulating the time interval the switch *S* is kept on.

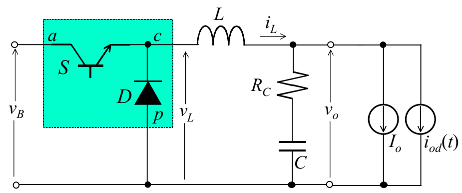

(a) Realization with transistor-diode combination

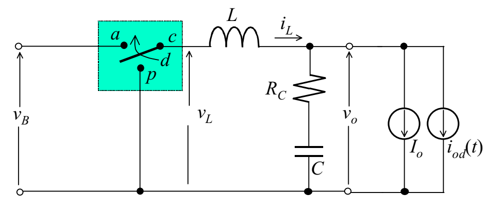

(b) Realization with PWM switch

Figure 3.4. Schematic of DC-DC Buck converter

An average model of the buck converter, which neglects the switching ripple in the currents and voltages, is used [57]. The average model of the buck converter replaces the switch-diode combination in the switch model (Figure 3.4a) by controlled current and voltage sources. A multi-loop controller consisting of an inner inductor current loop and an outer voltage loop is used for the regulation of the output voltage to a fixed reference. Since average models of the converters are in general nonlinear, small signal models linearized around an operating point are derived. These linearized models are then used for the design of the current and voltage controllers. As already mentioned, the input voltage v_B, is represented by an ideal voltage source of 270V. The average model of the buck converter along with a block diagram of the controller is shown in Figure3.5.

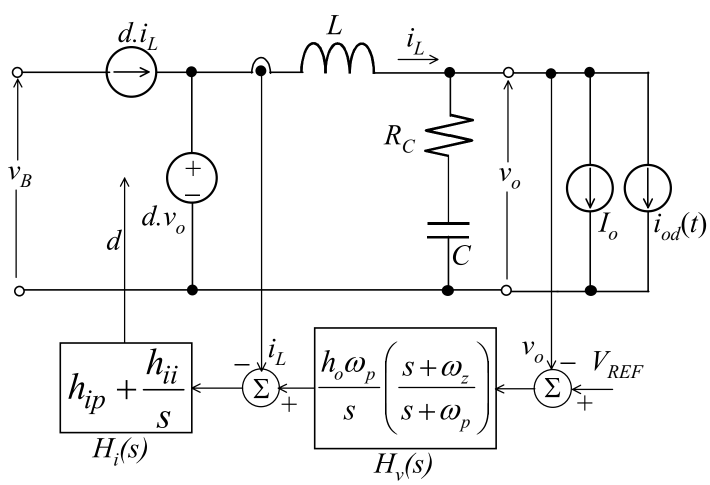

Figure 3.5. Average model of buck converter with inductor current and output voltage compensators

The state equations of the closed loop system shown in Figure 3.5 can be written as

$$\frac{di_L}{dt} = \frac{1}{L}\left(d v_B - v_C - R_C\left(i_L - I_o - i_{od}\right)\right)$$
$$\frac{dv_C}{dt} = \frac{1}{C}\left(i_L - I_o - i_{od}\right)$$
$$\frac{dv_{oc1}}{dt} = \omega_Z\left(v_{oc2} - v_{oc1}\right)$$
$$\frac{dv_{oc2}}{dt} = h_o\omega_p\left(v_o - V_{REF}\right) - \omega_p\left(v_{oc2} - v_{oc1}\right)$$
$$\frac{di_{Lc}}{dt} = h_{ii}\left(V_{REF} - v_{oc2} - i_L\right) \tag{3.2}$$

where, d is the duty cycle of the converter given by

$$d = i_{Lc} + h_{ip}\left(V_{REF} - v_{oc2} - i_L\right) \tag{3.3}$$

In Equations (3.2) and (3.3), the states v_{oc1} and v_{oc2} represent the state variables of the voltage controller and i_{Lc} represents the state variable of the current controller. The average model is nonlinear due to the product of the duty cycle d, which is a function of the state variables, and the input voltage v_B.

3.3.3 Inductor Model

The design of the inductors in the sample system includes their physical design in addition to just the determination of the inductance values. The inductors are assumed to use typical EE cores as shown in Figure 3.6.

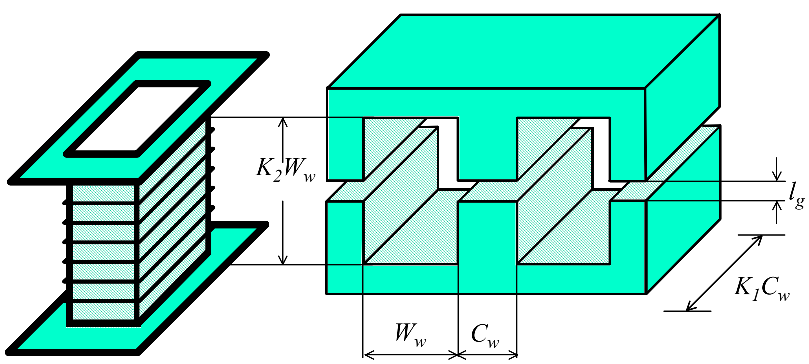

Figure 3.6. EE Core, bobbin and relevant dimensions

The quantities K_1 and K_2 shown in Figure 3.6 are assumed to be fixed and represent the aspect ratios of the center leg and the window, respectively. The other physical variables governing the design of each inductor are listed in Table 3.2. Note that these variables include parameters related to the windings and wire size.

Table 3.2. Physical variables associated with inductor design

Variable	Description
n	Number of turns
A_{cp}	Cross sectional area of
C_w	Center leg width
W_w	Window width
l_g	Airgap length

The inductance as a function of these physical variables is given by

$$L = \frac{\mu_o K_1 C_w^2 n^2}{l_g} \tag{3.4}$$

3.4 OPTIMIZATION OF THE INPUT FILTER

The optimization of the input filter is described in this section. The identification of the design variables, definition of the constraints and the objective function are explained in detail.

3.4.1 Design Variables

Design variables for the input filter shown in Figure 3.3 include the capacitance values C_1 and C_2, and resistance value R_d, and the three inductors. The complete set of input filter design variables is listed in Table 3.3.

3.4.2 Constraints

The input filter design constraints are subdivided into performance, stability and physical constraints as explained in the following subsections.

Performance Constraints

Performance constraints are further classified as frequency domain and time domain constraints.

Table 3.3. Design Variables for the Input Filter

Design Variable	Description
C_1	Filter capacitance
C_2	Filter capacitance
R_d	Filter resistance
n_d	Number of turns for L_d
A_{cpd}	Cross sectional area of winding for L_d
C_{wd}	Center leg width for L_d
W_{wd}	Window width for L_d
l_{gd}	Airgap length for L_d
n_1	Number of turns for L_1
A_{cp1}	Cross sectional area of winding for L_1
C_{w1}	Center leg width for L_1
W_{w1}	Window width for L_1
l_{g1}	Airgap length for L_1
n_2	Number of turns for L_2
A_{cp2}	Cross sectional area of winding for L_2
C_{w2}	Center leg width for L_2
W_{w2}	Window width for L_2
l_{g2}	Airgap length for L_2

Frequency domain constraints

As mentioned earlier, input filters are added at the front end of switching converters in order to prevent the high frequency noise from entering the source subsystem. Stringent EMI specifications exist that impose upper bounds on the input filter transfer characteristics at different frequency ranges as dictated by the specific application.

The EMI specifications on the input filter are typically translated into frequency domain constraints on the forward voltage transfer function of the input filter. This transfer function between the input and output voltage of the input filter in Figure3.3 is given by

$$\frac{V_B(j\omega)}{V_g(j\omega)} = A_v(j\omega) \tag{3.5}$$

The frequency response of the forward voltage transfer function for a typical input filter is shown in Figure 3.7.

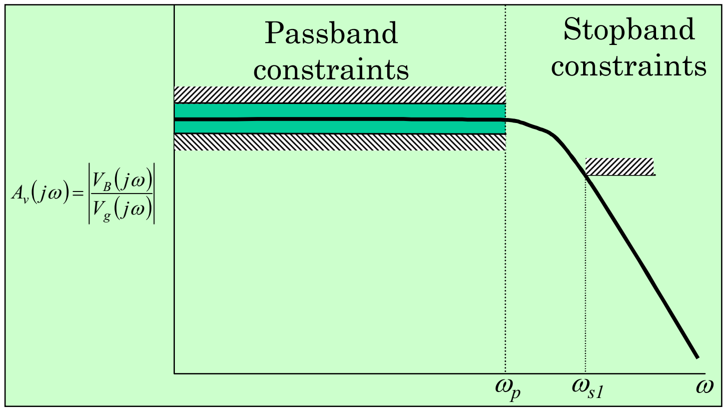

Figure 3.7. Definition of frequency domain performance specifications for the input filter

Two types of constraints exist for the frequency response function: low frequency passband constraints and high frequency stopband constraints. The transfer of power from the source to the load occurs almost entirely in the low frequency region. Hence, the input filter needs to be designed to have near unity gain in the passband. These passband constraints are defined in terms of upper and lower bounds on the input-output transfer function of the filter up to a passband frequency, ω_p, as shown in Figure 3.7. For the present problem, the passband constraint is defined as

$$-1\ dB \le |A_v(j\omega)| \le 6\ dB \ \text{ for } \ 0 \le \omega \le \omega_p = 2\pi 5 \times 10^3 \text{ rad/sec} \tag{3.6}$$

In addition, the filter must attenuate the high frequency switching noise according to given EMI specifications. Therefore, above a certain frequency, ω_{s1}, shown in Figure 3.7 the frequency response function must be below a given value.

For the present case, the frequency boundaries for the stopband and passband constraints were chosen based on the assumption that the converter to which the filter is attached has a nominal switching frequency of 100 kHz. For the present problem, the stopband constraint is

$$|A_v(j\omega)| < -60\ dB \quad \text{for } \omega > \omega_{s1} = 2\pi \cdot 50 \times 10^3 \text{ rad/sec} \tag{3.7}$$

Time Domain Constraints

The time domain constraints account for the dynamic coupling between the various components of the power distribution system. In the sample system shown in Figure 3.1, a pulse current load at the output of the buck converter develops a transient current disturbance $i_{Bd}(t)$. This transient current represents the regenerative energy from the actuator. This transient current will cause an undesirable voltage swing at the output of the filter. A time domain constraint on the output voltage is imposed to limit the disturbance. This constraint is an upper bound on the maximum transient excursion of the output voltage of the filter as indicated in Figure 3.8. For this work, the maximum transient voltage excursion limit is

$$\Delta v_B < 20\ V. \tag{3.8}$$

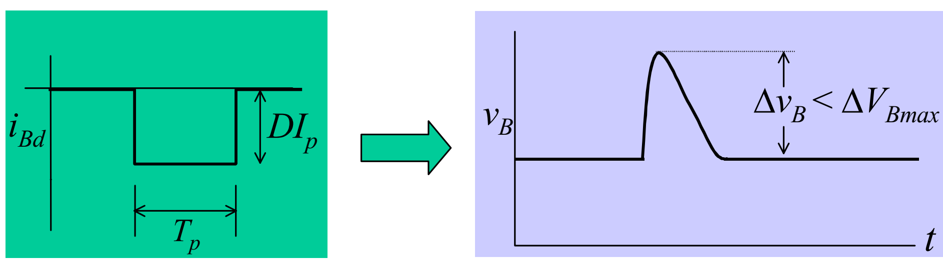

Figure 3.8. Time domain constraint for input filter

Stability Constraints

Because the input filter consists only of passive components it is generally internally stable (with all its eigenvalues in the left half of the s-plane). However, the input filter is notorious for causing instability due to its interaction with a regulated converter. It can be shown that a regulated power converter can have a negative input impedance that might cause the interconnected system to become unstable. Constraints that guarantee stability of the interconnected system are defined in the frequency domain using the Middlebrook impedance ratio criterion [37].

Figure 3.9 shows a generic subsystem interface formed by connecting two electrical subsystems. Each subsystem is represented by a standard two-port model as shown in Figure 3.9.

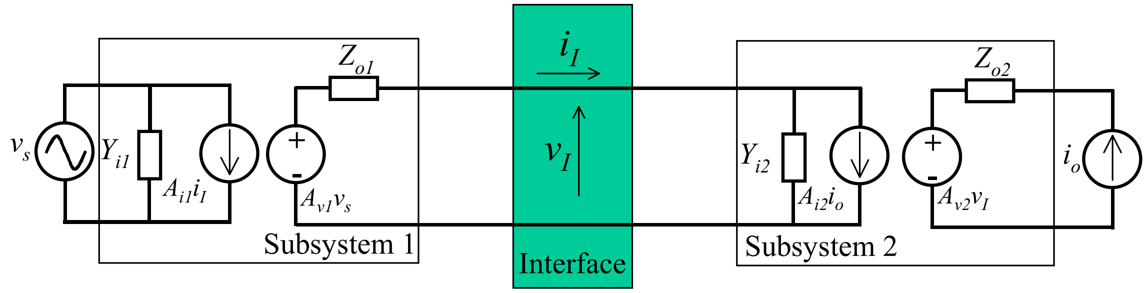

Figure 3.9. Generic Subsystem Interface

The impedance ratio criterion, explained in detail in Chapter 7, guarantees stability and minimal interaction between the interconnected subsystems by that the magnitude of the output impedance of subsystem 1 (filter) must everywhere be less than the input impedance of subsystem 2 (converter).

The input filter schematic showing only the relevant impedances is shown in Figure 3.10.

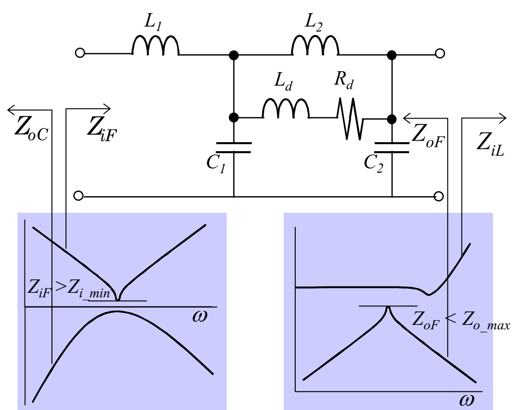

Figure 3.10. Impedances at the terminals of the input filter.

The impedance looking out of the output terminals of the filter is designated Z_{iL} and is the input impedance of the buck converter. For the filter optimization problem, this impedance is considered to be fixed and given. Applying the impedance ratio criteria, the output impedance of the filter Z_{of}, which depends on the design parameters, must be less than the impedance $Z_{iL.}$ Since Z_{iL} is given, sufficient separation between these two impedances can be enforced by requiring that the upper bound of the output impedance of the filter satisfy

$$Z_{o\_\max} = \max_{\omega}\left(\left|Z_{oF}\left(j\omega\right)\right|\right) < 15\ \text{dB} < Z_{iL} \tag{3.9}$$

A similar reasoning is applied to the interaction between the filter and the DC bus.

$$Z_{i\_\min} = \min_{\omega}\left(\left|Z_{iF}\left(j\omega\right)\right|\right) > 3\ \text{dB} \tag{3.10}$$

Physical Constraints

These constraints are defined to guarantee physically meaningful dimensions for the core and windings used in the inductor (Figure 3.6). They are defined as follows [21]:

- The widths of the center leg C_w, and of the window W_w are not allowed to be less that 1 mm to ensure sufficient mechanical strength of the core.

- In order to ensure sufficient mechanical strength for the winding, the copper wire used cannot be greater than 30AWG, which is equivalent to a cross-sectional area of $7.29 \times 10^{-8}\ \text{m}^2$.

- The number of turns in the inductor cannot be less than one and must be an integer.

- The current density in the windings of the inductor cannot be greater than maximum allowable current density for copper.

- The available window area of the EE core must be large enough to accommodate the windings of the inductor and the bobbin as shown in Figure 3.6. Through simple geometry, this constraint translates to

$$K_2 W_w^2 > \left(\frac{nA_{cp}}{F_w} + W_{bob} K_2 W_w\right) \tag{3.11}$$

where,

$$\begin{aligned} &F_w, \text{window fill factor} = 0.4 \\ &W_{bob}, \text{bobbin thickness} = 1.5\ \text{mm} \\ &K_2, \text{Window area aspect ratio} = 3 \end{aligned} \tag{3.12}$$

- The dimensions of the inductor should be such that the maximum allowable saturation flux density for a ferrite core material, B = 0.3 T, is not exceeded.

$$B_{sp} > \frac{LI_{L(pk)}}{nK_1C_w^2} \tag{3.13}$$

where,

$$\begin{aligned} &B_{sp}, \text{saturation flux density of ferrite} = 0.3T \\ &K_1, \text{center leg aspect ratio} = 1.5 \end{aligned} \tag{3.14}$$

3.4.3 Objective Function

The objective function is the weight of the input filter. The total filter weight is the sum of the weights of the inductors, capacitors, and resistors

$$J = W_L + W_C + W_R \tag{3.15}$$

The weight of an inductor is determined as the sum of the weights of iron and copper used in the core and windings, respectively

$$W_L = W_{fe} + W_{cu} \tag{3.16}$$

From Figure 3.6, the weight of the copper can be obtained as

$$W_{cu} = D_{cu}Vol_{cu} \tag{3.17}$$

where,

$$\begin{aligned} &D_{cu} = 8900\text{kg/m}^3 \\ &Vol_{cu} = MLT \cdot n \cdot A_{cp} \\ &MLT = 2F_cC_w(1+K_1), \text{mean length/turn,} \\ &F_c = 1.9, \text{winding pitch factor} \end{aligned} \tag{3.18}$$

Similarly the weight of the iron used in the EE core is given by (Figure 3.6)

$$W_{fe} = D_{fe}Vol_{fe}, \tag{3.19}$$

where,

$$D_{fe} = 7800\text{kg/m}^3 \tag{3.20}$$
$$Vol_{fe} = Z_p A_p$$
$$Z_p = 2(1+K_2)W_w + \frac{\pi}{2}C_w, \text{magnetic path length}$$
$$A_p = K_1 C_w^2, \text{Area of cross section of center leg}$$

The weight of a capacitor is approximated as a function of the energy stored in it and is given by

$$W_C = \alpha_C C V_C^2 \tag{3.21}$$

The constant α_C was obtained from manufacturer data sheets. Finally, the weight of the resistor is approximated as a function of the energy dissipated in it and is given by

$$W_R = \int_0^t R \cdot i_R^2 \cdot \text{dt} \tag{3.22}$$

3.4.4 Optimization Results

Optimization was performed using the VisualDOC optimization software [55] using the Modified Method of Feasible Directions algorithm [56]. The transient peak voltage constraint was enforced by imposing an upper bound constraint on the maximum output voltage obtained from a time domain simulation of the filter response. Constraint derivatives were computed using finite differences. Depending on the initial design used to start the optimization iterations, convergence was obtained within approximately 200 function evaluations (here a single function evaluation includes both a time domain simulation and frequency domain computations). The optimizations were achieved in approximately 40 minutes on a 500 MHz Pentium III PC.

In order to assess the validity of the results obtained from the optimizer, the optimal designs were compared to a filter built for a three-phase buck converter for a telecommunications application [54]. This hardware design, developed without the use of the optimizer, is referred to here as the nominal design. In addition to providing weight savings in comparison to the nominal design, the optimal design methodology is automated and can considerably reduce design cycle time.

The optimization algorithm used for the present work belongs to a class of optimization algorithms termed "gradient based methods". In order to begin the optimization process, these algorithms are typically provided with an initial design. Once an initial design is specified, gradients of the objective function and constraints are computed with respect to the design variables to compute a search direction in the design space. Next, the design space is searched along the computed direction so as to minimize the objective function while satisfying all the constraints. Gradients are then recomputed at the new design point, and the process continues until no further improvements are possible. If the design space contains several local minima, there is a possibility that a gradient-based optimizer may be trapped by a local minimum, and the answer will depend on the selection of the initial design point. In order to increase the probability of finding the point with the smallest objective function value (the global minimum), it is customary to execute the optimization algorithm starting from several different initial designs. In the present work, it was found that there were local minima in the design space, although in all cases studied, even the local minima were lighter than the nominal design. The results reported here correspond to the best designs found during the course of the study and are likely to be the globally optimum design.

The physical variables for the filter inductors values for the nominal and optimal designs are given in Table 3.4. The nominal and optimum component values and the objective function are provided in Table 3.5. Response quantities of interest for the nominal and optimal designs are given in Table 3.6. Response quantities that are at their upper or lower bounds are listed in bold face type. All the physical constraints on the inductor designs were active for the optimal design. The other active constraints for the optimized design were the lower bound constraint on the input impedance Z_{iF} and the stopband constraint on the input-output transfer function. Note that the peak voltage constraint was violated for the nominal design.

Table 3.4. Physical variables of the filter inductors

Variable	Nominal value	Optimal value
n_1	29.53	19.94
A_{cp1}	0.630 x 10^{-5} m^2	0.530 x 10^{-5} m^2
C_{w1}	0.751 x 10^{-2} m	0.484 x 10^{-2} m
W_{w1}	0.682 x 10^{-2} m	1.017 x 10^{-2} m
l_{g1}	1.16x 10^{-3} m	0.664 x 10^{-3} m
n_2	45.98	42.77
A_{cp2}	0.448 x 10^{-5} m^2	0.382 x 10^{-5} m^2
C_{w2}	0.985 x 10^{-2} m	0.939 x 10^{-2} m
W_{w2}	1.33 x 10^{-2} m	1.244 x 10^{-2} m
l_{g2}	1.29 x 10^{-3} m	1.03 x 10^{-3} m
n_d	16.06	7.79
A_{cpd}	0.349 x 10^{-5} m^2	0.359 x 10^{-5} m^2
C_{wd}	0.396 x 10^{-2} m	0.585 x 10^{-2} m
W_{wd}	0.978 x 10^{-2} m	0.564 x 10^{-2} m
l_{gd}	0.355 x 10^{-3} m	0.176 x 10^{-3} m

Table 3.5. Nominal and Optimal Filter Designs

Variable	Nominal value	Optimal value
L_1	80 μH	26.49 μH
L_2	300 μH	296.77 μH
L_d	21.5 μH	22.29 μH
C_1	5 μF	7.19 μF
C_2	18.8 μF	27.70 μF
R_d	3 Ω	2.23 Ω
Weight	0.5279 kg	0.3692 kg

Table 3.6. Response quantities for nominal and optimal designs of input filter

Response variable	Nominal	Optimal
Minimum input	3.81* dB	**2.99 dB**
Maximum output	15.39 dB	9.11 dB
Passband maximum	5.63 dB	3.18 dB
Passband minimum	6.55 x 10^{-6} dB	7.94390 x 10^{-6}
Stopband maximum	-63.13dB	**-60.00 dB**
Peak output voltage	21.97* V	13.75 dB

*violated constraint

In order to compare the optimization results with the hardware (nominal) design, several additional optimization runs were performed corresponding to different values of the lower bound constraint Z_{i_min} on the input impedance. The resulting family of optimal designs is compared to the nominal design in Figure 3.11. For the same value (3.8 dB) of Z_{i_min}, the optimal design is 25% lighter than the nominal design. For the same weight, on the other hand, the minimum input impedance for the optimized design is approximately 47% higher than for the nominal design.

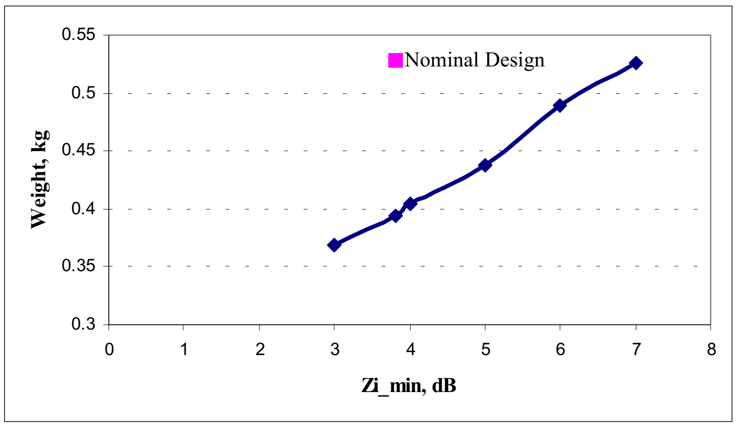

Figure 3.11. Weight of optimal designs as a function of the lower bound on the input impedance

3.5 OPTIMIZATION OF BUCK CONVERTER

The formulation of the optimization problem for the design of the buck converter, the second subsystem in the sample system discussed in Section 3.2 is considered. The approach to this subsystem is very similar to the approach taken for the filter, particularly the interaction constraints. Some additional constraints are required for the converter, however, because of its internal complexity.

3.5.1 Design Variables

Design variables for the buck converter include the physical parameters governing the design of the inductor L, the capacitance C, the switching frequency of the converter f_s, and a set of parameters governing the feedback controller (h_o, ω_z, ω_p, h_{ip}, and h_{ii}). As with the filter, it is assumed that an EE core is used for the inductor (Figure 3.6). Table 3.7 contains a list of all design variables used for the buck converter.

Table 3.7. Design Variables for buck converter

Design Variable	**Description**
n	Number of turns for L
A_{cp}	CSA of winding for L
C_w	Center leg width for L
W_w	Window width for L
l_g	Airgap length for L
C	Capacitance
f_s	Switching frequency of buck converter
h_o	Voltage controller gain
ω_z	Voltage controller zero
ω_p	Voltage controller pole
h_{ip}	Current controller proportional gain
h_{ii}	Current controller integral gain

3.5.2 Constraints

The performance, stability and physical constraints on the design of the buck converter are described in the following paragraphs.

Performance Constraints

Frequency Domain Constraints

Two frequency domain constraints are imposed on the buck converter. The average model of the closed loop converter is linearized around the nominal operating point to yield a small signal linear model. This linear model is then used for the determination for the transfer functions on which the frequency domain constraints are imposed. These constraints can be explained with the help of the simplified block diagram of the closed loop buck converter shown in Figure 3.12.

Frequency domain constraints for the buck converter are imposed as upper bounds on the maximum magnitude of the transfer function between the input and output voltage and the voltage loop gain crossover frequency.

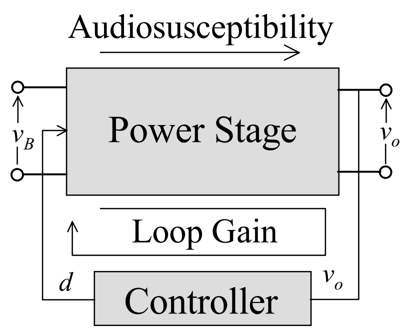

Figure 3.12. Simplified block diagram of closed loop buck converter

The transfer function between the input voltage v_B and the output voltage v_o is called the audiosusceptibility of the converter. A typical transfer function is shown in Figure 3.13a. An upper bound is imposed on this transfer function in order to guarantee sufficient rejection of any audio frequency disturbance introduced at the input voltage. This constraint can be stated as

$$A_v = \max_{\omega} \left| \frac{V_o(j\omega)}{V_B(j\omega)} \right| < -30\,\text{dB} \tag{3.23}$$

The second constraint is imposed on the loop gain. The loop gain is the open loop transfer function between the output voltage error V_{ref} - v_o, and the output voltage v_o (Figure 3.50). The characteristics of the loop gain transfer function determine the bandwidth and the stability margins of the closed loop system. A typical curve is shown in Figure 3.13b.

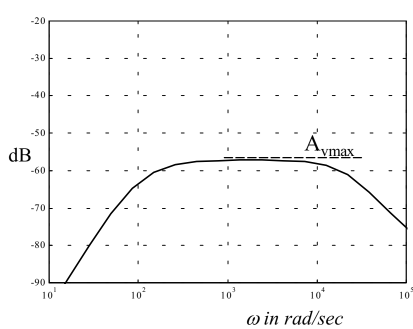

(a) Audiosusceptibility

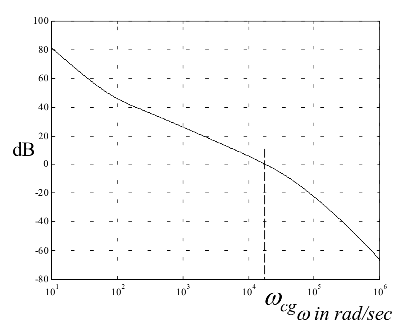

(b) Voltage Loop Gain

Figure 3.13. Frequency Domain Constraints for the buck converter

An upper bound constraint is also imposed on the crossover frequency of the voltage loop gain, ω_{cg} in order to limit the bandwidth of the converter. (This relationship can be found in classical control theory.) The bound on the bandwidth of the converter will guarantee that the switching frequency ripple in the inductor current and the output voltage are sufficiently attenuated before they propagate through the controller. The frequency ω_{cg} is chosen to be sufficiently less than half the switching frequency. For the present problem this upper bound is given by

$$\omega_{\mathrm{cg}} < \frac{2\pi f_s}{5} \tag{3.24}$$

Additional constraints will be imposed on the voltage loop gain for stability reasons as discussed below.

Time Domain Constraints

Time domain constraints are introduced to account for transients in the voltages in the converter due to transient disturbances at the output terminals of the converter. These constraints are identical to those developed for the filter in Section 3.3. A pulse load disturbance represents the transient disturbance at the output of the buck converter. For the optimized design of the buck converter, a fixed resistance is included in series with an ideal voltage source as shown in Figure 3.14.

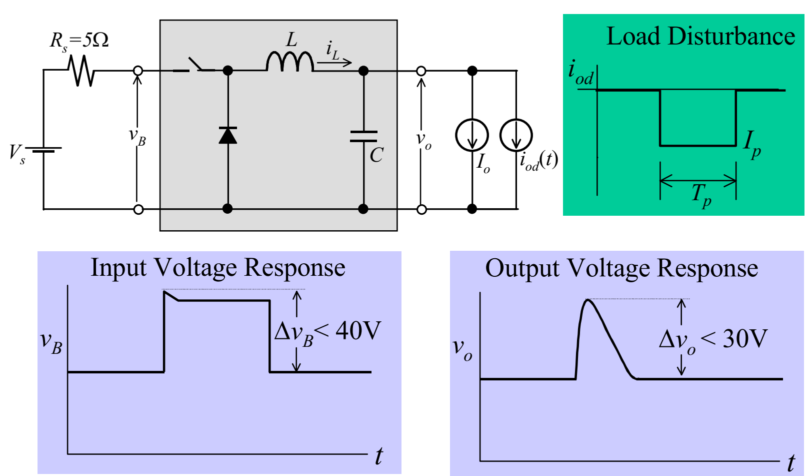

Figure 3.14. Time domain constraints for the converter

This fixed resistance was included to represent the effect of the input filter when imposing the impedance ratio criteria for stability. The resistance value was chosen to be equal to 5Ω, which was the maximum output impedance (15 dB) of the nominal input filter design (Table 3.6) and the voltage variations at the input and output of the converter were constrained as

$$v_B < 40V, \Delta v_o < 30V \tag{3.25}$$

Stability Constraints

Like the filter, the buck converter must satisfy external stability constraints, so that the entire sample system in Figure 3.1 is stable. In addition, because of the presence of the internal control loop, the converter must be internally stable.

Internal Stability Constraints

The design of the feedback controller for the buck converter (Figure 3.5) must guarantee stability and robustness of the closed loop system in the presence of disturbances in the load current and source voltage. These stability constraints are defined as bounds on the gain margin, g_m, and phase margin, ϕ_m of the closed loop. From classical control theory [58], positive values of phase margin and gain margin are necessary conditions for stability. In order to guarantee sufficient robustness of the closed loop, lower bounds are imposed on these values. These values are widely used in the design of switching converters. These constraints translate into constraints on the voltage loop gain in Figure 3.13b.

$$\begin{aligned} \phi_{\mathrm{m}} &> 60^o \\ g_{\mathrm{m}} &> 3\,\mathrm{dB} \end{aligned} \tag{3.26}$$

External Stability Constraints

External stability constraints are used to guarantee stability of the interconnected system after adding the input filter. As for the input filter, they are defined using the impedance ratio criterion with the input and output impedances appropriately defined. An upper bound is imposed on the maximum magnitude of the output impedance, Z_{o_max}, and a lower bound on the minimum magnitude of the input impedance, Z_{i_min}, of the closed loop converter. Using the notation of Section 3.3, these bounds are given as

$$\begin{aligned} Z_{i\_\min} &= \min_{\omega}\left(\left|Z_{iB}(j\omega)\right|\right) > 30\text{ dB} \\ Z_{o\_\max} &= \max_{\omega}\left(\left|Z_{oB}(j\omega)\right|\right) < 20\text{ dB} \end{aligned} \tag{3.27}$$

Since the output impedance of the filter is set to 15dB in Equation (3.9), the first of these two constraints ensures that there is at least a 15 dB separation between the output impedance of the filter and the input impedance of the converter. (See Figure 3.10.) The upper bound of the output impedance is set to ensure sufficient separation from the minimum input impedance of the load to the buck converter. Since the load is represented by an ideal current source (which has an infinite input impedance), the upper bound of the output impedance was arbitrarily chosen.

Physical Constraints

In addition to the physical constraints, which guarantee physically meaningful dimensions for the core and winding of the inductors similar to the input filter, constraints are also imposed to limit the switching ripple in the inductor currents and the capacitor voltages. Although the average model for the buck converter is used for the analysis, expressions for switching ripple in terms of average quantities are readily available.

Inductor Current Ripple

It is generally required that the peak-to-peak inductor current ripple be less than 10% of the nominal inductor current. From Figure 3.50, the inductor current ripple can be obtained as [57]

$$\Delta I_L = \frac{(1-D)}{f_s}\frac{V_o}{L} \tag{3.28}$$

If $P_o = V_o\, I_{L(nom)}$, is the nominal power rating of the converter, a lower bound on the inductance based on the switching ripple is then determined as follows

$$\varDelta I_L < 0.1 I_{L(nom)} \Rightarrow L > 10\left(\frac{V_o^2}{P_o}\right).\left(\frac{1-D}{f_s}\right) \tag{3.29}$$

Output Voltage Ripple

The ripple in the output voltage is generally limited to be less than 1% of the average value. It is assumed that the capacitor absorbs the ripple component of the inductor current. The peak-to-peak output voltage ripple constraint is derived as follows [57]

$$\varDelta V_o = \frac{1}{8C}\frac{\varDelta I_L}{f_s} + \varDelta I_L R_C \tag{3.30}$$

Substituting for the inductor current ripple from Equation (3.29), the output voltage ripple constraint is

$$\begin{aligned} &\varDelta V_o = \frac{1}{8LC}\frac{(1-D)}{f_s}V_o + \frac{(1-D)}{Lf_s}V_o R_C = \frac{1}{LC}\frac{(1-D)}{f_s^2}V_o\left(\frac{1}{8}+\tau f_s\right) < 0.01V_0 \\ &\varDelta V_o < 0.01V_o \Rightarrow LC > 100.\left(\frac{1-D}{f_s^2}\right)\left(\frac{1}{8}+\tau f_s\right), \end{aligned} \tag{3.31}$$

where $\tau = R_C C$ is the ESR time constant of the capacitor. If the voltage ripple is limited to be less than 1% of the average value, then the following constraint is obtained.

$$LC > 100.\left(\frac{1-D}{f_s^2}\right)\left(\frac{1}{8}+\tau f_s\right) \tag{3.32}$$

3.5.3 Objective Function

The objective function is the weight of the converter, which is calculated according to Equation (3.63) as the sum of the weights of the inductors and the capacitors. The controller is not assumed to contribute significantly to the weight of the converter and hence is neglected in the determination of the weight.

3.5.4 Optimization Results

As was the case for the input filter problem, the VisualDOC optimization software [55] using the Modified Method of Feasible Directions algorithm [56] were used to obtain an optimized design. The transient peak voltage constraint was enforced by imposing an upper bound constraint on the maximum output voltage obtained from a time domain simulation of the filter response. Constraint derivatives were computed using finite differences. Converged optimal designs were obtained in approximately 300 function evaluations (a single function evaluation includes both a time domain simulation and frequency domain computations). The optimizations were achieved in approximately 20 minutes on a 500 MHz Pentium III PC. The optimal design for the buck converter was generally insensitive to the initial design.

In order to assess the validity of the results obtained from the optimizer, the optimal designs where compared to a three-phase buck converter for a telecommunications application [54]. This hardware design, developed without the use of the optimizer, is referred to as the nominal design.

The physical variables for the filter are given in Table 3.8.

Table 3.8. Physical variables for the inductor in the buck converter

Variable	Nominal value	Optimal value
n	55	55.55
A_{cp}	1.1×10^{-5} m^2	1.05×10^{-5} m^2
C_w	1.65×10^{-2} m	1.626×10^{-2} m
W_w	2.5×10^{-2} m	2.28×10^{-2} m
l_g	3.9×10^{-3} m	3.66×10^{-3} m

The nominal and optimal designs of the buck converter along with the corresponding objective functions are presented in Table 3.9. Response variables of interest for the optimized buck converter are given in Table 3.10. Response variables at their upper or lower bounds are listed in bold face type. The active constraints for the optimized converter design were the physical constraints on the design of the inductor and the constraint on the input voltage variation to the transient load disturbance. Note that the nominal design violates the constraint on the inductor current ripple. The optimized converter design is not significantly lighter than the nominal design, but it was obtained in a shorter period of time and with a minimal amount of effort compared to the standard manual design procedures.

Table 3.9. Component values and objective function for the buck converter

Variable	Nominal value	Optimal value
L	**400 μH**	**419.75 μH**
C	82 μH	46. 88 μF
h_o	1	0.881
ω_z	100 rad/sec	420.14 rad/sec
ω_p	40000 rad/sec	54983 rad/sec
h_{ip}	1	0.998
h_{ii}	100	100
f_s	100kHz	100 kHz
Weight	**1.5637 kg**	**1.5072 kg**

Table 3.10. Response quantities for nominal and optimal designs

Response variable	**Nominal**	**Optimal**
Inductor current ripple	1.574 A*	**1.5A**
Capacitor voltage ripple	0.6V	**1V**
Phase margin	72.5°	69.54°
Gain margin	58.67 dB	37.13 dB
Minimum input impedance	33.72 dB	33.69 dB
Maximum output impedance	0.02 dB	1.25 dB
Audiosusceptibility	-57.24 dB	-55.99 dB
Peak output voltage	19.85 V	22.61 V
Peak input voltage	37.38 V	38.85 V

* Violated constraint

3.6 OPTIMIZATION OF SAMPLE SYSTEM

The optimization procedure for the design of the sample system (combined filter/converter) is presented in this section. The individual optimization formulations of the input filter and the converter are combined with a few modifications in the definition of the constraints. The design variables are those of the input filter and the converter as shown in Tables 3.3 and 3.7. The constraints on the optimization of the interconnected system are obtained from those of the designs of each of the individual systems with some modifications to account for interactions between the input filter and the converter. The constraints that need to be modified are those that are defined at the interface between the input filter and the converter.

1. Due to the interconnection of the filter and the converter, it may not be appropriate to impose fixed limits on the output impedance of the filter and the input impedance of the converter, as was the case when they were designed independently. Since a sufficient condition for stability is to ensure a minimum separation between the two impedances, the constraints on the minimum input impedance of the converter, Z_{iB}, and the maximum output impedance of the filter, Z_{oF}, are replaced by a single constraint that imposes a lower bound on the difference between the two as shown in Figure 3.15a.

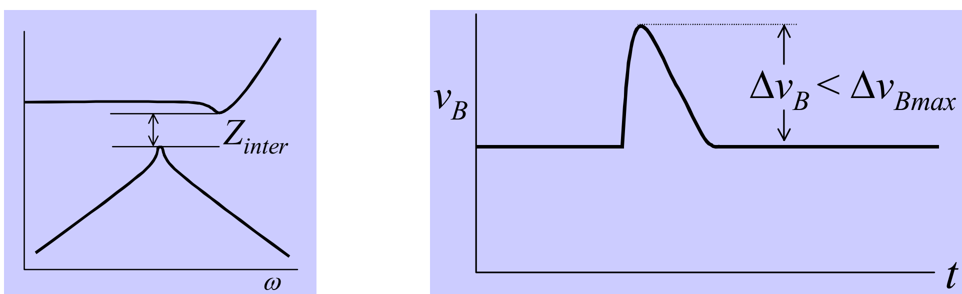

(a) Impedance Separation (b) Interface voltage variation

Figure 3.15. Interaction constraints on the sample system design

The interaction constraints used for the current example are

$$\min_{\omega}\left(\left|Z_{iB}(j\omega)\right|\right) - \max_{\omega}\left(\left|Z_{oF}(j\omega)\right|\right) > 15\ \text{dB} \tag{3.33}$$

The 15-dB separation used in the first constraint is consistent with the constraints used for the individually optimized designs (Equations (3.9) and (3.27)) presented earlier. All other constraints are directly carried over from the optimization formulations of the input filter and the buck converter.

2. The constraint on the transient excursions on the output voltage of the input filter and the input voltage of the converter are replaced by a single constraint on the maximum excursion of the interface voltage v_B, as shown in Figure 3.15b.

$$v_B < 20V \tag{3.34}$$

3. The objective function is the total weight of the input filter and converter.

Optimization Results

Converged optimal designs were obtained in approximately 1400 function evaluations, where a single function evaluation again includes both a time domain simulation and frequency domain computations. The optimizations were achieved in approximately 90 minutes on a 500 MHz Pentium III PC. The physical variables associated with the inductors in the sample system are given in Table 3.11. The component values and objective functions are given in Table 3.12. The important responses are listed in Table 3.13.

The active constraints for the filter in this optimization run were all the physical constraints on the design of the inductors, the lower bound constraint on the input impedance, the upper bound stopband constraint, and the upper bound constraint on the passband. The active constraints on the converter were the physical constraints on the inductor design and the upper bound on the voltage variation at the output due to a load disturbance. The filter design obtained from the combined problem is 5% lighter than that obtained from the individual optimization, while the converter design obtained for the combined optimization problem is almost identical to that obtained independently. Differences in the combined designs and the independently obtained designs arise because the interconnection of two subsystems creates a feedback loop where a change in the source subsystem causes a change in the load subsystem and vice versa. When the optimization was performed on the integrated sample system as a whole, the optimizer was able to take advantage of the interaction between the filter and converter and reduce the overall system weight. The nature of the interaction between the filter and the converter are explained in the following.

Table 3.11. Physical variables of inductors in sample system

Variables		Nominal	Individual Optimization	Integrated Optimization
FILTER	n_1	29.53	19.94	20.01
	A_{cp1}	0.630 x 10^{-5}	0.530 x 10^{-5} m^2	0.521 x10^{-5} m^2
	C_{w1}	0.751 x 10^{-2} m	0.484 x 10^{-2} m	0.480 x 10^{-2} m
	W_{w1}	0.682 x 10^{-2} m	1.017 x 10^{-2} m	1.014 x 10^{-2} m
	l_{g1}	1.16 x 10^{-3} m	0.664 x 10^{-3} m	0.657 x 10^{-3} m
	n_2	45.98	42.77	42.81
	A_{cp2}	0.448 x 10^{-5}	0.382 x 10^{-5} m^2	0.370 x 10^{-5} m^2
	C_{w2}	0.985 x 10^{-2} m	0.939 x 10^{-2} m	0.914 x 10^{-2} m
	W_{w2}	1.33 x 10^{-2} m	1.244 x 10^{-2} m	1.230 x 10^{-2} m
	l_{g2}	1.29 x 10^{-3} m	1.03 x 10^{-3} m	1.017 x 10^{-3} m
	n_d	16.06	7.79	7.78
	A_{cpd}	0.349 x 10^{-5}	0.359 x 10^{-5} m^2	0.356 x 10^{-5} m^2
	C_{wd}	0.396 x 10^{-2} m	0.585 x 10^{-2} m	0.576 x 10^{-2} m
	W_{wd}	0.978 x 10^{-2} m	0.564 x 10^{-2} m	0.561 x 10^{-2} m
	l_{gd}	0.355 x 10^{-3} m	0.176 x 10^{-3} m	0.172 x 10^{-3} m
BUCK	n	55	55.55	55.55
	A_{cp}	1.1 x 10^{-5} m^2	1.05 x 10^{-5} m^2	1.05 x 10^{-5} m^2
	C_w	1.65 x 10^{-2} m	1.626 x 10^{-2} m	1.63 x 10^{-2} m
	W_w	2.5 x 10^{-2} m	2.28 x 10^{-2} m	2.28 x 10^{-2} m
	l_g	3.9 x 10^{-3} m	3.66 x 10^{-3} m	3.67 x 10^{-3} m

When the input filter is optimized individually, the load disturbance was represented by a pulse current load similar to that at the output of the converter except that it was scaled by its duty cycle. When the converter and the filter are optimized together, the load disturbance at the output of the filter (and hence, at the input of the converter) is filtered by the presence of the converter. Hence, the transient peak currents flowing into the inductors of the filter are less than those that were present when the filter was optimized individually.

This is illustrated in Figure 3.16 and where the transient responses of the filter inductor current i_{L1}, with and without the buck converter are shown. Since the peak currents flowing into the filter inductors are lower when the converter is taken into account, smaller inductors can be used. This results in a lower weight filter.

Table 3.12. Component values and Objective Function for the sample system

Variables		Nominal	Individual Optimization	Integrated Optimization
F	L_1	80 μH	26.49 μH	26.531 μH
I	L_2	300 μH	296.77 μH	283.84 μH
L	L_d	21.5 μH	22.29 μH	22.045 μH
T	C_1	5 μF	7.19 μF	7.21 μF
E	C_2	18.8 μF	27.70 μF	27.86 μF
R	R_d	3 Ω	2.23 Ω	2.27 Ω
WEIGHT		**0.5279 kg**	**0.3692 kg**	**0.3495 kg**
C	L	400 μH	419.75 μH	419.75 μH
O	C	82 μF	46. 88 μF	46.904 μF
N	h_o	1	0.881	0.880
V	ω_z	100 rad/sec	420.14 rad/sec	420.12 rad/sec
E	ω_p	40000	54983 rad/sec	54998.2 rad/sec
R	h_{ip}	1	0.998	0.998
T	h_{ii}	100	100	100
E	f_s	100 kHz	100 kHz	100 kHz
R				
WEIGHT		**1.5637 kg**	**1.5072 kg**	**1.5072 kg**

Table 3.13. Response quantities of Integrated Optimization

Response Quantity		Value
INPUT FILTER	Minimum input impedance	**3.00 dB**
	Maximum output	9.3382 dB*
	Passband maximum	3.36 dB
	Passband minimum	4.87 x 10^{-6} dB
	Stopband maximum	-60 dB
BUCK CONVERTER	Phase margin	69.57°
	Gain Margin	37.18 dB
	Minimum input impedance	33.72 dB*
	Maximum output	1.25 dB
	Audiosusceptibility	-55.98 dB
	Peak output voltage	22.59 V
INTERFACE QUANTITIES	Impedance Difference	24.378 dB
	Peak interface voltage	11.81 V

* These responses were not constrained while performing the integrated optimization. They are shown here for the sake of completeness.

It can be seen from Figure 3.17 that the output voltage variation of the buck converter in the optimized sample system is higher than that of the individually optimized converter.

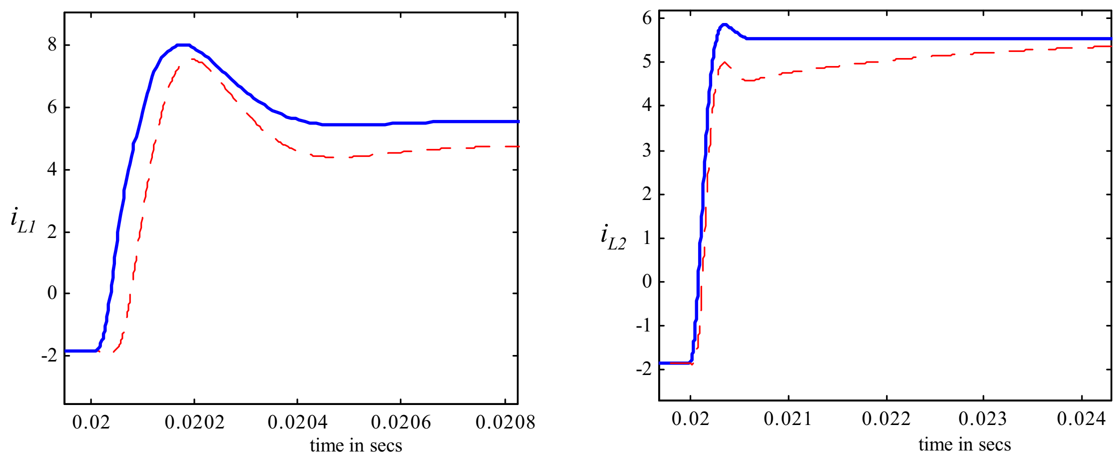

(a) Filter Inductor current i_{L1} (b) Filter Inductor Current i_{L2}

Figure 3.16. Filter inductor currents with (--) and without (-) buck converter

Simulation results of the sample system with the converter design obtained from the individual and integrated optimizations are shown in Figure 3.17.

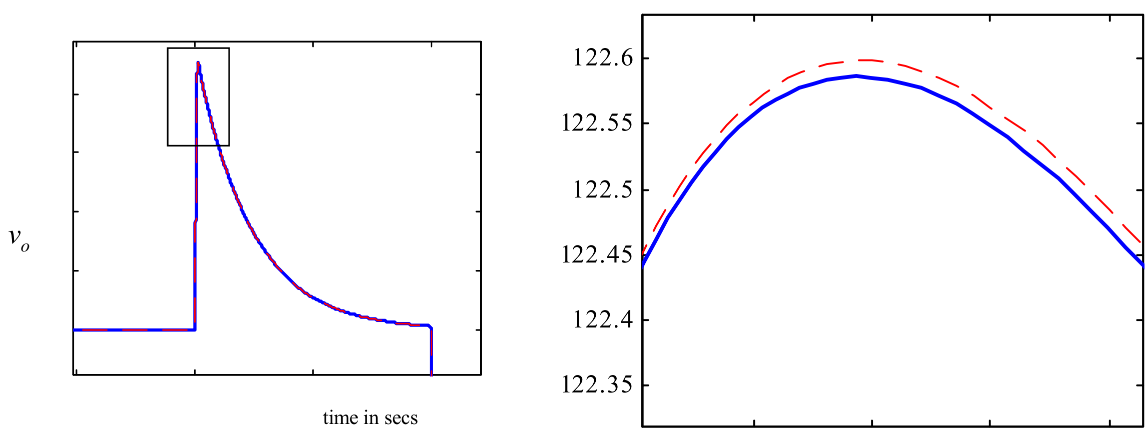

(a) Converter output voltage in sample system (b) Expanded view of boxed area in (a)

Figure 3.17. Converter output voltage in sample system with individually optimized converter design (-) and converter design obtained from optimized sample system (--)

A similar observation can be made from Figures 3.16a and 3.16b, where the filter inductor currents are shown. The optimizer increases the capacitance slightly (Table

3.12) at the output of the buck converter to allow a larger voltage variation. This results in a larger portion of the transient current to flow into the output capacitance of the buck converter than propagate to the filter. This enables the filter weight to be significantly decreased. The optimizer was, therefore, able to take advantage of the system interactions and the more accurate representations of the load disturbances and voltage variations to arrive at an improved (lower weight) design for the combined filter/converter sample system.

3.7 SUMMARY

The problem of formulating a mathematical optimization problem for the design of subsystems in an aircraft power distribution system was considered in this chapter.. The approach is to develop a mathematical optimization problem for the various components of the power distribution system in such a way that these component problems can be easily integrated into a larger optimization problem. This concept is demonstrated on a simple interconnected system consisting of an input filter and a regulated DC-DC buck converter. First, an optimization problem is developed for the filter and the converter separately, and it is shown that reasonable results are obtained. Next an optimization problem is developed for the interconnected system using the optimization formulations of the two subsystems. It was shown that optimizing the sample system as a whole resulted in a lesser weight because the optimizer was able to account for the interactions between the interconnected subsystems.

PART II

PIEZOELECTRIC ACTUATORS

4 MODELING

4.1 INTRODUCTION

The study of smart actuators in this research effort is limited to piezoelectric actuators used for active vibration control of aircraft surfaces. The study is motivated by the application of piezoelectric actuators for alleviating the "tail buffeting" problem in a twin tail aircraft [24]. The buffet loads acting on the tail surface cause excessive wear and tear that significantly reduce the lifetime of the aircraft and increase repair and maintenance costs. Piezoelectric actuators mounted at the root of the tail and on the surface are controlled to actively suppress the effect of the buffet loads on the tail surface. These actuators are electrically capacitive elements so that the load presented to the DC bus is almost purely reactive. Strain is induced in the actuation material by cycling charge in and out of the actuator. The drive electronics must be carefully designed, as these reactive loads require a significant amount of electrical energy to be cycled between the actuator and electronics. Furthermore, these materials also support reverse power flow by changing mechanical energy into electrical energy.

A detailed electromechanical model of a piezoelectric actuator is developed in this chapter. A simple mass-spring-damper system is used as the coupled mechanical structure. The linear model of the actuator is developed from the linear piezoelectric, constitutive equations. Modifications to the linear model to account for the anhysteretic nonlinearity between the polarization and the electric field are then included to develop the nonlinear model.

4.2 MODELING OF THE ACTUATOR AND STRUCTURE

The electromechanical model of the piezoelectric actuator coupled to a simple mechanical structure is developed in this section. The linear, constitutive equations of the actuator are used to develop the model. This model can be directly coupled to the dynamic model of the amplifier. Modifications to the linear model to account for the anhysteretic nonlinearity between the polarization and the electric field in the actuator are described.

The mechanical model of the actuator-structure is represented by a simple mass-spring-damper system acted on by a disturbance force f_{ext} as shown in Figure 4.1.

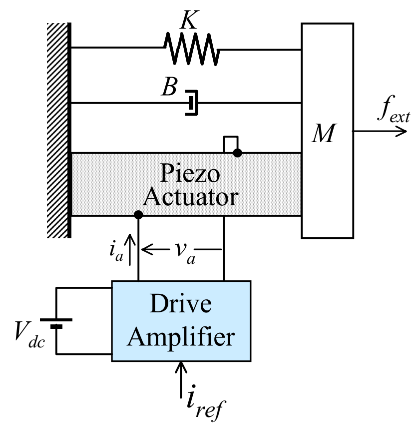

Figure 4.1. Schematic of amplifier driving the actuator-structure

A drive amplifier operating off a fixed dc voltage V_{dc} provides the power to the piezoelectric actuator. The coordinate system and the forces acting on the mass M are identified in Figure 4.2 where f_a is the force exerted by the actuator on the mass.

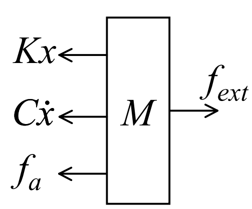

Figure 4.2. Freebody diagram of the mass

The equation of motion can then be written as

$$M\ddot{x} + B\dot{x} + Kx = f_{ext} - f_a \tag{4.1}$$

A block diagram representation of Equation (4.1) is shown in Figure 4.3.

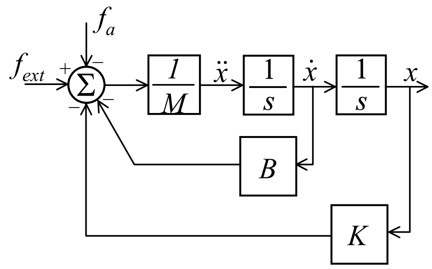

Figure 4.3. Block diagram representation of structure

The electromechanical model of the actuator is determined in the following. We assume that the actuator has a multilayered stack configuration as shown in Figure 4.4. Each layer is rectangular with width *w*, length *l* and thickness *d*. The actuator is formed by stacking *n* of these layers together. Contiguous layers are polarized in opposite directions and the voltage is applied to the layers as shown in Figure 4.4.

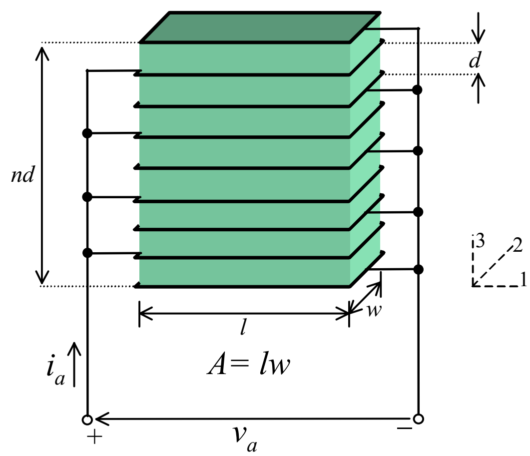

Figure 4.4. Actuator Configuration

The one-dimensional, linear, coupled, electromechanical, constitutive relations between the strain S_3, stress T_3, electric field E_3, and electric displacement D_3, are

$$D_3 = \varepsilon_{33} E_3 + d_{33} T_3 \qquad (4.2)$$
$$S_3 = d_{33} E_3 + \frac{1}{Y_{33}} T_3$$

where, ε_{33} is the dielectric permittivity, Y_{33} is elastic modulus and d_{33} is the transverse piezoelectric charge constant. The first index in the subscripts indicates the direction of the electrical component and the second index indicates the mechanical direction. The first equation in Equation (4.2) states that the electric displacement or polarization is the superposition of the direct piezoelectric effect and the applied field times the permittivity. The second equation states that the strain is the superposition of Hooke's law and the indirect effect where a mechanical deformation is caused due to the application of an electric field.

Using the geometry of the actuator, we can use Equation (4.2) to express the relationship between charge and voltage. Noting that charge is displacement per unit area, and electric field is voltage per unit length, the charge q_l entering each layer can be obtained as

$$\frac{1}{lw} q_l = \varepsilon_{33} \frac{v_a}{d} + d_{33} T_3 \tag{4.3}$$

Rewriting this equation we obtain

$$\begin{aligned} q_l &= \varepsilon_{33} \frac{lw}{d} v_a + d_{33} lw \\ &= C_l v_a + d_{33} lw T_3 \end{aligned} \tag{4.4}$$

where, C_l represents the capacitance of each layer and v_a is the voltage across the terminals of the actuator. The total charge entering all the n layers of the actuator is then given by

$$q = nq_l = nC_l v_a + d_{33} nlw T_3 \tag{4.5}$$

Solving Equation (4.3) for the voltage v_a we obtain

$$v_a = \frac{1}{nC_l} q - \frac{d_{33}}{\varepsilon_{33}} dT_3 = \frac{1}{C} q - \frac{d_{33}}{\varepsilon_{33}} dT_3 \tag{4.6}$$

where,

$$C = nC_l = \varepsilon_{33} \left(\frac{nlw}{d} \right)$$

From Equation (4.6) the voltage across a piezoelectric actuator is the resultant of two components: 1) the direct capacitive effect, and 2) a contribution from the mechanical stress. Next we replace electric field by the voltage in the second equation in Equation (4.2) and substitute in voltage from Equation (4.6). We obtain

$$S_3 = d_{33}E_3 + \frac{1}{Y_{33}}T_{33} = d_{33}\frac{v_a}{d} + \frac{1}{Y_{33}}T = \frac{d_{33}}{d}\left(\frac{1}{C}q - \frac{d_{33}}{\varepsilon_{33}}dT_3\right) + \frac{1}{Y_{33}}T_3 \tag{4.7}$$
$$= \frac{1}{nlw}\frac{d_{33}}{\varepsilon_{33}}q + \left(1 - \frac{Y_{33}d_{33}^2}{\varepsilon_{33}}\right)\frac{1}{Y_{33}}T_3$$
$$= \frac{1}{nlw}\frac{d_{33}}{\varepsilon_{33}}q + \left(1 - k^2\right)\frac{1}{Y_{33}}T_3$$

The electromechanical coupling coefficient k^2 is

$$k^2 = \frac{Y_{33}d_{33}^2}{\varepsilon_{33}} \tag{4.8}$$

This constant is defined as the fraction of the input electrical energy that is mechanically deliverable.

To enter these equations into the block diagram, we rewrite Equation (4.7) as

$$T_3 = \frac{Y_{33}}{1-k^2}\left(S_3 - \frac{1}{nlw}\frac{d_{33}}{\varepsilon_{33}}q\right) \tag{4.9}$$

The block diagram corresponding to these relationships is shown in Figure 4.5. The displacement in the structure induces a strain in the actuator according to

$$S_3 = K_1 x \tag{4.10}$$

Similarly, the force applied to the structure by the actuator is derived from the stress in the actuator according to

$$f_a = K_2 T_3 \tag{4.11}$$

The constants K_1 and K_2 depend on the coupling between the actuator and the structure. They are determined by the location of the actuator, configuration of the actuator, bonding layers, modal coupling coefficients of the structure, and other factors.

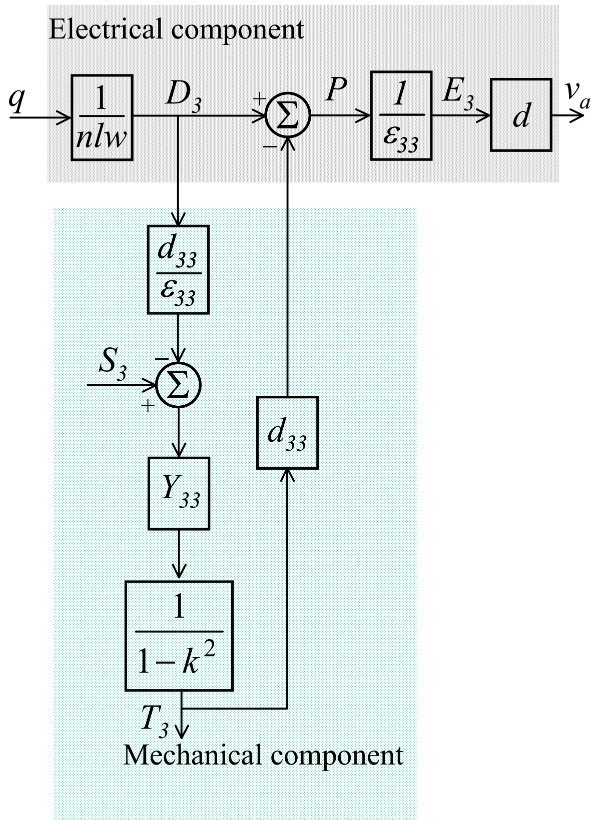

Figure 4.5. Electromechanical model of piezoelectric actuator

If we interpret the physical system represented by Figure 4.54 to be a stacked actuator (Figure 4.4) bonded rigidly to a mass, then the constants K_1 and K_2 are given by

$$K_1 = \frac{1}{nd} \qquad (4.12)$$
$$K_2 = lw$$

Equations (4.10) and (4.11) allow us to couple the actuator equations in Figure 4.5 to the dynamics of the structure in Figure 4.3. The complete model is shown in Figure 4.6. The model shown in Figures 4.5 and 4.6 has been derived from the linear, coupled constitutive equations (Equation (4.2)). The modifications in the model to account for the anhysteretic nonlinearity between the polarization and the electric field are described in the following section.

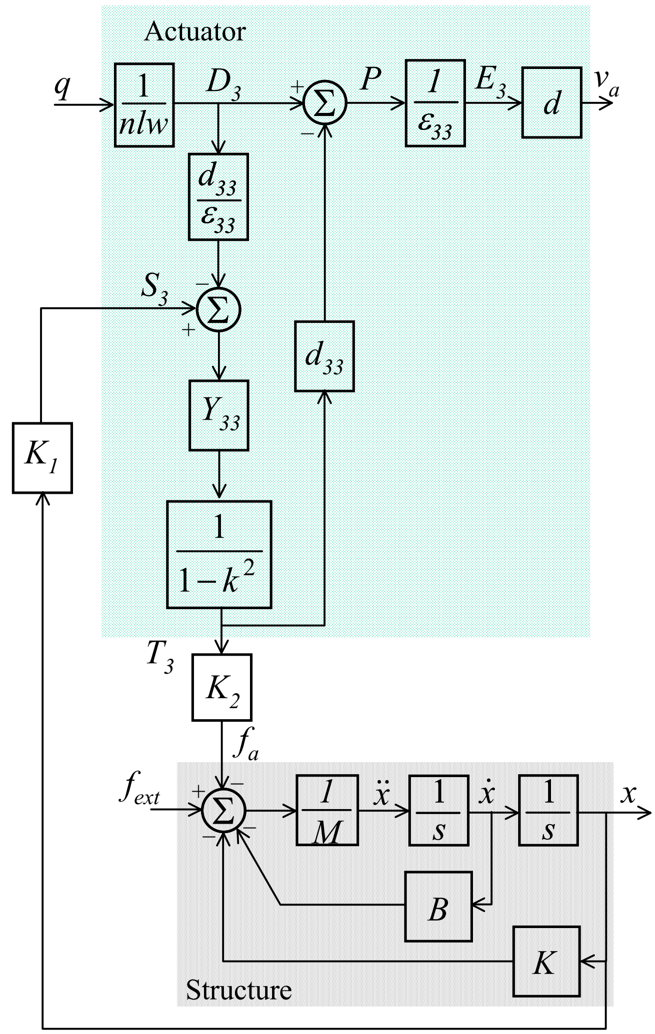

Figure 4.6. Complete electromechanical model of actuator-structure

4.3 ANHYSTERETIC NONLINEARITY

In the absence of interdomain coupling, the anhysteretic nonlinearity according to the Ising spin model between the polarization P, and the electric field E_3, in the actuator is given by [59]

$$P = P_s \tanh\left(\frac{E_3}{a}\right) \tag{4.13}$$

where, P_s is the saturation polarization of the material of the actuator and a is a scaling electric field. However, in the block diagram shown in Figure 4.6 electric field in the actuator is determined from the polarization. Hence, inverting the nonlinearity given by

Equation (4.13) to conform to the block diagram shown in Figure 4.6, the electric field is determined as

$$E_3 = a\tanh^{-1}\left(\frac{P}{P_s}\right) \tag{4.14}$$

This nonlinearity is shown graphically in Figure 4.7.

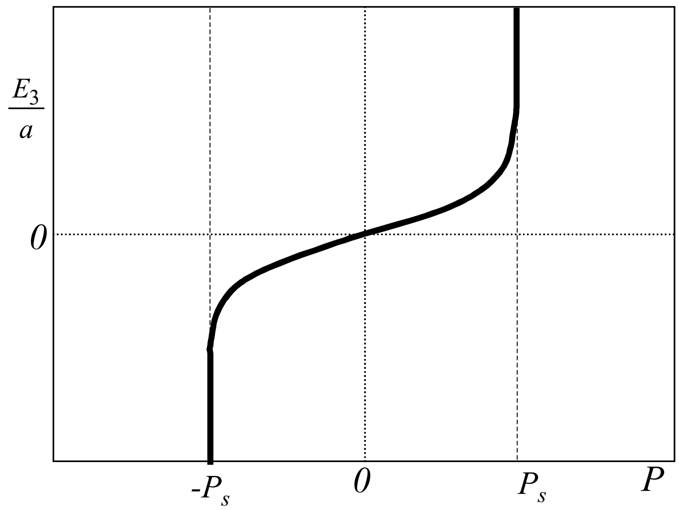

Figure 4.7. Inverse nonlinearity between polarization and electric field

The block diagram of the electromechanical model of the actuator and the structure with the nonlinearity is shown in Figure 4.8. Under the assumption that the polarization *p*, does not exceed the saturation polarization P_s a power series expansion can be used to represent the nonlinearity given by Equation (4.14). This power series expansion for the electric field is given by

$$E_3 = a\left[\left(\frac{P}{P_s}\right) + \frac{1}{3}\left(\frac{P}{P_s}\right)^3 + \frac{1}{5}\left(\frac{P}{P_s}\right)^5\right] \tag{4.15}$$

The actuator model can be represented as a cascade combination of a linear transfer function between the charge and polarization and the nonlinearity between the polarization and the voltage as shown in Figure 4.9.

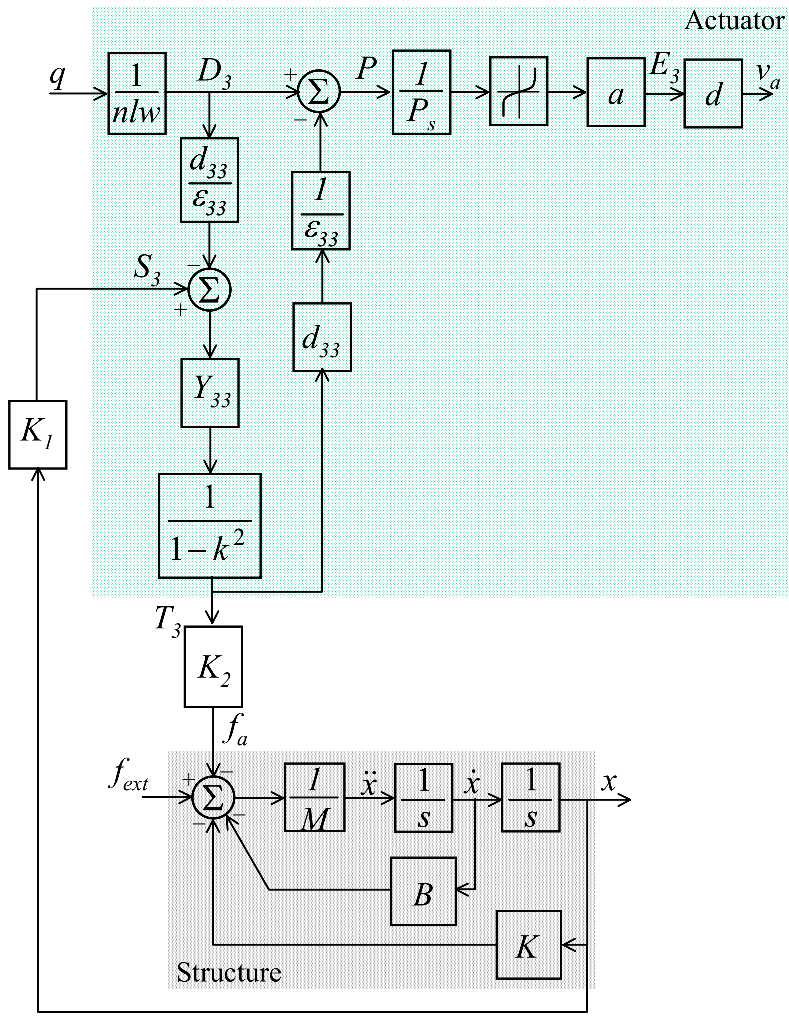

Figure 4.8. Electromechanical model of actuator-structure with nonlinearity

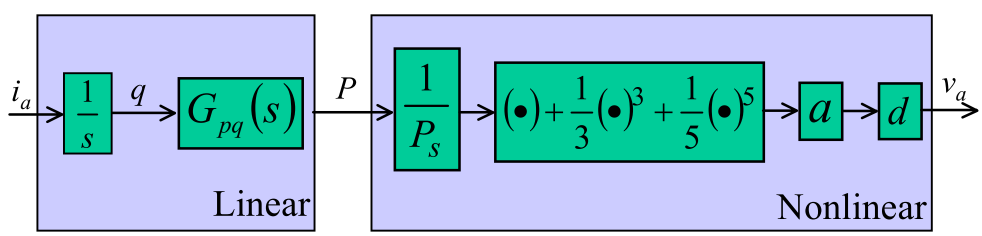

Figure 4.9. Actuator model as a cascade combination of linear and nonlinear systems

It is clear from Figure 4.9 that if the input signal to the nonlinearity is a sinusoid, the output signal will not be purely sinusoidal, but will contain third and fifth harmonics in addition to the fundamental component due to the nonlinearity. Since the actuator current and the polarization are related by a linear transfer function, the polarization is sinusoidal at the same frequency as the actuator current. Hence, if the actuator current is given by

$$i_a(t) = I_{\max}\cos(\omega t) \tag{4.16}$$

the polarization can be represented as

$$P(t) = P_m\cos(\omega t + \phi) \tag{4.17}$$

The voltage v_a, at the terminals of the actuator, from Figure 4.9, is then given by

$$v_a(t) = d\,a\left[\left(\frac{P_m}{P_s}\right)\cos(\omega t + \phi) + \frac{1}{3}\left(\frac{P_m}{P_s}\right)^3\cos^3(\omega t + \phi) + \frac{1}{5}\left(\frac{P_m}{P_s}\right)^5\cos^5(\omega t + \phi)\right] \tag{4.18}$$

Using trigonometric identities it can be easily shown that v_a consists of the fundamental, third and fifth harmonics and can be expressed as

$$v_a(t) = d\,a\left[V_{m1}\cos(\omega t + \phi) + V_{m3}\cos(3\omega t + 3\phi) + V_{m5}\cos(5\omega t + 5\phi)\right] \tag{4.19}$$

where,

$$\begin{aligned} V_{m1} &= \frac{1}{8}\left[8\left(\frac{P_m}{P_s}\right) + 2\left(\frac{P_m}{P_s}\right)^3 + \left(\frac{P_m}{P_s}\right)^5\right] \\ V_{m3} &= \frac{1}{96}\left[8\left(\frac{P_m}{P_s}\right)^3 + 6\left(\frac{P_m}{P_s}\right)^5\right] \\ V_{m5} &= \frac{1}{80}\left(\frac{P_m}{P_s}\right)^5 \end{aligned} \tag{4.20}$$

4.4 SUMMARY

An electromechanical model of a stacked piezoelectric actuator was developed in this section. A simple mass-spring-damper system was chosen to be the coupling mechanical structure. The linear model was developed from the linear, piezoelectric constitutive equations. The nonlinear model was then obtained by modifying the linear model to account for the anhysteretic nonlinearity between the polarization and the electric field.

5 OPTIMIZATION OF THE DRIVE AMPLIFIER

5.1 INTRODUCTION

The formulation of an optimization problem for the design of the drive amplifier for the piezoelectric actuator is the subject of this chapter. Switching power amplifiers are beginning to be recognized as promising alternatives for driving piezoelectric actuators [25-30]. It was shown in the previous chapter that these actuators exhibit capacitive electrical characteristics. In addition, it was shown that these actuators exhibit a hysteretic nonlinearity between the polarization and the electric field. Due to the reactive undamped electrical characteristics of the actuator, the drive amplifier is required to process almost zero real power and a considerable amount of reactive power circulates between the actuator and the amplifier.

The use of switching power amplifiers for driving piezoelectric actuators was discussed in [25-30]. High voltage switching amplifiers for piezoelectric actuators are discussed in [25,26]. The switching amplifiers for electrostrictors are reported in [27]. It has been noted that charge and current controlled amplifiers naturally reduce the distortion induced by the nonlinearities of the piezoelectric actuator [30,31]. A similar result for electrostrictor actuators has been reported in [28,29]. This reduced distortion can have beneficial effects on the performance of the control system. Hence, the drive amplifier discussed in this chapter is configured as a current controlled amplifier. The topology of the amplifier chosen is that of a single-phase DC-AC inverter with a filter inductor connected on the AC side. The switching devices in the amplifier are controlled using the principle of pulse width modulation.

Optimization of drive electronics for piezoelectric actuators was addressed in [32]. However, a well-defined optimization procedure that takes into account the nonlinear characteristics of the actuator and yields physically meaningful designs of the individual components of the amplifier has not been proposed. The optimization formulation presented in this chapter is a first step in this direction.

5.2 PROBLEM DEFINITION

A switching amplifier driving a piezoelectric actuator attached to the structure is shown in Figure 5.1. The goal of the optimization procedure is to design the amplifier such that it has minimum weight for the given actuator and structure. It is assumed that the amplifier is configured as a current controlled amplifier. That is, the actuator is controlled by controlling the current flowing into it that is proportional to i_{ref}. (The actuator is not controlled by the voltage across it.)

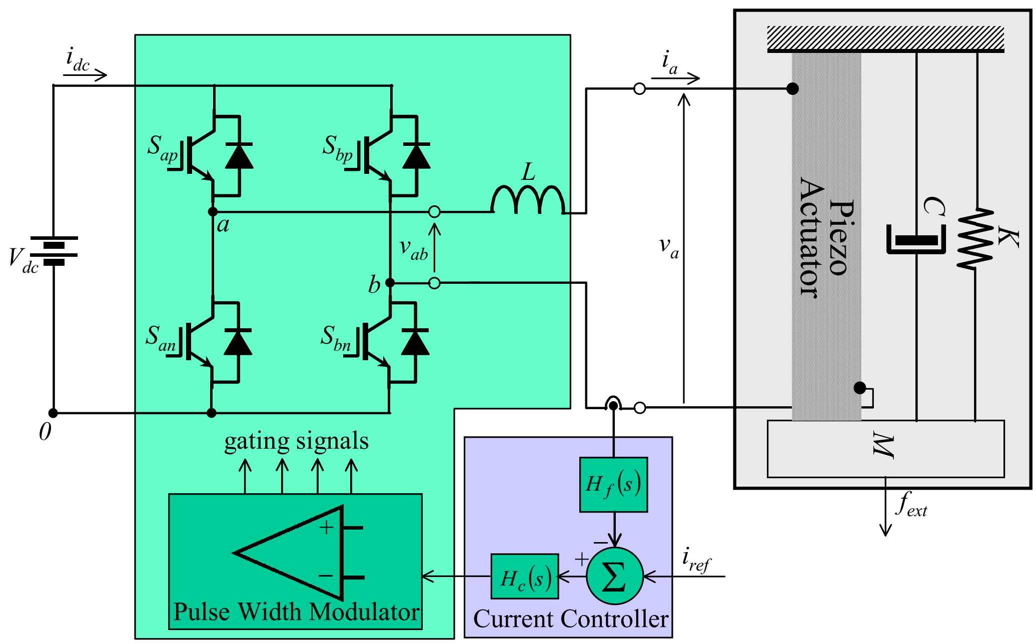

Figure 5.1. System Under Consideration

In the frequency domain, this performance specification is defined in the form of a transfer function shown in Figure 5.2.

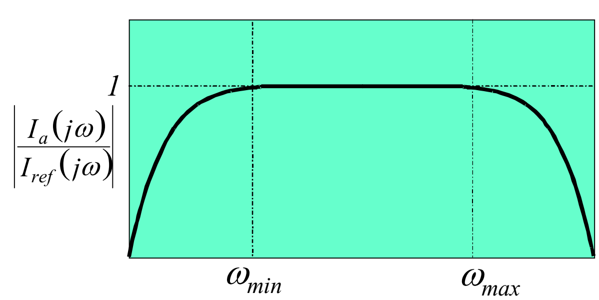

Figure 5.2. Regulation Specifications of Current Controller

It can be seen that the zero frequency is excluded from the passband in this amplifier topology. Clearly, this specification defines the frequency band over which the structure can be controlled. This data is part of the problem definition including frequencies ω_{min} and ω_{max}, which define the bandwidth of operation.

The amplifier is required to be able to drive the actuator to full stroke over the entire operational frequency range. Since the constitutive equations of the piezoelectric material has a saturation characteristic, this assumption implies that the amplifier must be able to deliver a maximum current over all frequencies in the bandwidth of the amplifier. This maximum current will be calculated below using a nonlinear model of the piezoelectric constitutive equations. This maximum current determines the required value of the bus DC voltage.

The main components of the amplifier are: 1) the switching power devices with the pulse width modulator, 2) the current controller, and 3) the inductor. The selection of the power devices is driven by several implementation issues including voltage ratings, thermal dissipation, cost, etc. However, these transistors all tend to be about the same size and weight. Since the performance of the amplifier is of primary concern, ideal switches in the optimization formulation replace the semiconductor switching devices. Hence, thermal considerations such as the design of the heat sink are excluded from the optimization problem.

The design of the current controller is largely driven by the frequency domain requirement on the amplifier given in Figure 5.2. That is to say, the current controller can be readily determined once the value of the inductance is known. Furthermore, the components of the current controller have a negligible contribution to the weight of the amplifier. Therefore, the current controller is also excluded from the optimization.

Hence the optimization problem presented in this chapter is specifically focused on the design of the inductor. Indeed, the inductor is by far the largest component over which the designer has control, and its value is impacted by the other parameters of the amplifier. Similar to the optimization of the sample system described in Chapter 3, the actual physical design of the inductor is considered, not only the selection of the inductance value.

The power transistor switches are used to control the average voltage and current that is delivered to the actuator. Due to the switching of these transistors, a ripple voltage and a ripple current ride on top of these average waveforms. This ripple current acts as a disturbance signal on the actuator causing high frequency excitation and unwanted heating in the actuator. The magnitude of the ripple current is determined by the inductor size and the switching frequency of the amplifier. In the optimization process the maximum allowable ripple current is a constraint.

The formulation of the optimization problem consists of the following steps:

1. Modeling the actuator and the amplifier
2. Calculation of the DC bus voltage and current ripple
3. Identification of the design variables
4. Definition of the optimization constraints
5. Definition of the objective function

Each of these steps is described in detail in the following sections.

It is straightforward to formulate the optimization problem. The main challenge is the determination of the current ripple. The current ripple can be ascertained from a simulation of the system in Figure 5.1, which includes the switching dynamics of the semiconductor power devices. These simulations are, however, computationally very expensive. Any optimization methodology that includes such a simulation would take prohibitively long to run. Therefore, it is necessary to develop a computationally cheap estimate of the switching ripple. A substantial amount of this chapter is devoted to this task.

5.3 MODEL DEVELOPMENT

The development of the coupled nonlinear electromechanical model of the actuator and the structure to be used for the optimization problem was described in the previous chapter. The modeling of the drive amplifier shown in Figure 5.1 is briefly described in this section. The modulation algorithm and the switching waveform, which it engenders, are discussed. Then a simpler, "average' model of the power stage is introduced. A detailed description of the drive amplifier used in this discussion is shown in Figure 5.3.

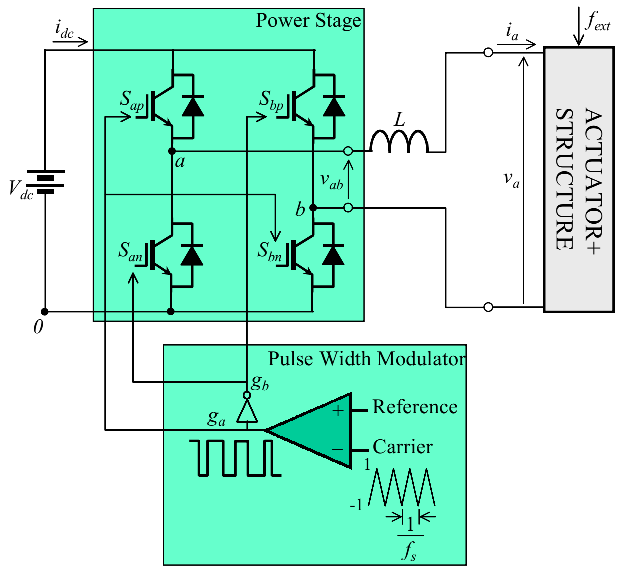

Figure 5.3. Single phase DC-AC inverter driving the actuator

In this amplifier, the current driving the piezoelectric actuator is synthesized by pulse width modulating the voltage from the DC source by appropriately controlling the semiconductor switches with the pulse width modulator. The inductor (in conjunction with the capacitive actuator load) filters the pulse width modulated voltage to deliver a current to the load that contains a fundamental component that is proportional to the reference input signal and that contains an acceptably small ripple.

A bipolar voltage v_{ab}, is synthesized from the DC voltage source V_{dc}, by operating the switches S_{ap}, S_{an}, S_{bp} and S_{bn} according to a technique called pulse width modulation (PWM)[60]. A reference signal is modulated with a triangular wave called the carrier signal as shown in Figure 5.4.

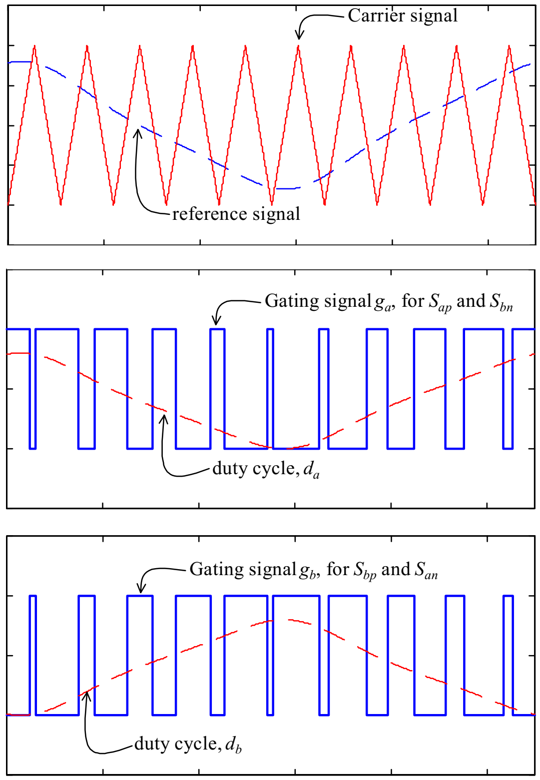

Figure 5.4. Pulse Width Modulation (PWM)

The frequency of the carrier signal is the switching frequency of the amplifier. The signals g_a and g_b are the gating signals generated by the pulse width modulator to drive the four switches of the amplifier. The gating signal g_a, turns on the switches S_{ap} and S_{bn} when the reference signal becomes greater than the carrier signal and turns them off when the reference signal becomes lesser than the carrier. The gating signal g_b, for S_{bp} and S_{an} is the logical inverse of the drive signal to S_{ap} and S_{bn}.

The voltage v_{ab}, shown in Figure 5.5, at the output of the amplifier is then given by

$$\begin{aligned} v_{ab} &= \begin{cases} V_{dc} & \text{when } S_{ap} \text{ and } S_{bn} \text{ are on} \\ -V_{dc} & \text{when } S_{bp} \text{ and } S_{an} \text{ are on} \end{cases} \\ &= g_a V_{dc} - g_b V_{dc} \end{aligned} \tag{5.1}$$

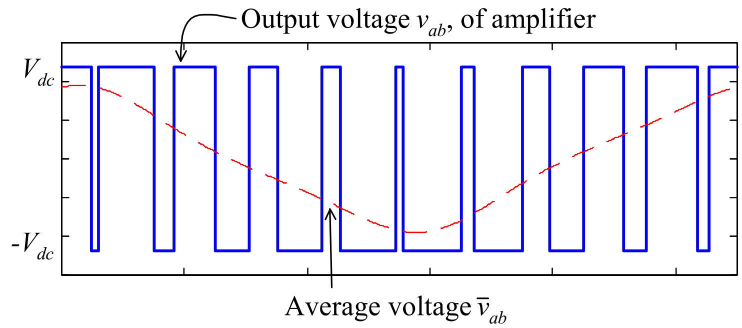

Figure 5.5. Pulse width modulated voltage v_{ab} and its average value $\bar{v}_{ab}$

The duty cycle of the gating signal is the fraction of the period for which the gating signal is high. The average value of the amplifier output can be obtained from (5.1) by replacing the control signals for the switches with the equivalent duty cycles of the gating signals as follows

$$\bar{v}_{ab}(t) = (d_a(t) - d_b(t))V_{dc} = d_{ab}(t)V_{dc} \tag{5.2}$$

From Equation (5.2), it can be seen that the duty cycles d_a and d_b can be replaced by a single duty cycle d_{ab} which multiplies the input DC voltage to obtain the average of the output voltage of the amplifier. Since the duty cycle d_{ab} cannot exceed unity, the maximum amplitude of the average value of the output voltage is equal to V_{dc}.

A typical waveform of this actuator current i_a is shown in Figure 5.6 where it is assumed that the reference input signal is sinusoidal.

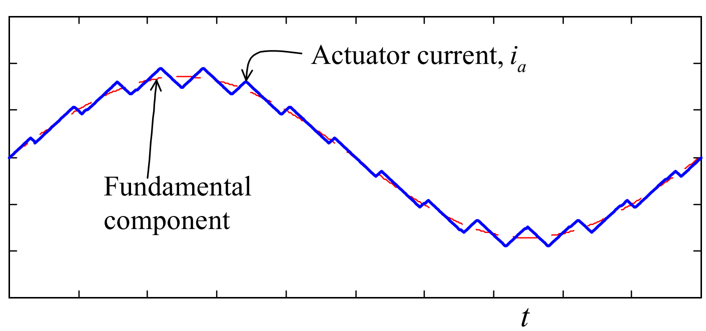

Figure 5.6. Typical waveform of current generated by the drive amplifier

It can be seen that the actuator current is nearly sinusoidal at the reference frequency. The deviation of the actual current from the desired fundamental component is called the switching ripple. It can be also shown that the average value of the input current to the amplifier is given by

$$\bar{i}_{dc}(t) = d_{ab}(t) i_a(t) \tag{5.3}$$

5.3.1 Average Model of Amplifier

In order to incorporate a model of the switching amplifier into the optimization process, it is necessary to replace the switches to make the model computationally tractable. This simplified model, called an average model, neglects the switching ripple in the currents and voltages and reduces the model to a set of relationships between the average waveforms. This model is valid only over frequency ranges significantly lower than half the switching frequency of the amplifier [57]. The average model is shown in Figure 5.7.

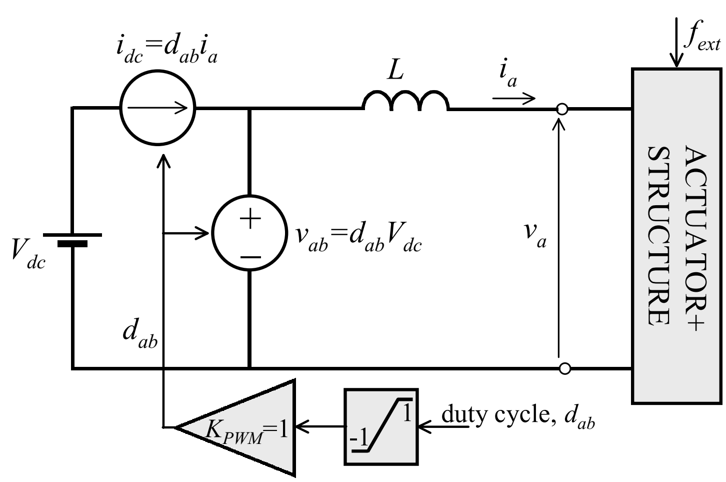

Figure 5.7. Average model of amplifier driving the actuator

A transfer function representation of the amplifier can be very easily obtained from the average model. A control block diagram representation coupling the models of the amplifier and the actuator is shown in Figure 5.8.

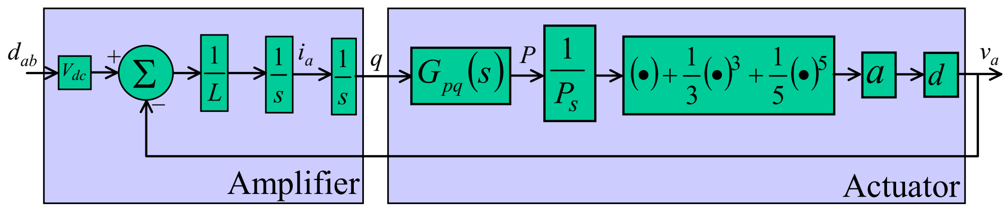

Figure 5.8. Block diagram of amplifier coupled to the actuator

The final component of the amplifier is the current controller. The block diagram of the closed loop system with a generic representation of the current controller is shown in Figure 5.9.

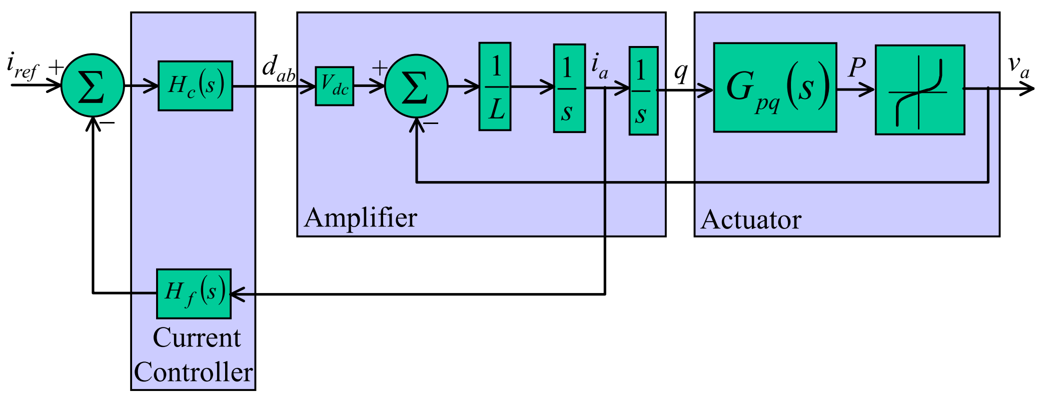

Figure 5.9. Block diagram of amplifier and actuator with current controller

This controller uses the current into the actuator as feedback to create an error signal with a reference input signal. The duty cycle command is then synthesized from the error signal. The current controller ensures that the fundamental component of the actuator current follows the reference over the regulation bandwidth of the amplifier. In the analysis that follows, it is assumed that the fundamental component of the actuator current is identical to the reference current command.

The controller uses the current into the actuator as feedback to create an error signal with the reference input signal. The duty cycle command is then synthesized from the error signal. The design of the current controller depends on the inductance L, actuator specifications, DC input voltage V_{dc} and the switching frequency f_s. Given these parameters of the amplifier and the actuator, it is a straightforward exercise to design the current controller.

In most cases, the current controller can be implemented with analog operational amplifier circuits, whose weight is negligible compared to the weight of the overall system. Furthermore, the weight of the current controller is independent of the control gains. Therefore, the design of the current controller is excluded from the optimization formulation.

5.4 DETERMINATION OF DC BUS VOLTAGE

One of the requirements of the amplifier is to drive the actuator to full stroke over the bandwidth of the system. This requirement implies that the amplifier must produce enough current to saturate the piezoelectric amplifier when the duty cycle of the amplifier is at its maximum value. This current requirement, in turn, places a restriction on the minimum bus voltage V_{dc}. The minimum DC bus voltage is related to the inductance, and a simple expression that describes this relationship is required for the optimization methodology. The average model of the amplifier is used to determine the DC bus voltage neglecting the switching ripple in the actuator current and the voltage. This assumption is validated by the fact that the electromechanical power transfer between the amplifier and the actuator predominantly occurs at the frequency of the reference sinusoidal current, which is much lower than the switching frequency. The determination of the DC bus voltage goes through the following steps. First, the maximum current drawn by the actuator is determined. From this current, the voltage across the actuator using the nonlinear model is determined. The amplifier output voltage $\overline{v}_{ab}$, is then calculated as the sum of the actuator voltage and the voltage drop across the inductance. The DC bus voltage is finally determined such that the duty cycle does not exceed unity when $\overline{v}_{ab}$ reaches its maximum amplitude.

A simplified block diagram of the average model of the amplifier and the actuator with the nonlinearity is shown in Figure 5.10.

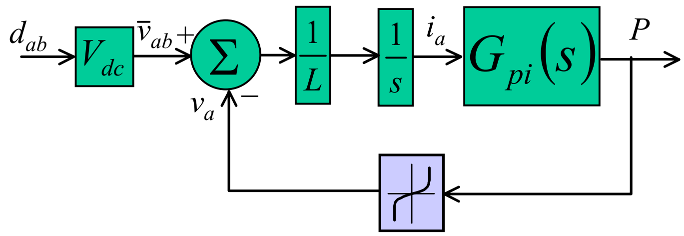

Figure 5.10. Simplified block diagram of amplifier-actuator with nonlinearity

To start with, it is assumed that the reference current command is selected to drive the actuator at its maximum deflection. As mentioned in the previous section, the current controlled amplifier is configured such that the fundamental component of the actuator current is identical to the reference current. (Figure 5.2). Let this sinusoidal current be given by

$$i_{ref}(t) = I_{\max}\cos(\omega_F t) = i_a(t) \tag{5.4}$$

where, ω_F is the frequency that results in the maximum deflection. From Figure 5.10, it can be seen that the actuator current and polarization are linearly related by a transfer function $G_{pi}(j\omega)$, whose magnitude response is shown in Figure 5.11. Hence, for the actuator current given by Equation (5.4), the polarization can be expressed as

$$P(t) = P_s\cos(\omega_F t + \phi) \tag{5.5}$$

since the actuator is being driven to its maximum deflection.

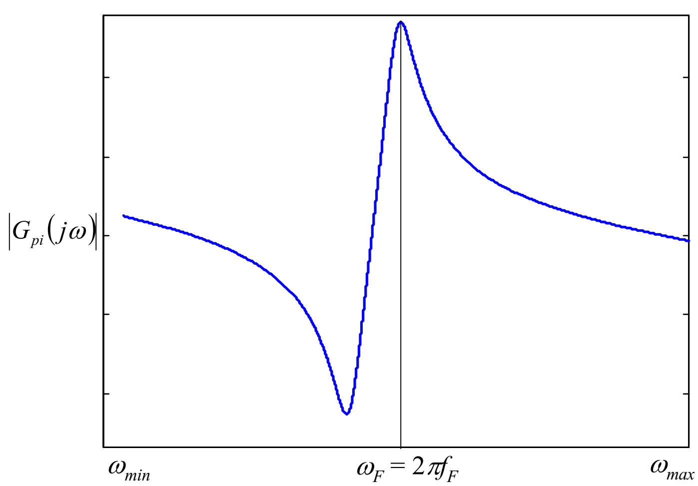

Figure 5.11. Actuator current to polarization transfer function

(In this case, the amplifier bandwidth is assumed to include the mechanical resonant frequency of the structure.) Using the relationship in Figure 5.11 between the current and polarization, the maximum current amplitude can be obtained as

$$I_{\max} = \frac{P_s}{G_{PI}\left(j\omega_F\right)} \tag{5.6}$$

The next step is to determine the voltage across the actuator using the nonlinear constitutive equations of the piezoelectric material. Given the polarization in Equation (5.5) the actuator voltage, due to the nonlinearity, consists of the fundamental, third and fifth harmonics according to Equations 4.18, 4.19 and 4.20, because of the nonlinearity. Substituting $P_m = P_s$ in Equation (4.20), we obtain

$$v_a(t) = d\,a\left[\frac{11}{8}\cos(\omega_F t+\phi)+\frac{7}{48}\cos(3\omega_F t+3\phi)+\frac{1}{80}\cos(5\omega_F t+5\phi)\right] \tag{5.7}$$

The voltage $\bar{v}_{ab}$, at the output of the amplifier is the sum of the actuator voltage and the drop across the inductor given by. This is given by

$$\bar{v}_{ab}(t) = L\frac{di_a(t)}{dt} + v_a(t) \tag{5.8}$$

Substituting for $i_a(t)$ from Equation (5.4) and for $v_a(t)$ from Equation (5.7), we obtain

$$\begin{aligned}\bar{v}_{ab}(t) = d\,a&\left[\frac{11}{8}\cos(\omega_F t+\phi)+\frac{7}{48}\cos(3\omega_F t+3\phi)+\frac{1}{80}\cos(5\omega_F t+5\phi)\right]\\ &+\omega L I_{\max}\sin\left(\omega_F t\right)\end{aligned} \tag{5.9}$$

It can be seen from Equation (5.9) that, in order to guarantee the sinusoidal actuator current given by Equation (5.4), the current controller (Figure 5.9) needs to synthesize a duty cycle command d_{ab}, such that the third and fifth harmonic components of the amplifier output voltage $\bar{v}_{ab}$, are identical to those of the actuator voltage v_a. According to Equation (5.2), the duty cycle $d_{ab}(t)$ can be written as

$$d_{ab}(t) = \frac{1}{V_{dc}}\bar{v}_{ab}\left(t\right) \tag{5.10}$$

The minimum DC bus voltage required is then determined such that the duty cycle given by Equation (5.10) does not exceed its maximum allowable amplitude $d_{ab,\max}$ when the amplifier output voltage $\bar{v}_{ab}$, reaches its maximum amplitude. The minimum DC bus voltage is hence obtained as

$$V_{dc} = \frac{1}{d_{ab,\max}} \max[\bar{v}_{ab}(t)] \tag{5.11}$$

5.5 ESTIMATION OF ACTUATOR CURRENT RIPPLE

The next step in the analysis is to determine the current ripple. Specifications on the harmonic content of the actuator current are used as optimization constraints to determine the values of inductance and switching frequency. This analysis is complicated by the nonlinear constitutive equations of the actuator. One approach for determining the current ripple is to directly simulate the nonlinear system. This method is computationally too expensive for optimization, however. Therefore, the size of the current ripple is estimated by computing the amplitudes of the components of the Fourier series of the actuator current.

The switching of the power transistors causes the voltage v_{ab} in Figure 5.5 to be a pulse width modulated square wave. The Fourier decomposition of the voltage v_{ab} can be given as,

$$v_{ab}(t) = \sum_{k=1}^{\infty} V_{abk} \cos(\omega_k t + \vartheta_k) \tag{5.12}$$

A typical harmonic spectrum of the amplifier output voltage is shown in Figure 5.12. The first, third and the fifth harmonics of the voltage v_{ab}, are given by Equation (5.8). Since the actuator current has no third and fifth harmonics, the third and fifth harmonic components of the amplifier output voltage v_{ab}, are identical to those of the actuator voltage v_a, and do not contribute to the ripple in the actuator current. Hence, the ripple in the actuator current is due to the voltage harmonics whose frequencies are in the switching frequency range.

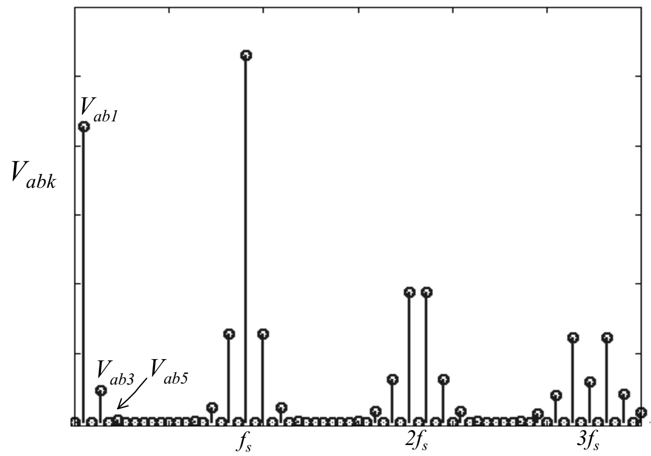

Figure 5.12. Harmonic spectrum of amplifier output voltage v_{ab}

The Fourier decomposition of the actuator current can be expressed as

$$i_a = I_{\max}\cos(\omega_F t) + \sum_{k=2}^{\infty} I_{ak}\cos(\omega_k t + \theta_k) \tag{5.13}$$

It is assumed that the fundamental component of the actuator current i_a is identical to i_{ref}. The polarization and actuator voltage can also be expressed in a similar fashion as

$$P(t) = P_s\cos(\omega_F t + \phi) + \sum_{k=2}^{\infty} P_k\cos(\omega_k t + \phi_k) \tag{5.14}$$
$$v_a(t) = \sum_{k=1}^{\infty} V_{ak}\cos(\omega_k t + \varphi_k)$$

The harmonic components of v_a for k=1,3 and 5 are given by Equation (5.7). In the following analysis, complex phasor notation of sinusoidal steady state variables is used to determine the Fourier components of the actuator current. Rewriting Equation (5.8) in complex phasor notation,

$$V_{abk}e^{j\vartheta_k} = V_{ak}e^{j\varphi_k} + \omega_k L I_{ak} e^{j\left(\theta_k + \frac{\pi}{2}\right)} \tag{5.15}$$

The amplitudes I_{ak}, of the actuator current are then obtained from Equation (5.15) as

$$I_{ak} = \frac{1}{\omega_k L}\left(V_{abk} e^{j\left(\vartheta_k - \theta_k - \frac{\pi}{2}\right)} - V_{ak} e^{j\left(\varphi_k - \theta_k - \frac{\pi}{2}\right)} \right) \tag{5.16}$$

To obtain the Fourier series components of the actuator current, the corresponding components of the actuator voltage are required according to Equation (5.16). Typical switching waveforms of the actuator current, actuator voltage and the polarization are shown in Figure 5.13. It can be seen that the polarization and the voltage across the actuator have negligible switching ripple. The reasons for this are explained in the following.

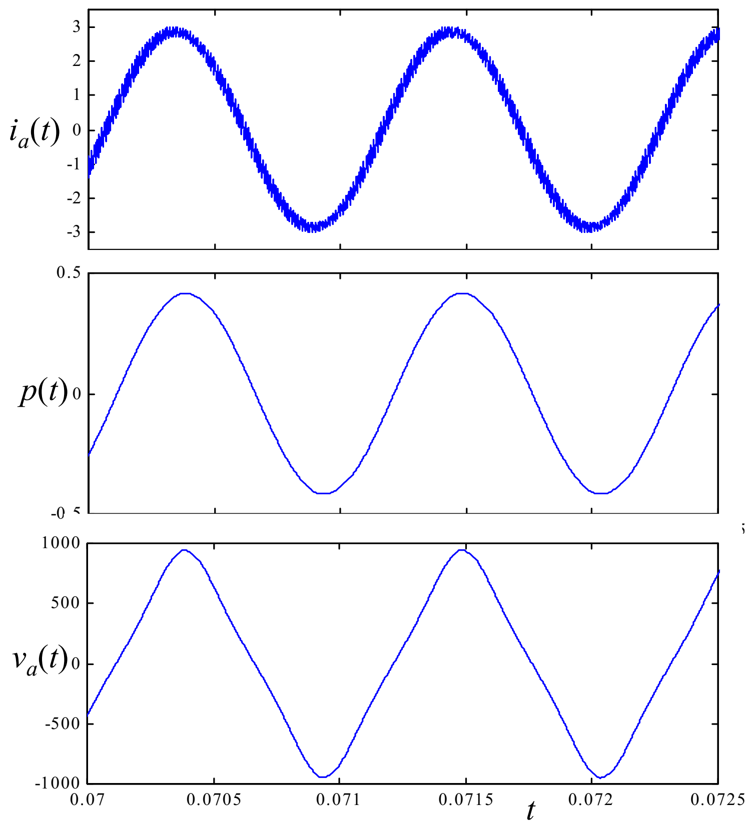

Figure 5.13. Switching waveforms of actuator current i_a, duty cycle d_{ab}, and actuator voltage v_a.

An expanded view of magnitude of the transfer function $G_{pi}(s)$, from the actuator current to the polarization is shown in Figure 5.14. Since the switching frequency has to be significantly higher than ω_{max}, it can be seen from Figure 5.14, that harmonics of the current in the switching frequency range are sufficiently attenuated by the actuator. Hence, it can be assumed that the harmonic components at the switching frequency range of the polarization are equal to zero.

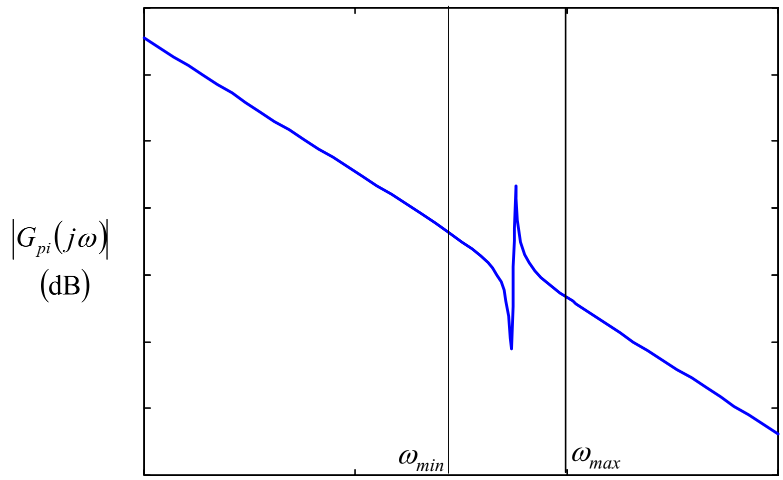

Figure 5.14. Expanded of transfer function $G_{pi}(s)$ from actuator current to polarization

In addition, the actuator voltage can also be assumed to be devoid of any components in the switching frequency range. As a result, we have

$$P_k = 0 \text{ for } k \geq 2 \qquad (5.17)$$
$$V_{ak} = 0 \text{ for } k \geq 6$$

Hence, (5.16) reduces to

$$I_{ak} = \frac{1}{\omega_k L} V_{abk} \text{ for } k \geq 6 \qquad (5.18)$$

5.6 FORMULATION OF OPTIMIZATION PROBLEM

The optimization methodology is now formulated using the calculations in the previous sections. The design variables are identified, the constraints are set up and the objective function is defined.

5.6.1 Design Variables

The design variables for the optimization problem are the variables associated with the design of the inductor. The inductors are assumed to be typical EE cores as in the optimization formulation of sample system described in Chapter 3. The design variables associated with the inductor are given in Table 5.1.

Table 5.1. Design variables associated with inductor design

Variable name	Description
n	Number of turns
A_{cp}	Cross sectional area of winding
C_w	Center leg width
W_w	Window width
l_g	Airgap length

5.6.2 Constraints

The optimization constraints are subdivided into performance and physical constraints as explained in the following subsections.

Performance Constraints

Total Harmonic Distortion of Actuator Current

The first performance constraint is the maximum allowable current ripple. Because the current ripple is a nonlinear function, the actuator current is expressed as a Fourier series (Equation (5.13)), and then the current ripple is measured as total harmonic distortion. The *THD* is the percentage ratio of the distortion component of the actuator current to its fundamental component [60]. It is defined as

$$THD = 100\frac{I_{dis}}{I_{a1}} \tag{5.19}$$

where, I_{a1} is the rms value of the fundamental component of the actuator current and I_{dis} is the rms value of the distortion component. The fundamental component of the actuator current is assumed to be identical to the reference command. According to Equation (5.13), the distortion component is given by

$$I_{dis} = \sum_{h=2}^{\infty}\frac{I_{ak}^2}{2} \tag{5.20}$$

Hence, the *THD* of the amplifier used at full capacity can be expressed as

$$THD = 100\sqrt{\frac{\sum_{k=2}^{\infty} I_{ak}^2}{I_{\max}^2}} \tag{5.21}$$

An upper bound is imposed on the *THD* of the actuator current to size the inductor at the specified switching frequency.

The *THD* of the actuator current is a function of the switching frequency and the amplitude and the frequency of the fundamental component of the actuator current. To begin with, the switching frequency is fixed at a specified value. The amplitude and frequency of the fundamental component of the actuator current are determined from the mechanical model according to Equation (5.6) and Figure 5.11. The average amplifier output voltage $\bar{v}_{ab}$ then is determined for this maximum current amplitude from Equation (5.9). The DC bus voltage is then determined from Equation (5.11) using the maximum duty cycle. For this DC bus voltage the duty cycle d_{ab}, is determined from Equation (5.10). This duty cycle is then modulated with the triangular carrier at the switching frequency as shown in Figure 5.4 to generate the pulse width modulated output voltage v_{ab} as shown in Figure 5.5. The Fourier components V_{abk}, of the pulse width modulated voltage v_{ab} are then determined. Finally, the Fourier series components of the actuator current are determined from Equation (5.16) where the inductance is determined from Equation (3.4). The *THD* of the actuator current is then determined from Equation (5.21).

Physical Constraints

The physical constraints are defined to guarantee physically meaningful dimensions for the core and windings used in the inductor and they are the same as those defined in Chapter 3.

5.6.3 Objective Function

The objective function is the weight of the inductor determined in a similar fashion to the Chapter 3. That is,

$$J = W_L \tag{5.22}$$

The weight of an inductor is determined as the sum of the weights of iron and copper used in the core and windings, respectively

$$W_L = W_{fe} + W_{cu} \tag{5.23}$$

5.7 OPTIMIZATION RESULTS

The results of the optimization problem are presented in this section. The bandwidth requirements and relevant specifications of the actuator are given below in Table 5.2.

Table 5.2. Operating Conditions

Variable	Value
Operating bandwidth	$\omega_{min} = 2\pi\, 700$ rad/sec $< \omega < \omega_{max} = 2\pi\, 1200$ rad/sec
Saturation Polarization, P_s	*0.425* C/m^2
Coercive Electric Field, a	*6.4* MV/m
Mass of Structure, M	*200* kg
Damping of Structure, B	2.56×10^4 N-s/m
Stiffness of Structure, K	5.4×10^9 N/m
DC Bus Voltage, V_{dc}	*1186* V (determined from Equation (5.11))

Optimization was performed using the VisualDOC optimization software [55] using the Modified Method of Feasible Directions algorithm [56]. The definition of the constraints and the objective function were coded in MATLAB. Constraint derivatives were computed using finite differences. Depending on the initial design used to start the optimization iterations, convergence was obtained within approximately 200 function evaluations. The optimizations were achieved in approximately 10 minutes on a 500 MHz Pentium II PC. For this problem, it was found that there were not any local minima in the design space, and the optimizer converged to the global minima irrespective of the choice of the initial design.

A family of optimal designs was obtained by varying the upper bound on the THD of the actuator current for switching frequencies of 100 kHz and 200 kHz. The inductance values plotted as a function of the THD of the actuator current for the two values of switching frequency is shown in Figure 5.15. It can be seen that the inductance increases as the upper bound on the THD decreases for a given switching frequency. In addition, the inductance value required to meet a given THD specification reduces as the switching frequency increases.

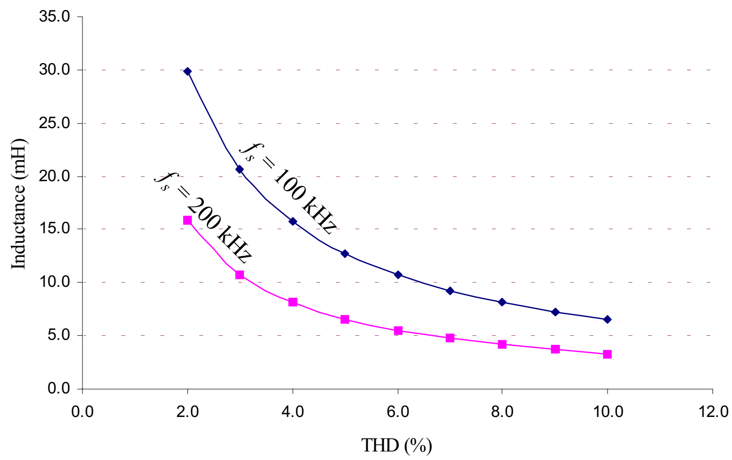

Figure 5.15. Inductance value *vs* THD of actuator current

The weight of the inductor as a function of the inductance value is plotted in Figure 5.16.

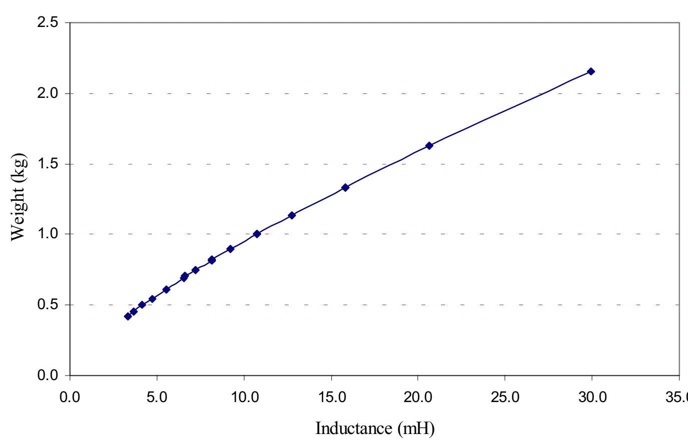

Figure 5.16. Weight of the inductor *vs* inductance value

The weight of an inductor is proportional to the energy stored, which in turn is proportional to inductance value and to the square of the peak inductor current. Since the peak current is approximately constant (determined by the maximum polarization), the weight of the inductance varies almost linearly with inductance.

5.8 SUMMARY

The problem of designing a minimum weight, current controlled switching amplifier for a piezoelectric actuator was discussed in this chapter. These results are partial in that the design of the heat sink is ignored. With this assumption the design of the amplifier reduces to the design of the inductor. Indeed, the inductor is the largest single component of the amplifier. An optimization methodology is formulated that takes into account the physical configuration of the inductor, the bandwidth of the amplifier, the effect of the ripple current and switching frequency on the sizing of the inductor. The optimization results demonstrate that the proposed optimization formulation provides an effective method to obtain physically meaningful results in a time efficient manner.

6 ACTIVE DAMPING USING PIEZOELECTRIC ACTUATORS

6.1 INTRODUCTION

In the chapter, a control law to make the piezoelectric actuator actively damp the structure is proposed. In this paper we show analytically that controlling the current through the actuator to be proportional to the acceleration of the structure naturally results in an increase in the damping of the mechanical system without a change to the stiffness of the structure. Specifically, it is shown analytically that controlling the current into the actuator to be proportional to the acceleration of the structure results in an increase in the damping of the mechanical structure without a change to the stiffness of the structure. The coupled electromechanical model of the actuator and the structure developed in Chapter 4, is used in this chapter for the development of the control law and for the analysis of its implications on the design of the drive amplifier and the power flow characteristics between the actuator and the amplifier. The structure is assumed to be acted on by an sinusoidal external disturbance force It is shown that, due to the active damping, the piezoelectric actuator absorbs mechanical power injected into the system by the external disturbance force and redirects it back to the electrical source. Hence, there is a net flow of electrical power from the actuator to the electrical source. In addition, due to the capacitive electrical characteristics of the actuators, there is a considerable amount of reactive power circulating between the actuator and the amplifier. A detailed analysis of the electromechanical power transfer characteristics is presented in this chapter. The anhysteretic nonlinearity in the actuator is, however, neglected in this analysis in order to exemplify the dependence of the power flow characteristics on the material properties of the actuator and the structure. Estimates of the peak current and voltage in the actuator are also determined. These peak values are used in the design of the drive amplifier.

6.2 ACTIVE DAMPING OF STRUCTURE

In this section, a control law to add damping to the structure shown in Figure 4.1 is presented. Beginning with the electromechanical model in Figure 4.6, it is shown that the natural control law to increase damping in the structure is acceleration feedback to a current controlled amplifier. From Figure 4.6, the force F_a exerted by the actuator on the structure is given by

$$
\begin{aligned}
f_a &= \frac{Y_{33}K_1K_2}{1-k^2}x - \frac{d_{33}}{\varepsilon_{33}}\frac{1}{nlw}\frac{Y_{33}K_2}{1-k^2}q \\
&= K_a x - \frac{d_{33}}{\varepsilon_{33}}\frac{1}{nlw}\frac{1}{K_1}K_a q
\end{aligned} \tag{6.1}
$$

where, K_a is the equivalent stiffness of the actuator and is given by

$$
K_a = \frac{Y_{33}K_1K_2}{\left(1-k^2\right)}\ . \tag{6.2}
$$

Substituting Equation (6.1) into Equation (4.1) we obtain

$$
M\ddot{x} + B\dot{x} + Kx = f_{ext} - K_a x + \frac{d_{33}}{\varepsilon_{33}}\frac{1}{nlw}\frac{1}{K_1}K_a q \tag{6.3}
$$

or

$$
M\ddot{x} + B\dot{x} + \left(K + K_a\right)x = f_{ext} + \frac{d_{33}}{\varepsilon_{33}}\frac{1}{nlw}\frac{1}{K_1}K_a q
$$

So the addition of the actuator to the system increases the stiffness of the structure as we expect.

Furthermore, Equation (6.3) also clearly shows how to introduce feedback from the structure to increase the damping. If the charge into the piezoelectric actuator is made a function of the velocity as

$$
q = -K_f\dot{x}, \tag{6.4}
$$

then the closed loop equation becomes

$$M\ddot{x}+\left(B+\frac{d_{33}}{\varepsilon_{33}}\frac{1}{nlw}\frac{1}{K_1}K_aK_f\right)\dot{x}+\left(K+K_a\right)x=f_{ext} \quad (6.5)$$

Differentiating Equation (6.4),

$$i_a=\dot{q}=-K_f\ddot{x} \quad (6.6)$$

which shows that the damping can also be increased by feeding back acceleration to current into the actuator. This configuration of the feedback law is attractive because current amplifiers are easier to construct than charge amplifiers. Also, the output signal of an accelerometer can be used without any integration. Of course, this control law will not work at zero frequency. That is, the control system will not act as a positioning system.

The block diagram of the complete system after introducing the acceleration feedback is shown in Figure 6.1. This block diagram assumes there is a current controlled amplifier with unity gain in the loop.

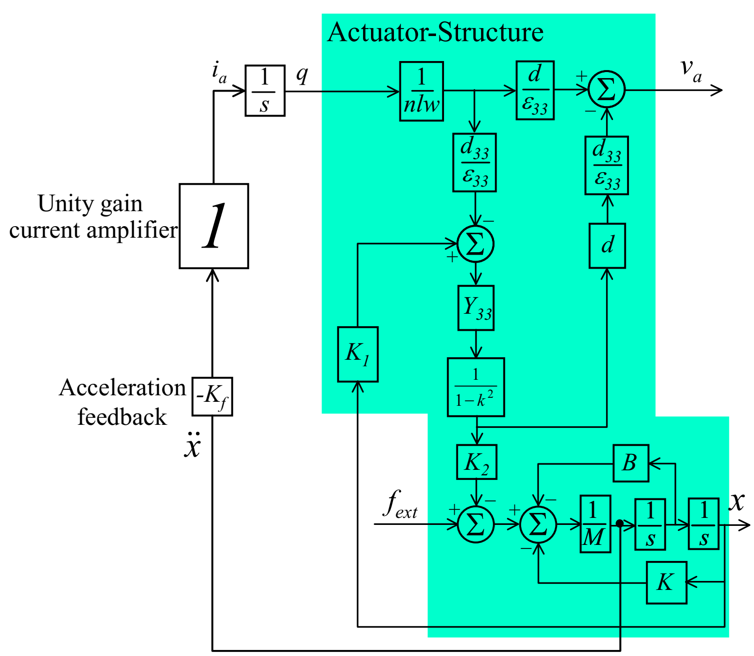

Figure 6.1. Block diagram of closed loop system

Rewriting Equation (6.5) in the standard form,

$$\ddot{x}+\left(B+\frac{d_{33}}{\varepsilon_{33}}\frac{1}{nlw}\frac{1}{K_1}K_aK_f\right)\frac{1}{M}\dot{x}+\left(\frac{K+K_a}{M}\right)x=\frac{1}{M}f_{ext} \tag{6.7}$$

$$\ddot{x}+2(\zeta+\zeta_a)\omega_n\dot{x}+\omega_n^2x=\frac{1}{M}f_{ext}$$

where,

$$\omega_n=\sqrt{\frac{K+K_a}{M}} \tag{6.8}$$

is the resonant frequency of the structure with the actuator,

$$\zeta=\frac{B/M}{2\omega_n} \tag{6.9}$$

is the damping of the uncontrolled structure and,

$$\zeta_a=\frac{\frac{d_{33}}{\varepsilon_{33}}\frac{1}{nlw}\frac{1}{K_1}K_aK_f\Big/M}{2\omega_n} \tag{6.10}$$

is the active damping added by the actuator.

Using Equation (6.2) the expression for the active damping ζ_a can be simplified as

$$\zeta_a=\frac{\frac{d_{33}}{\varepsilon_{33}}\frac{1}{nlw}\frac{1}{K_1}K_aK_f\Big/M}{2\omega_n}=\frac{\frac{d_{33}}{\varepsilon_{33}}\frac{1}{nlw}\frac{1}{K_1}\frac{Y_{33}K_1K_2}{1-k^2}K_f}{2\omega_nM} \tag{6.11}$$

Using the expressions for K_1 and K_2 from Equation (4.13), the active damping introduced by the controlled actuator can be reduced to

$$\zeta_a=\frac{1}{nd_{33}}\frac{k^2}{1-k^2}K_f\frac{1}{2\omega_nM} \tag{6.12}$$

Thus, making the current proportional to the acceleration of the structure introduces additional damping to the structure. The effects of actively damping the structure on the power flow between the external disturbance and the electrical input will be analyzed in the next section.

6.3 AMPLIFIER REQUIREMENTS

In the previous section, a control law to add damping to the structure was proposed. The primary electrical requirements of the amplifier needed to drive this system are determined in this section. First, the peak voltages and currents drawn by the actuator in closed loop are derived. These estimates are critical to the design of the amplifier. It is assumed that the structure is subjected to a sinusoidal disturbance force and the peak current and voltage are obtained from a frequency domain analysis. The damping of the uncontrolled structure ζ, is assumed to be zero. It can be shown the current and voltage in the actuator reach their maximum amplitudes when the frequency of the external force is ω_n. The following analysis is, in this sense, worst case.

In the previous section, it was shown that the proposed control law required a current controlled amplifier. A schematic of such an amplifier driving the actuator is shown in Figure 6.2.

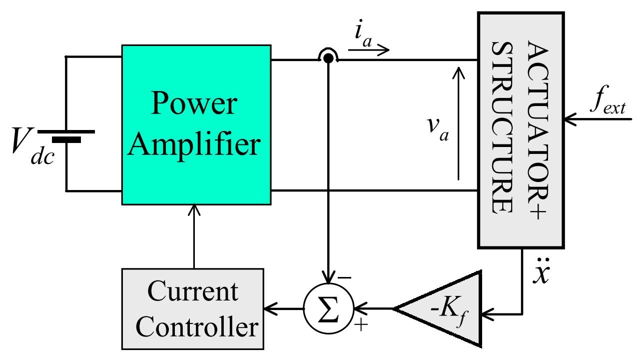

Figure 6.2. Schematic of amplifier driving the actuator

The amplifier is driven from a constant voltage source. It is forced by the current controller to synthesize the current to be driven into the actuator in response to the command from the acceleration feedback. Typical current i_a, and voltage v_a waveforms at the terminals of the actuator are shown in Figure 6.3 for a sinusoidal disturbance f_{ext} at the resonant frequency ω_n of the structure. Due to the capacitive nature of the actuator the current and voltage at the actuator terminals are oscillatory. In particular, the amplifier must be able to sink current.

The components of the amplifier must be capable of withstanding the peak values of current and voltage. The amplifier components should be sized according to the input DC voltage V_{dc} and the peak current required to be driven into the actuator under typical operating conditions.

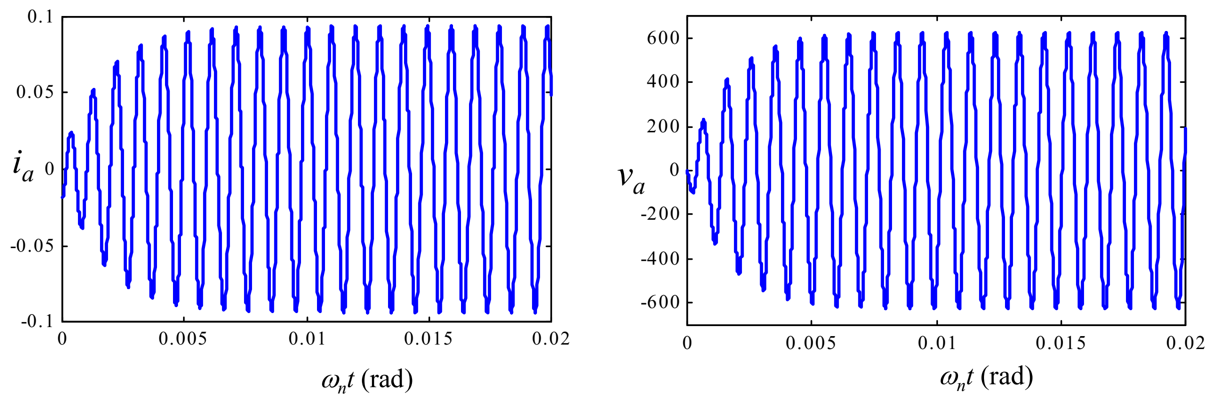

(a) Actuator Current (b) Actuator Voltage

Figure 6.3. Instantaneous current and voltage at actuator terminals

To determine the peak current and voltage at the actuator terminals, a simplified representation of Figure 6.2 as shown in Figure 6.4 is used.

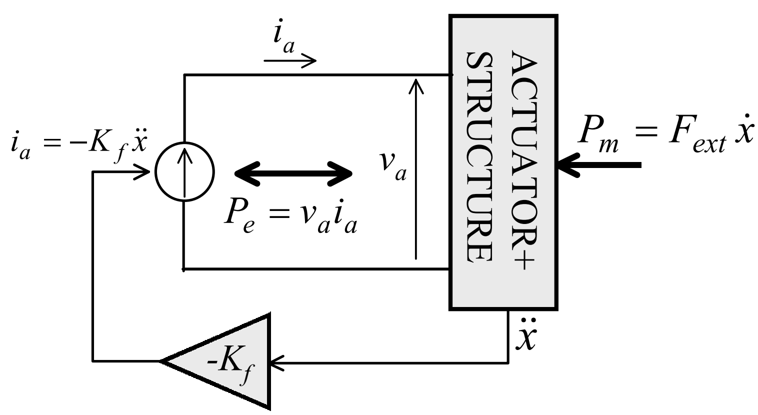

Figure 6.4. Simplified representation of the controlled actuator-structure

The power amplifier is made to appear as an ideal current source/sink to the actuator. Mechanical power is injected into the actuator/structure from the external disturbance and electrical power is injected from the amplifier.

In the following analysis the peak current and voltage into the terminals of the actuator will be determined. The basic idea is to inject a sinusoidal disturbance force into the system, and then determine the voltage and current at the terminals of the actuator as a function of this sinusoidal disturbance force. Sinusoidal steady state analysis is used and the analysis is based on the block diagram in Figure 6.1. From Equation (6.7), the displacement *X*(*s*) of the structure can be obtained as

$$X(s) = \frac{1}{s^2 + 2(\zeta + \zeta_a)\omega_n s + \omega_n^2} \frac{F_{ext}(s)}{M} \tag{6.13}$$

The current is directly proportional to the acceleration of the structure due to the feedback introduced and is given by

$$I_a(s) = -s^2 K_f X(s) = \frac{-s^2 K_f}{s^2 + 2(\zeta + \zeta_a)\omega_n s + \omega_n^2} \frac{F_{ext}(s)}{M} \tag{6.14}$$

It can be seen that the current amplitude reaches its maximum value when the structure is excited at its resonant frequency. This maximum amplitude can be obtained from Equation (6.14) and is

$$I_{a,\max} = \left| I_a(j\omega) \right|\Big|_{\substack{\omega=\omega_n \\ \zeta=0}} = \frac{\omega_n}{\left(\dfrac{k^2}{1-k^2} \dfrac{1}{n d_{33}} \right)} \left| F_{ext}(j\omega) \right| \tag{6.15}$$

The denominator in Equation (6.15) is determined by the material parameters of the actuator. It can be observed, that as the coupling coefficient decreases, the peak current increases. As d_{33} increases, the maximum current increases. Finally, as the number of layers increases, the maximum current increases because the actuator gets bigger.

Through a similar analysis, the maximum voltage across the actuator terminals can be determined. The voltage v_a at the terminals of the actuator is the resultant of the capacitive effect of the actuator and the contribution from the mechanical strain. With reference to Figure 6.1, the voltage is given by

$$V_a(s) = \frac{1}{\varepsilon_{33}}\frac{d}{nlw}\frac{I_a(s)}{s} - \frac{d_{33}}{\varepsilon_{33}} d\left(\frac{Y_{33}}{1-k^2}\right)\left(K_1 X(s) - \frac{d_{33}}{\varepsilon_{33}}\frac{1}{nlw}\frac{I_a(s)}{s}\right)$$
$$= \frac{1}{1-k^2}\frac{1}{C}\frac{I_a(s)}{s} - \frac{d_{33}}{\varepsilon_{33}}\frac{d}{K_2} K_a X(s) \tag{6.16}$$

Substituting for $X(s)$ from Equation (6.13) and for $I_a(s)$ from Equation (6.14), the expression for the voltage $V_a(s)$ in terms of the external disturbance F_{ext} is obtained as follows

$$V_a(s) = \frac{1}{C_{blk}}\frac{I_a(s)}{s} - \frac{d_{33}}{\varepsilon_{33}}\frac{d}{K_2} K_a X(s) = -\left(\frac{sK_f}{C_{blk}} + \frac{d_{33}}{\varepsilon_{33}}\frac{d}{K_2} K_a\right) X(s)$$
$$= \frac{-1}{s^2 + 2(\zeta + \zeta_a)\omega_n s + \omega_n^2}\left(\frac{sK_f}{C_{blk}} + \frac{d_{33}}{\varepsilon_{33}}\frac{d}{K_2} K_a\right)\frac{F_{ext}(s)}{M} \tag{6.17}$$

where,

$$C_{blk} = \varepsilon_{33}\left(\frac{nlw}{d}\right)\left(1-k^2\right) \tag{6.18}$$

, is the equivalent blocked capacitance of the actuator.

Similar to the actuator current, the voltage reaches its maximum amplitude at ω_n. This maximum amplitude determined from Equation (6.17) is given by Equation (6.19).

$$V_{a,\max} = \left|V_a(j\omega)\right|\Big|_{\substack{\omega=\omega_n \\ \zeta=0}} = \sqrt{\frac{1}{K_f^2\omega_n^2} + \frac{1}{\frac{1}{nd_{33}}\frac{k^2}{1-k^2}C_{blk}}}\left|F_{ext}(j\omega)\right| \tag{6.19}$$

Using the expression for the maximum current into the actuator, Equation (6.19) can be further simplified as

$$V_{a,\max} = \left|V_a(j\omega)\right|\Big|_{\substack{\omega=\omega_n \\ \zeta=0}} = \sqrt{\frac{\left|F_{ext}^2(j\omega)\right|}{K_f^2\omega_n^2} + \frac{I_{a,\max}^2}{\omega_n^2 C_{blk}^2}} \tag{6.20}$$

It can be seen from Equation (6.20) that the maximum voltage is determined as a sum of the capacitive voltage drop and a component contributed by the feedback constant and the external disturbance force.

Due to constraints imposed by material properties, there is a specified maximum allowable voltage across the actuator and the value determined from Equation (6.19) should not exceed this maximum allowable voltage. The amplifier components need to be designed such that this maximum amplitude can be safely supplied to the actuator. Finally, the relationship between the maximum voltage delivered to the actuator and the value of the DC bus voltage V_g supplying the amplifier in Figure 6.2 will affect the topology of the amplifier.

6.4 POWER FLOW ANALYSIS

A detailed analysis of the electromechanical power transfer between the amplifier and actuator structure is presented in this section. Sinusoidal steady state analysis is used as in the previous section using Figure 6.1 to obtain expressions for the real and reactive components of the mechanical power from the external disturbance force and the electrical power from the constant current source. The dependence of the power flow characteristics on the material properties and active damping introduced is described. It is assumed that ζ=0, as in the previous section. It can be easily verified that the average mechanical and electrical powers reach their maximum values when the frequency of the sinusoidal excitation is ω_n. Furthermore, their magnitudes decrease as the amount of the active damping introduced by the control system increases.

Using the expressions for the actuator current and voltage from Equations (6.2) and (6.5), the actuator impedance can be obtained as

$$Z_a(j\omega) = \frac{V_a(j\omega)}{I_a(j\omega)} = \frac{1}{j\omega C_{blk}} - \frac{1}{\omega^2}\frac{d_{33}}{\varepsilon_{33}}\frac{d}{K_2}\frac{K_a}{K_f} \qquad (6.21)$$

It can be seen that the electrical impedance of the actuator consists of a reactive part due to the capacitive nature of the actuator and a negative resistive part. The negative resistive part is a manifestation of the active damping introduced to the acceleration feedback. The effect of this negative real part will be explained in the following analysis of power flow. The apparent electrical power is given by

$$P_e(j\omega) = V_a(j\omega)I_a^*(j\omega) = Z_a(j\omega)I_a(j\omega)I_a^*(j\omega) = |I_a(j\omega)|^2 Z_a(j\omega)$$
$$= \frac{\left(K_f^2\omega^4\right)}{\left(\omega_n^2-\omega^2\right)^2 + 4(\zeta+\zeta_a)^2\omega^2\omega_n^2}\left|\frac{F_{ext}(j\omega)}{M}\right|^2\left(\frac{1}{j\omega C_{blk}} - \frac{1}{\omega^2}\frac{d_{33}}{\varepsilon_{33}}\frac{d}{K_2}\frac{K_a}{K_f}\right) \tag{6.22}$$

To calculate the mechanical power into the system, the velocity of the structure is required. From Equation (6.1), the velocity can be obtained as

$$\dot{X}(s) = \frac{s}{s^2 + 2(\zeta+\zeta_a)\omega_n s + \omega_n^2}\frac{F_{ext}(s)}{M} \tag{6.23}$$

Now the apparent mechanical power is given by

$$P_m(j\omega) = F_{ext}(j\omega)\left(-j\omega X^*(j\omega)\right) = \frac{-j\omega}{\left(\omega_n^2-\omega^2\right) - 2j(\zeta+\zeta_a)\omega\omega_n}\frac{|F_{ext}(j\omega)|^2}{M} \tag{6.24}$$

These power quantities are complex, indicating that there is a real net power flow through the system and a circulating reactive power component between the amplifier and the actuator/structure. To illustrate this point, the instantaneous and average mechanical power fed into the structure by a sinusoidal disturbance force with an amplitude of 1000N is shown in Figure 6.5.

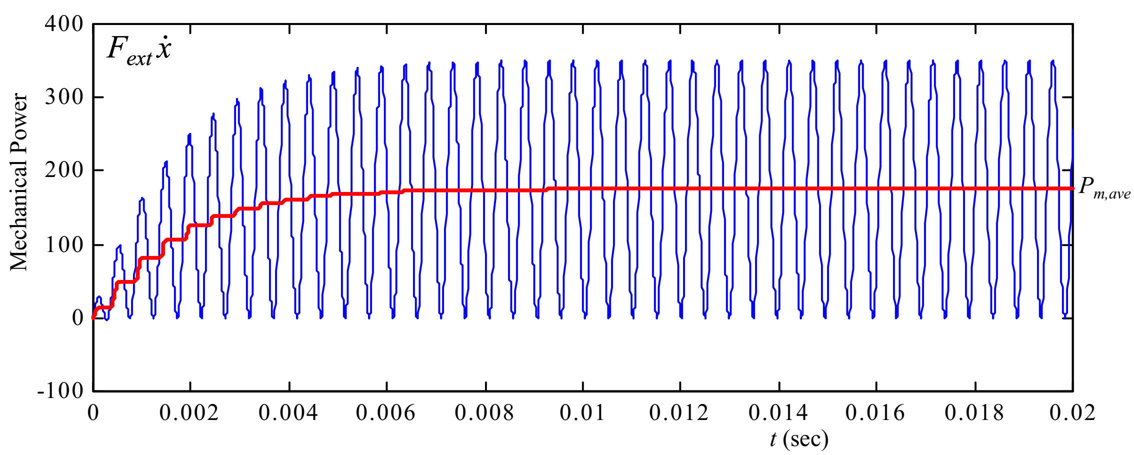

Figure 6.5. Instantaneous and average mechanical power from external disturbance

In steady state, average mechanical power is being injected into the system as shown by Figure 6.5 as long as the system is actively damped ($\zeta_a > 0$).

The corresponding instantaneous and average electrical powers at the terminals of the actuator are shown in Figure 6.6. These graphs show that there is a large oscillating power flow compared to the real power flow. This characteristic is typical of piezoelectric actuators, and must be accounted for in the design of the amplifier. Second, these graphs show a net real power flow from the actuator/structure to the amplifier. This net power flow accounts for the damping introduced by the control loop.

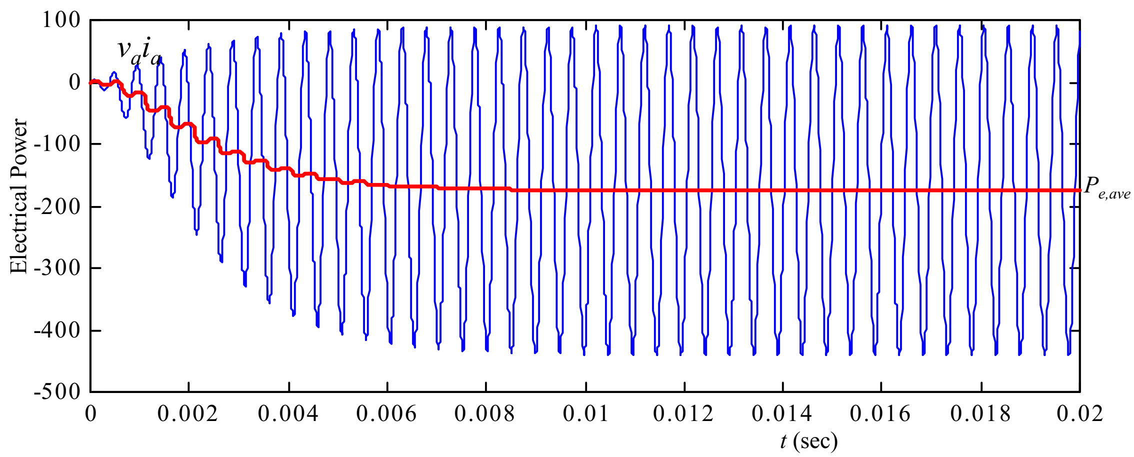

Figure 6.6. Instantaneous and average electrical power at actuator terminals.

The average power is obtained by taking the real part of the apparent power. The average electrical power is

$$
\begin{aligned}
P_{e,ave}(\omega) &= \mathrm{Re}\left[V_a(j\omega)I_a^*(j\omega)\right] = |I_a(j\omega)|^2 \,\mathrm{Re}[Z_a(j\omega)] \\
&= \frac{1}{\left(\omega_n^2-\omega^2\right)^2+4(\zeta+\zeta_a)^2\omega^2\omega_n^2}\left(-\frac{d_{33}}{\varepsilon_{33}}\frac{d}{K_2}K_aK_f\omega^2\right)\left|\frac{F_{ext}(j\omega)}{M}\right|^2 \\
&= \frac{1}{\left(\omega_n^2-\omega^2\right)^2+4(\zeta+\zeta_a)^2\omega^2\omega_n^2}\left(-\frac{d_{33}}{\varepsilon_{33}}\frac{1}{nlw}\frac{1}{K_1}K_aK_f\omega^2\right)\left|\frac{F_{ext}(j\omega)}{M}\right|^2 \\
&= \frac{-2\zeta_a\omega_n\omega^2}{\left(\omega_n^2-\omega^2\right)^2+4(\zeta+\zeta_a)^2\omega^2\omega_n^2}\frac{|F_{ext}(j\omega)|^2}{M}
\end{aligned}
\tag{6.25}
$$

where Equation (6.8) has been used. The average mechanical power is given by

$$P_{m,ave}(\omega) = \mathrm{Re}\left[F_{ext}(j\omega)\left(-j\omega X^*(j\omega)\right)\right] = \frac{2(\zeta+\zeta_a)\omega_n\omega^2}{\left(\omega_n^2-\omega^2\right)^2+4(\zeta+\zeta_a)^2\omega^2\omega_n^2}\frac{\left|F_{ext}(j\omega)\right|^2}{M} \tag{6.26}$$

$$= \frac{2\zeta\omega_n\omega^2}{\left(\omega_n^2-\omega^2\right)^2+4(\zeta+\zeta_a)^2\omega^2\omega_n^2}\frac{\left|F_{ext}(j\omega)\right|^2}{M}$$

$$+ \frac{2\zeta_a\omega_n\omega^2}{\left(\omega_n^2-\omega^2\right)^2+4(\zeta+\zeta_a)^2\omega^2\omega_n^2}\frac{\left|F_{ext}(j\omega)\right|^2}{M}$$

It can also be seen from Equations (6.25) and (6.26) that the average electrical power at the actuator terminals is the portion of the total average input power from the external disturbance that is consumed by the active damping ζ_a introduced by the controlled actuator. The rest of the mechanical power is dissipated in the damping of the structure. This observation is supported by Figures 6.5 and 6.6 (ζ=0). This means that there is an average flow of power from the actuator-structure to the electrical source. This result is similar to the result obtained in [33] which shows that active damping manifests itself in enabling the actuator absorb the injected mechanical energy and funnel it to the electrical source. This electrical power is absorbed by the ideal current amplifier in this model.

It can be seen from Equation (6.12) that the acceleration feedback constant K_f depends on the active damping ratio ζ_a, the electromechanical coupling coefficient k^2 and the physical dimensions of the actuator according to

$$K_f = 2\zeta_a\omega_n M\left(nd_{33}\frac{1-k^2}{k^2}\right) \tag{6.27}$$

Since the active damping ratio is related to the real power flow, it is not surprising that the real power flow depends on the acceleration feedback constant. Figure 6.7 shows the real electrical power as a function of frequency for a range of values of K_f. The damping ζ of the uncontrolled structure is assumed to be zero in Figure 6.7.

It can be seen that the real electrical power reaches its maximum value at the resonant frequency ω_n for all values of K_f as mentioned above. As K_f and hence ζ_a

decreases, the profile of the real power becomes more concentrated around ω_n approaching an impulse for $K_f = \zeta_a = 0$.

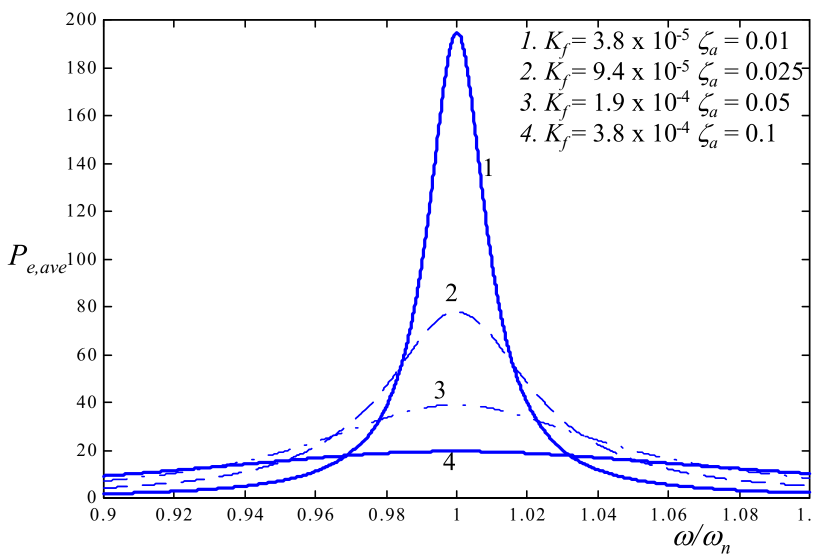

Figure 6.7. Variation of real power with acceleration feedback constant

It is not surprising that the feedback gain affects the real power flow primarily in the frequency band around the natural frequency, because that is where the control action is concentrated. From Equations (6.25) and (6.3), the maximum value of the real electrical power for a given value of K_f can be expressed as

$$\max_{\omega,\zeta}\left[P_{e,ave}(\omega)\right] = P_{e,ave}(\omega)\Big|_{\omega=\omega_n,\zeta=0} = \frac{-1}{2\zeta_a\omega_n}\frac{\left|F_{ext}(j\omega)\right|^2}{M} = -\frac{I_{\max}\left|F_{ext}\right|}{K_f} \tag{6.28}$$

Hence, the maximum real electrical power decreases with increase in the feedback constant and hence the active damping introduced as seen in Figure 6.7.

The electromechanical coupling coefficient of the actuator affects the active damping and the resonant frequency of the structure as can be seen from Equations (6.2), (6.7) and (6.11). The effect of the coupling coefficient on the feedback constant for varying values of active damping can also be determined from Equation (6.27). It can be seen that the acceleration feedback constant K_f required to achieve a given value of active damping ratio ζ_a decreases as the coupling coefficient increases.

Hence, for the given external excitation the average power that the electrical source is required to absorb so as to achieve a reference active damping ratio decreases as the coupling coefficient decreases. This is illustrated in Figure 6.8, which shows the average electrical power absorbed by the current amplifier at the resonant frequency of the structure. The negative values of average power in Figure 6.8 indicate that the power is flowing back through the current amplifier back to the electrical source. It can be seen that as the coupling coefficient increases, there is a decrease in the real power flow back into the amplifier.

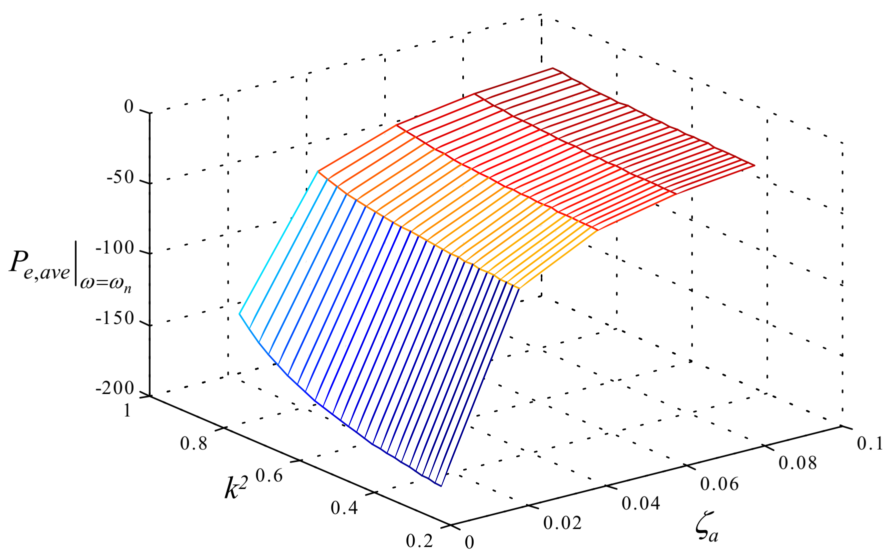

Figure 6.8. Average electrical power at the resonant frequency as a function of k^2 and ζ_a

The complex part of the apparent power implies that there is a considerable amount of reactive power circulates between the actuator and the electrical source. This circulating power can be observed from Figure 6.6. This reactive power results in the current and voltage at the actuator terminals to be oscillatory as shown in Figure 6.2. Since these oscillating currents and voltages are considerably larger that the real power flow, it is necessary to design the amplifier to account for these components. The reactive component of the electrical power is given by

$$P_{e,reac}(\omega) = \mathrm{Im}\left[V(j\omega)I^*(j\omega)\right] = \left|I_a(j\omega)\right|^2 \mathrm{Im}\left[Z_a(j\omega)\right] = -\frac{\left|I_a(j\omega)\right|^2}{\omega C_{blk}}$$
$$= \left[\frac{-\omega^3 K_f^2 / C_{blk}}{\left(\omega_n^2 - \omega^2\right)^2 + 4(\zeta + \zeta_a)^2 \omega^2 \omega_n^2}\right] \left|\frac{F_{ext}(j\omega)}{M}\right|^2 \tag{6.29}$$

The reactive components of the mechanical power is given by

$$P_{m,reac}(\omega) = \mathrm{Im}\left[F_{ext}(j\omega)\left(-j\omega X^*(j\omega)\right)\right]$$
$$= \left[\frac{-\omega\left(\omega_n^2 - \omega^2\right)}{\left(\omega_n^2 - \omega^2\right)^2 + 4(\zeta + \zeta_a)^2 \omega^2 \omega_n^2}\right] \frac{\left|F_{ext}(j\omega)\right|^2}{M} \tag{6.30}$$

It can be seen from Equation (6.30) that when the disturbance frequency is the same as the resonant frequency ω_n, the reactive component in the mechanical power, as expected, becomes zero. The reactive component of the electrical power, however, reaches its maximum at the resonant frequency according to Equation (6.28). Using the expression for the maximum actuator current given by Equation (6.3) the peak reactive power can be obtained as

$$P_{e,reac}(j\omega)\Big|_{\zeta=0,\omega=\omega_n} == -\frac{I_{\max}^2}{\omega_n C_{blk}} = \frac{-\omega_n / C_{blk}}{\left(\frac{1}{d_{33}} \frac{k^2}{1-k^2}\right)^2} \left|F_{ext}(j\omega)\right|^2 \tag{6.31}$$

The peak reactive power is independent of the active damping introduced and is determined by the material constants of the actuator. Figure 6.9 shows the reactive electrical power as a function of the real electrical power over a frequency range $0.1\omega_n$ to $10\omega_n$ for different values of K_f. It can be seen that the peak values of the real and reactive powers increase with decreasing ζ_a as can be expected from Equations (6.25) and (6.26). The amplifier must be designed such that it can handle the real power and capacitive reactive power under worst case operating conditions. Worst case occurs when the actuator is driven at the mechanical resonant frequency where the real and reactive power at the actuator terminals reach their peak operating values.

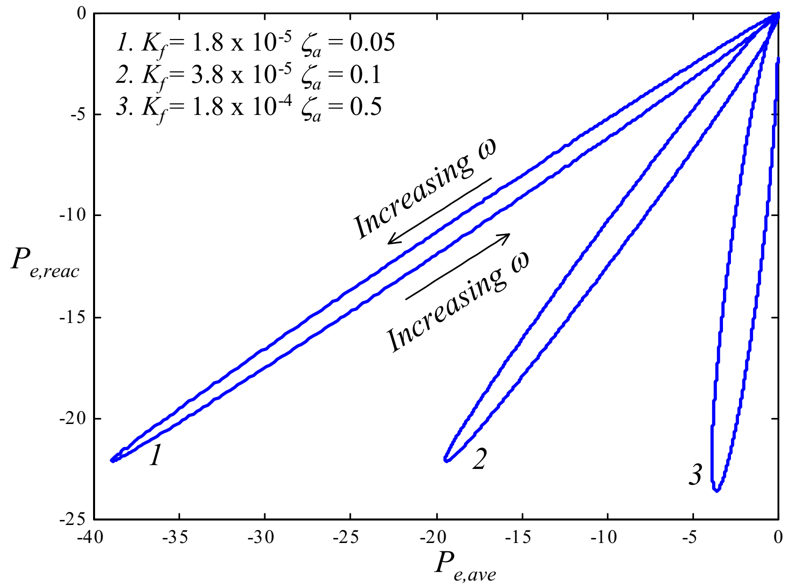

Figure 6.9. Reactive power vs. real power for different ζ_a

Figure 6.10 shows the reactive power at the actuator terminals at the resonant frequency as a function of ζ_a and the coupling coefficient k^2. As expected from Equation (6.30), the reactive power does not vary with the damping ratio but decreases with increasing k^2 since a higher value of the coupling coefficient results in a greater energy conversion efficiency.

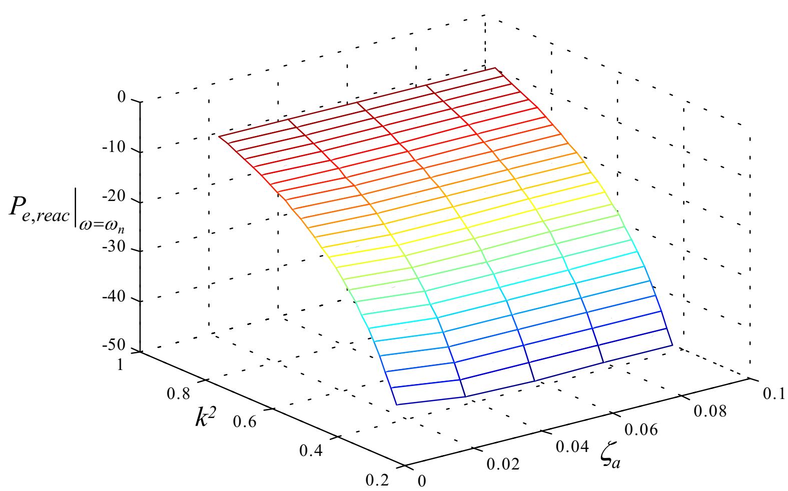

Figure 6.10. Reactive electrical power at the resonant frequency as a function of k^2 and ζ_a

6.5 SUMMARY

In this chapter, some of the factors that influence the design of amplifiers for piezoelectric actuators have been investigated. It was shown that controlling the current through the actuator to be proportional to the acceleration can actively damp the mechanical structure. As a result of this control law, the actuator absorbs the mechanical energy injected into the structure from the external disturbance force and directs it to the electrical source. In addition, due to the capacitive nature of the actuator, there is a considerable amount of reactive energy that needs to be circulated between the actuator and the electrical source. The drive amplifier that controls the actuator current in response to the acceleration feedback needs to be able to accommodate the circulating reactive power and the net flow of average power back from the actuator. A detailed analysis of the electromechanical transfer of power between the amplifier and the actuator is presented and expressions for the peak voltage and current that the amplifier has to support for reliable implementation of the control law are derived. These estimates are critical to the design of the amplifier can be incorporated into an optimization design methodology in a straightforward manner.

PART III

SUBSYSTEM INTERACTION AND STABILITY ANALYSIS

7 MULTIVARIABLE IMPEDANCE RATIO CRITERION

7.1 INTRODUCTION

The baseline power distribution system shown in Figure 2.1 consists of several complex systems that interact with each other. One of critical operational requirements is the stability and robustness of the power distribution system. Hence, in addition to ensuring the stability of individual subsystems, it is necessary to guarantee minimal interaction between interconnected subsystems and avoid unstable operation due to the integration of subsystems. The remainder of the dissertation is devoted to the study of techniques to analyze the stability and interaction between interconnected subsystems.

In the optimization formulations presented in Chapter 3, the classical Middlebrook impedance ratio criterion was used to ensure stability of interconnected subsystems by requiring that the terminal impedances of the individual subsystems at the interconnection be sufficiently separated. However, the impedance ratio criterion, is applicable only to a SISO case and hence cannot be directly applied to study interaction in three phase systems because of their multivariable nature. In this chapter, the impedance ratio criterion is extended to a multivariable setting to make it applicable to three phase and single-phase AC interfaces. A multivariable impedance ratio criterion, defined in terms of the singular values of the terminal impedance matrices at the interconnection is proposed.

Studies of input filter interaction in three phase rectifiers were performed in [43,44], but the results presented therein were not applied to three phase AC-DC converters in general. The design of input filters for power factor correction circuits was introduced in [45]. The factors affecting the choice of the filter topology for power factor correction circuits were outlined. In [46], the three-phase converter was treated as a multivariable system and criteria for the stability of the interconnected filter-converter system were derived based on the eigenvalue loci and singular values of the relevant transfer function matrices. However, the analysis presented in [46] did not clearly identify the effects of the inclusion of the input filter on the performance indices of the system. The analysis presented here is general but is described using the example of a three-phase boost rectifier represented by its average model in rotating *dq* coordinates [47].

The organization of the chapter is as follows: The Middlebrook Impedance Ratio criterion is described in section 7.2. In section 7.3, the basic control objectives of a generic PFC converter are presented. A filter topology suitable for PFC converters as proposed in [45] is chosen as an example for the analysis. The effects of the filter components on the existence and variation of the operating conditions of the converter are detailed. In section 7.4, a three phase boost rectifier with a conventional two-channel controller is used as an example to study the effect of the input filter on the performance and stability of the rectifier system. Expressions for the loop gain, output impedance and audio-susceptibility are derived. Section 7.5 introduces the dq-model of a balanced three phase input filter. The effect of the input filter on the performance indices of the rectifier identified in section 7.4 is determined. The traditional minor loop gain, "Ratio of the output impedance of the filter to the input impedance of the converter" is introduced. A multivariable criterion for the stability of the interconnected system is derived. The stability criterion is then reduced to a sufficient condition based on the singular values of the impedance matrices in section 7.6. Simplifying approximations that enable the system designer to draw on physical insights to relate to the singular values are then made. Simulation results are shown to illustrate the results derived from the analysis.

7.2 MIDDLEBROOK IMPEDANCE RATIO CRITERION

A generic subsystem interface formed by connecting two electrical subsystems in the aircraft power distribution system is shown in Figure 7.1. Each subsystem is represented by a standard two-port model as shown in Figure 7.1.

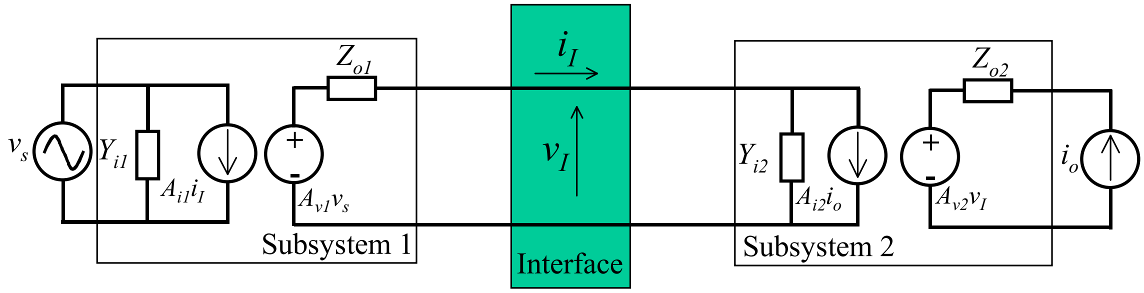

Figure 7.1. Generic Subsystem Interface

The current i_I, and voltage v_I, at the interface are given by

$$\begin{aligned} i_I &= A_{i2}i_o + Y_{i2}v_I \\ v_I &= A_{v1}v_s - Z_{o1}i_I \end{aligned} \tag{7.1}$$

From Equation (7.1), it can be seen that the interconnection results in a feedback loop as shown in Figure 7.2.

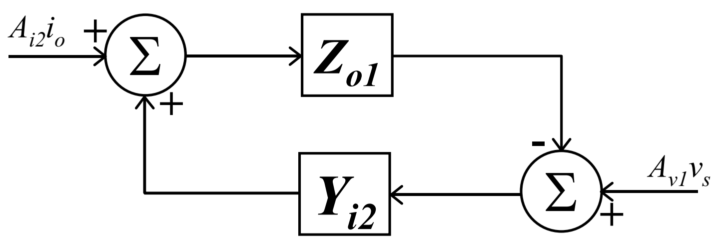

Figure 7.2. Feedback loop at the interface due to interconnection of subsystems 1 and 2

The stability of the interconnected system depends on the stability of the feedback loop. The sufficient condition for the stability of the feedback loop and hence of the interconnected system is given by the small gain theorem. According to the small gain theorem, the feedback loop is stable if the loop gain is less that unity as given below:

$$\left\|Z_{o1}(j\omega)\right\| \cdot \left\|Y_{i2}(j\omega)\right\| << 1 \tag{7.2}$$

This expression can be rewritten as

$$\left\|Z_{o1}(j\omega)\right\| << \frac{1}{\left\|Y_{i2}(j\omega)\right\|} = \left\|Z_{i2}(j\omega)\right\| \tag{7.3}$$

This simple expression says that the magnitude of the output impedance of subsystem 1 (filter) must everywhere be less than the input impedance of subsystem 2 (converter). Equation (7.3) is traditionally known as the Impedance Ratio Criterion.

7.3 Input Filter Interaction in Three-Phase AC-DC Converters

AC-DC converters both three phase and single phase, are basically posed with two control objectives: (1) tight regulation of output DC voltage and (2) regulation of input power factor to unity. The power drawn by the converter from the AC source is, hence, purely real and is equal to the power required by the load on the DC side. The schematic of a three phase AC-DC converter supplied from an AC source through an input filter is shown in Figure 7.3. v_b and v_c, not shown in Figure 7.3, represent the voltages of phase b and c at the converter input.

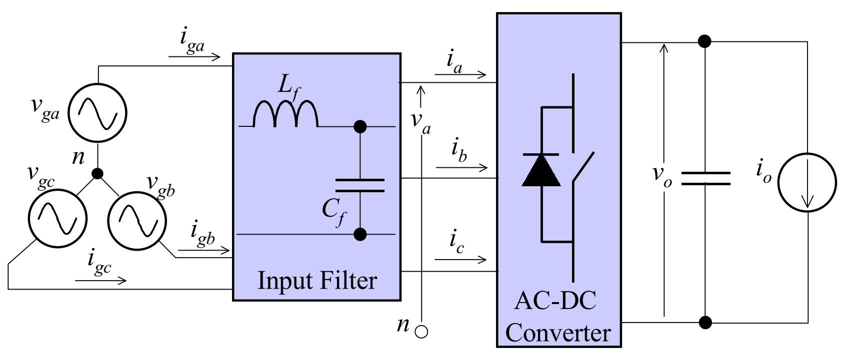

Figure 7.3. Schematic of three-phase AC-DC Converter with input filter

In the absence of an input filter, the voltage v_{ga}=v_a and the current i_{ga}=i_a. With the power factor regulated to unity, the current i_{ga} and the voltage v_{ga} are in phase. The phasor diagram showing the voltages and currents at sinusoidal steady state are shown in Figure 7.4a. With the inclusion of the input filter, if the input current is required to be in phase with the voltage, as in Figure 7.4b, the converter must be forced to draw a current that is not in phase with the voltage at its input.

Thus, some reactive power has to be circulated between the converter and the input filter to achieve unity power factor at the source. Figure 7.5 shows a block diagram of a three phase rectifier fed from an AC source through an input filter.

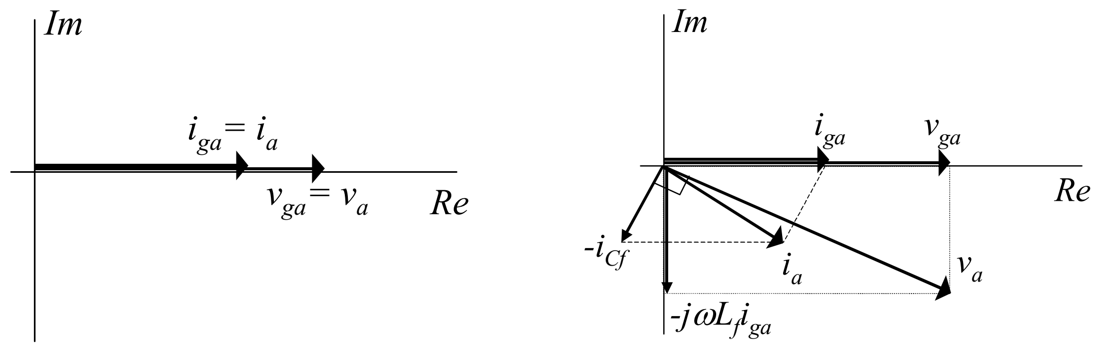

(a) Without Input Filter (b) With Input Filter

Figure 7.4. Phasor Diagram of phase current and voltage with and without input filter

The rectifier, input filter and the AC source are represented by their corresponding *dq* models.

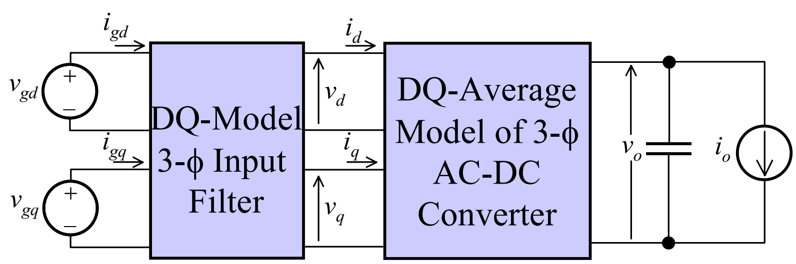

Figure 7.5. DQ-Model of a three phase rectifier fed from an AC source

The real and reactive powers supplied by the source are given by:

$$P = \left(\frac{1}{2}\right)\left(v_{gd}i_{gd} + v_{gq}i_{gq}\right) \tag{7.4}$$

$$Q = \left(\frac{1}{2}\right)\left(v_{gq}i_{gd} - v_{gd}i_{gq}\right)$$

Regulating the power factor to unity at the input requires driving the reactive power Q to zero. This results in the following relationship between the input voltages and currents:

$$\frac{v_{gd}}{i_{gd}} = \frac{v_{gq}}{i_{gq}} \tag{7.5}$$

If the d-axis is synchronized with the zero crossing of the phase a voltage, then $v_{gq}=0$ thus resulting in $i_{gq}=0$ for zero reactive power. The rectifier is usually controlled by a two channel compensator, one channel for output voltage regulation and the other for regulating i_q to I_{qref} to achieve unity power factor. In the absence of an input filter, $v_{gd,q}=v_{d,q}$ and $i_{gd,q}=i_{d,q}$. Hence, regulating i_q to 0 will ensure unity power factor at the input.

However, as mentioned before, with the inclusion of the input filter, it is necessary to circulate some reactive power between the filter and the converter to achieve unity power factor at the input. This translates to regulating i_q to a value different from zero, dependent on the magnitude of the real power supplied to the load, the input voltage and the component values of the input filter. However, the circulating reactive power between the converter and the input filter may result in larger currents to flow through the switches of the converter if the filter components are not appropriately sized. In addition, the inclusion of the input filter appreciably changes the operating point of the rectifier.

7.3.1 Existence and Stability of Equilibrium Solutions

The input filter schematic shown in Figure 7.6 is used as an example for the interaction analysis to be presented in the following. This topology was chosen according to the directions presented in [45] for PFC circuits.

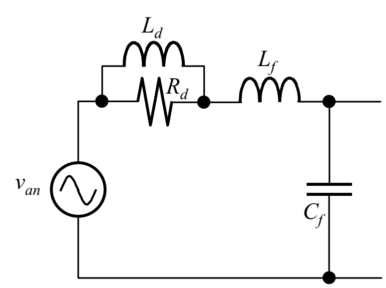

Figure 7.6. Schematic of input filter used in the analysis

Since the dc output voltage of the rectifier is tightly regulated, for a given load, the real power supplied by the rectifier and hence, drawn at the output of the filter (assuming a lossless converter) is constant. If i_q is regulated such that $i_{gq}=0$, the real power P is then given by the equation,

$$P = \frac{1}{2}\left(V_{gd} I_{gd} - I_{gd}^2 R_d \frac{(\omega/\omega_d)^2}{1+(\omega/\omega_d)^2} \right) \tag{7.6}$$

where, $\omega_d = \dfrac{R_d}{L_d}$

From Equation (7.6), it can be seen that real equilibrium solutions exist for the interconnected system if and only if the following condition is satisfied,

$$\frac{V_{gd}^2}{8R_d} > P \frac{(\omega/\omega_d)^2}{1+(\omega/\omega_d)^2} \tag{7.7}$$

Uppercase letters in Equations (7.6) and (7.7) represent the operating point values of the corresponding variables. The operating point values for the input voltages and currents of the converter are given in Equation (7.8).

$$\begin{aligned} V_d &= V_{gd} - I_{gd} R_d \frac{(\omega/\omega_d)^2}{1+(\omega/\omega_d)^2}, \\ V_q &= -\omega L_f I_{gd} - I_{gd} R_d \frac{(\omega/\omega_d)}{1+(\omega/\omega_d)^2}, \\ I_d &= I_{gd} + \omega C_f V_q, I_q = -\omega C_f V_d \end{aligned} \tag{7.8}$$

Figures 7.7 and 7.8 show the effects of changing R_d and C_f on the q-axis input current I_q to the rectifier, power dissipated in the filter, reactive power and the input current drawn by the rectifier. The control design for the rectifier is usually done at a single operating point given by $V_d=V_{gd}$, $V_q=V_{gq}=0$, $I_d=2P/V_d$, $I_q=0$. The filter components must hence be chosen such that the variation in the operating point after the inclusion of the input filter is not appreciable.

It is obvious from Equation (7.8) that C_f does not affect the power loss in the resistor. Increasing R_d reduces the power loss in the filter, at the cost of reduction in damping. To achieve the same damping ratios with a higher R_d requires a higher L_d and hence a bigger filter.

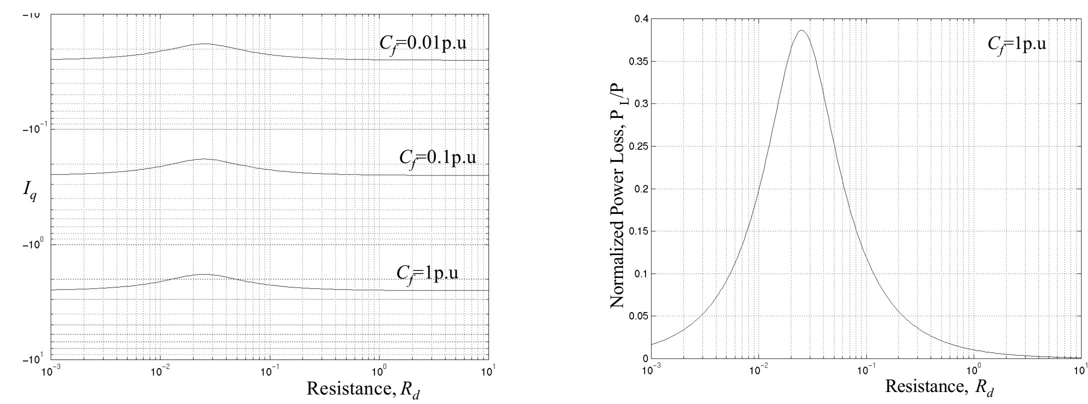

(a) (b)

Figure 7.7. (a) Variation of I_q as a function of R_d for different values of C_f.
(b) Variation of power loss in filter as a function of R_d.

The variation of the resonant frequency, bandwidth and the damping ratios of the filter as a function of the component values are well known and hence, are not included here. A comparison of different filter topologies for PFC circuits is presented in [45].

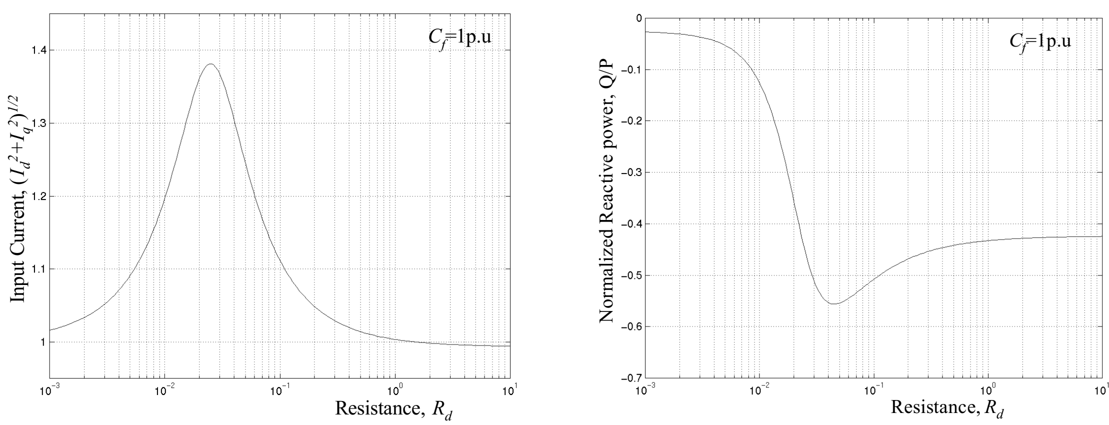

(a) (b)

Figure 7.8. (a) Variation of $(I_d^2+I_q^2)^{1/2}$ as a function of R_d.
(b) Variation of reactive power as a function of R_d.

7.4 Three Phase Boost Rectifier

The three phase boost rectifier is chosen as an example to illustrate the variation of loop gain, output impedance and stability of the system due to the interaction with the input filter. The average model of the three phase boost rectifier in rotating dq-coordinates [47] is given by Equation (7.9).

$$
\begin{aligned}
L\frac{di_d}{dt} &= v_d - d_d^{'} v_o \\
L\frac{di_q}{dt} &= v_q - d_q^{'} v_o \\
C\frac{dv_o}{dt} &= \left(\frac{1}{2}\right)\left(d_d^{'} i_d + d_q^{'} i_q\right) - i_o
\end{aligned}
\tag{7.9}
$$

If the duty cycles d_d and d_q are modified as follows,

$$
d_d = d_d^{'} + \frac{\omega L i_q}{v_o}, d_q = d_q^{'} - \frac{\omega L i_d}{v_o}
\tag{7.10}
$$

the state equations reduce to,

$$
\begin{aligned}
L\frac{di_d}{dt} &= v_d - d_d^{'} v_o \\
L\frac{di_q}{dt} &= v_q - d_q^{'} v_o \\
C\frac{dv_o}{dt} &= \left(\frac{1}{2}\right)\left(d_d^{'} i_d + d_q^{'} i_q\right) - i_o
\end{aligned}
\tag{7.11}
$$

For notational simplicity, the primes for the modified duty cycles are dropped and they are used as the original duty cycles. Linearizing the system of differential equations around an operating point, we get

$$
\frac{d}{dt}\begin{bmatrix} \hat{i}_d \\ \hat{i}_q \\ \hat{v}_o \end{bmatrix} = \begin{bmatrix} 0 & 0 & -\frac{D_d}{L} \\ 0 & 0 & -\frac{D_q}{L} \\ \frac{D_d}{2C} & \frac{D_q}{2C} & 0 \end{bmatrix} \begin{bmatrix} \hat{i}_d \\ \hat{i}_q \\ \hat{v}_o \end{bmatrix} + \begin{bmatrix} -\frac{V_o}{L} & 0 \\ 0 & -\frac{V_o}{L} \\ \frac{I_d}{2C} & \frac{I_q}{2C} \end{bmatrix} \begin{bmatrix} \hat{d}_d \\ \hat{d}_q \end{bmatrix} + \begin{bmatrix} \frac{1}{L} & 0 & 0 \\ 0 & \frac{1}{L} & 0 \\ 0 & 0 & -\frac{1}{C} \end{bmatrix} \begin{bmatrix} \hat{v}_d \\ \hat{v}_q \\ \hat{i}_o \end{bmatrix}
\tag{7.12}
$$

The variables D_d, D_q, I_d, I_q and V_o denote the operating point values of corresponding duty cycles, currents and voltage. The transfer function representation of the linearized system of equations given by Equation (7.12) is given below:

$$
\begin{bmatrix} I_d(s) \\ I_q(s) \\ V_o(s) \end{bmatrix} = \begin{bmatrix} G_{idd} & G_{idq} \\ G_{iqd} & G_{iqq} \\ G_{vod} & G_{voq} \end{bmatrix} \begin{bmatrix} D_d(s) \\ D_q(s) \end{bmatrix} + \begin{bmatrix} Y_{dd} & Y_{dq} & A_{id} \\ Y_{qd} & Y_{qq} & A_{iq} \\ A_{vd} & A_{vq} & Z_o \end{bmatrix} \begin{bmatrix} V_d(s) \\ V_q(s) \\ I_o(s) \end{bmatrix}
\tag{7.13}
$$

The boost rectifier is usually controlled by a two channel compensator, one for the regulation of the output voltage v_o and the other for the q-axis input current i_q. A block diagram representation of a controlled three phase boost rectifier system is shown in Figure 7.9.

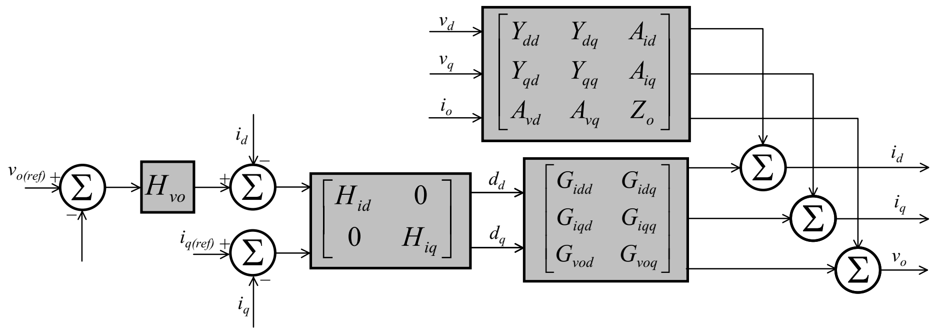

Figure 7.9. Block diagram of the controlled 3-Φ boost rectifier

H_{vo} represents the output voltage controller and H_{id} and H_{iq}, the current controllers. The output variables I_d, I_q and V_o are determined below after making the following definitions:

$$\begin{bmatrix} I_d \\ I_q \end{bmatrix} = I_c, \begin{bmatrix} V_d \\ V_q \end{bmatrix} = V_c, \begin{bmatrix} G_{idd} & G_{idq} \\ G_{iqd} & G_{iqq} \end{bmatrix} = G_{id}, \begin{bmatrix} G_{vod} & G_{voq} \end{bmatrix} = G_{vd},$$
$$\begin{bmatrix} Y_{dd} & Y_{dq} \\ Y_{qd} & Y_{qq} \end{bmatrix} = Y_i, \begin{bmatrix} A_{vd} & A_{vq} \end{bmatrix} = A_v, \begin{bmatrix} A_{id} \\ A_{iq} \end{bmatrix} = A_i, \tag{7.14}$$
$$\begin{bmatrix} H_{id} & 0 \\ 0 & H_{iq} \end{bmatrix} = H_i, H_v = \begin{bmatrix} H_{id} H_{vo} \\ 0 \end{bmatrix}$$

$$\begin{bmatrix} D_d \\ D_q \end{bmatrix} = -\begin{bmatrix} H_i & H_v \end{bmatrix} \begin{bmatrix} I_c \\ V_o \end{bmatrix} \tag{7.15}$$
$$\begin{bmatrix} I_c \\ V_o \end{bmatrix} = -\begin{bmatrix} G_{id} \\ G_{vd} \end{bmatrix} \begin{bmatrix} H_i & H_v \end{bmatrix} \begin{bmatrix} I_c \\ V_o \end{bmatrix} + \begin{bmatrix} Y_i & A_i \\ A_v & Z_o \end{bmatrix} \begin{bmatrix} V_c \\ I_o \end{bmatrix}$$
$$= \begin{bmatrix} I + G_{id} H_i & G_{id} H_v \\ G_{vd} H_i & 1 + G_{vd} H_v \end{bmatrix}^{-1} \begin{bmatrix} Y_i & A_i \\ A_v & Z_o \end{bmatrix} \begin{bmatrix} V_c \\ I_o \end{bmatrix}$$

The reference vector is omitted from the Equation (7.14) because it does not affect the loop gain. The loop gain in Equation (7.15), is not a single transfer function as in the case of a DC-DC converter, but a transfer function matrix given by:

$$T(s) = \begin{bmatrix} G_{id} H_i & G_{id} H_v \\ G_{vd} H_i & G_{vd} H_v \end{bmatrix} \tag{7.16}$$

The diagonal elements of $T(s)$ represent the current and voltage loop gains and the off-diagonal elements, the coupling between the two channels. The characteristic polynomial, the eigenvalues of which determine the stability of the closed loop system is given by:

$$\begin{aligned} \Phi_{CL} &= \det(I + T(s)) \\ &= \det((I + G_{id}H_i)(1 + G_{vd}H_v) - G_{id}H_vG_{vd}H_i) \end{aligned} \tag{7.17}$$

The closed loop output impedance, audiosusceptibility and input admittance determined from Equation (7.15) are given in Equation (7.18). The modifications in the above expressions due to the interaction with the input filter are determined in the next section.

$$\begin{aligned} &\begin{bmatrix} Y_i & A_i \\ A_v & Z_o \end{bmatrix}^{CL} = (I + T(s))^{-1} \begin{bmatrix} Y_i & A_i \\ A_v & Z_o \end{bmatrix} \\ &(I + T(s))^{-1} = \begin{bmatrix} S^{-1}(1 + G_{vd}H_v) & -S^{-1}G_{id}H_v \\ -G_{vd}H_iS^{-1} & \dfrac{(I + G_{vd}H_iS^{-1}G_{id}H_v)}{(1 + G_{vd}H_v)} \end{bmatrix} \\ &S = (I + G_{id}H_i)(1 + G_{vd}H_v) - G_{id}H_vG_{vd}H_i \end{aligned} \tag{7.18}$$

7.5 EFFECT OF INPUT FILTER ON RECTIFIER PERFORMANCE

The circuit schematic of one phase of a typical input filter is shown in Figure 7.6. The corresponding state space representation of one phase is given by Equation (7.19).

$$\begin{aligned} \dot{x} &= A_f x + Bu \\ y &= C_f x \end{aligned} \tag{7.19}$$

The dq model of the input filter derived based on the directions presented in Chapter 3 is shown in Figure 7.10. The corresponding state space representation of the dq model is given by Equation (7.20).

$$\begin{aligned} \begin{bmatrix} \dot{x}_d \\ \dot{x}_q \end{bmatrix} &= \begin{bmatrix} A_f & \omega_s I \\ -\omega_s I & A_f \end{bmatrix} \begin{bmatrix} x_d \\ x_q \end{bmatrix} + \begin{bmatrix} B_f & 0 \\ 0 & B_f \end{bmatrix} \begin{bmatrix} u_d \\ u_q \end{bmatrix} \\ \begin{bmatrix} y_d \\ y_q \end{bmatrix} &= \begin{bmatrix} C_f & 0 \\ 0 & C_f \end{bmatrix} \begin{bmatrix} x_d \\ x_q \end{bmatrix} \end{aligned} \tag{7.20}$$

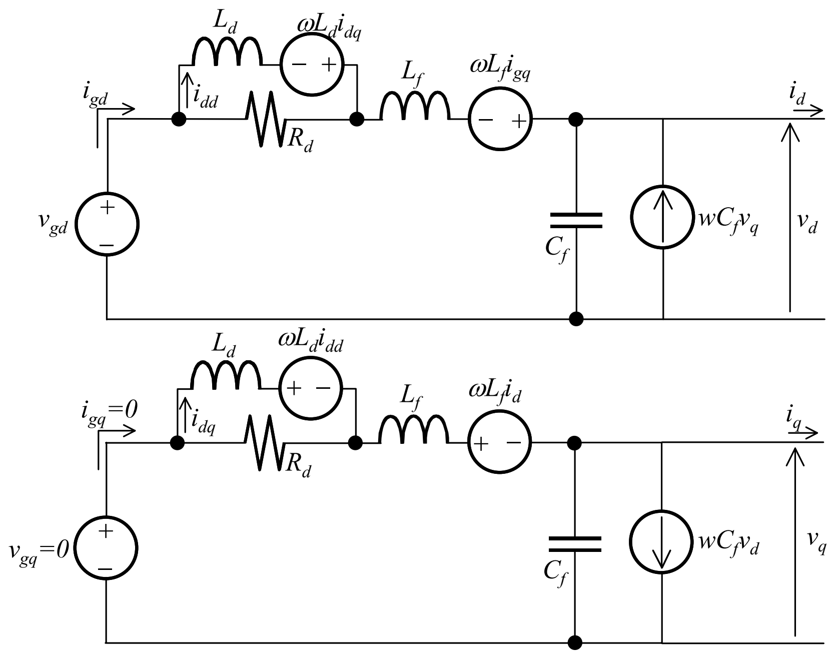

Figure 7.10. *DQ*-Equivalent circuit model of three phase input filter

The transfer function representation of the Equation (7.20) is then,

$$\begin{bmatrix} Y_d(s) \\ Y_q(s) \end{bmatrix} = \begin{bmatrix} M(s) & N(s) \\ -N(s) & M(s) \end{bmatrix} \begin{bmatrix} U_d(s) \\ U_q(s) \end{bmatrix} \tag{7.21}$$

where,

$$\begin{aligned} M(s) &= C_f\left(sI - A_f\right)\left[\left(sI - A_f\right)^2 + \omega_s^2 I\right]^{-1} B_f \\ N(s) &= \omega_s C_f \left[\left(sI - A_f\right)^2 + \omega_s^2 I\right]^{-1} B_f \end{aligned} \tag{7.22}$$

ω_s, the angular frequency of the input supply voltage. Figure 7.11 shows how the input filter affects the input currents and output voltage of the boost rectifier.

Due to the interaction with the input filter, Equation (7.15) gets modified as follows.

$$\begin{bmatrix} I_c \\ V_o \end{bmatrix} = \begin{bmatrix} I + G_{id}H_i + Y_i Z_{of} & G_{id}H_v \\ G_{vd}H_i + A_v Z_{of} & 1 + G_{vd}H_v \end{bmatrix}^{-1} \begin{bmatrix} Y_i H_f & A_i \\ A_v H_f & Z_o \end{bmatrix} \begin{bmatrix} V_g \\ I_o \end{bmatrix} \tag{7.23}$$

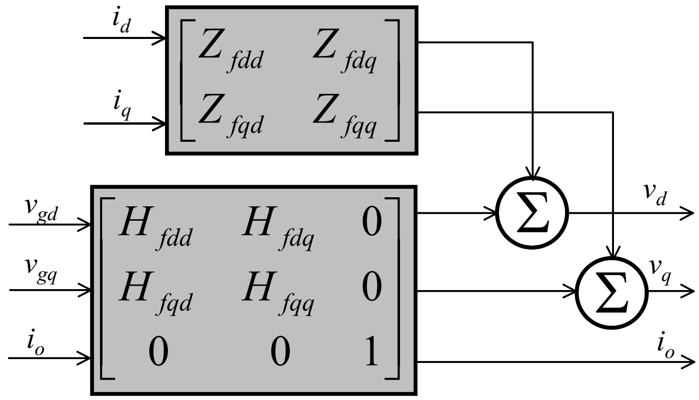

Figure 7.11. Effect of input filter on output variables of the rectifier

The characteristic polynomial is given by Equation (7.24). The last part of Equation (7.24) is obtained from the expression derived in Equation (7.18) for the closed loop input admittance.

$$\begin{aligned}\Phi_{CL(filt)} &= \det\Big(\big(I + G_{id}H_i + Y_i Z_{of}\big)\big(1 + G_{vd}H_v\big)\Big) \\ &\quad - G_{id}H_v\big(G_{vd}H_i + A_v Z_{of}\big) \\ &= \det\big(I + T(s)\big)\times \\ &\quad \det\left(I + \left(\big(I + G_{id}H_i\big)^{-1}Y_i - \frac{G_{id}H_v A_v}{\det\big(I + T(s)\big)}\right)Z_{of}\right) \\ &= \det\big(I + T(s)\big)\det\big(I + Y_i^{CL}Z_{of}\big)\end{aligned} \tag{7.24}$$

The origin of the minor loop gain, "$Y_I^{CL}Z_{of}$" can be clearly seen in Equation (7.24). The stability of the interconnected system is now given by stability of the controller loops and of the minor loop due to the interaction. Thus, the stability of interconnection is determined by the zeros of $\det(I+Y_i^{CL}Z_{of})$. It is obvious that the smaller the "magnitude" of the minor loop gain is compared to unity, lesser is the effect of the interaction due to the input filter on the performance and stability of the converter.

7.6 Sufficient Condition for Stability

According to the multivariable Nyquist criterion [48], the interconnected system is internally stable if the number of counterclockwise encirclements of the origin made by the Nyquist contour of $\det(I+Y_i^{CL}Z_{of})$ is equal to the number of right half plane poles of Y_I^{CL} and Z_{of}. Since Y_I^{CL} and Z_{of} are transfer function matrices, it is quite difficult to relate their individual elements to the characteristic polynomial det($I+Y_i^{CL}Z_{of}$). Hence, the criterion for stability must be simplified so that it lends itself to direct physical insight and can be used efficiently in a design procedure. In the following, a sufficient condition for stability is derived based on the singular values of input admittance Y_I^{CL}, and output impedance Z_{of} matrices. From Figure 7.9 and Equation (7.15) the voltage at the output terminals of the filter can be determined as given by Equation (7.25). Equation (7.25) shows the existence of a feedback loop as shown in Figure 7.62, the only difference in this case being that the elements of the feedback loop are transfer function matrices.

$$\begin{bmatrix} V_d \\ V_q \end{bmatrix} = \left. \left[I + \underbrace{\begin{bmatrix} Z_{fdd} & Z_{fdq} \\ Z_{fqd} & Z_{fqq} \end{bmatrix}}_{Z_{oF}} \overbrace{\begin{bmatrix} Y_{dd}^{CL} & Y_{dq}^{CL} \\ Y_{qd}^{CL} & Y_{qq}^{CL} \end{bmatrix}}^{Y_i^{CL}} \right]^{-1} \underbrace{\begin{bmatrix} H_{fdd} & H_{fdq} \\ H_{fqd} & H_{fqq} \end{bmatrix} \begin{bmatrix} V_{gd} \\ V_{gq} \end{bmatrix}}_{\begin{bmatrix} V_{sd} \\ V_{sq} \end{bmatrix}} \right|_{I_o=0} \tag{7.25}$$

$$\begin{bmatrix} V_d \\ V_q \end{bmatrix} = \left[I + Z_{oF} Y_i^{CL} \right]^{-1} \begin{bmatrix} V_{sd} \\ V_{sq} \end{bmatrix}$$

According to the small gain theorem, a sufficient condition for stability is to ensure that the product of the incremental gains of the systems comprising the feedback loop is less than unity for all ω. The incremental gain of a linear, time invariant, stable system is its maximum singular value. The theory of singular values of a matrix and its application to the study of multivariable systems has been well established [48]. In simple terms, the singular values of a matrix represent its “modulus” or “gain” similar to the modulus of a scalar constant. Hence, the sufficient condition for stability is given by

$$\overline{\sigma}\left(Y_i^{CL}(j\omega)\right)\overline{\sigma}\left(Z_{of}(j\omega)\right) < 1 \tag{7.26}$$

The sufficient condition for stability also turns out to be the condition that ensures minimal interaction between the input filter and the converter as shown below.

$$\left|\det\left(I + Y_i^{CL}(j\omega) Z_{of}(j\omega)\right)\right| \leq \left(1 + \overline{\sigma}\left(Y_i^{CL}(j\omega)\right)\overline{\sigma}\left(Z_{of}(j\omega)\right)\right)^2 \tag{7.27}$$

Hence, satisfying Equation (7.26) not only ensures the stability of the minor loop gain (and hence of the integrated system), but also that its modulus is closer to 1 than to zero so that the characteristic polynomial given by Equation (7.24) is not appreciably different from that given by Equation (7.17).

7.6.1 Simplifying Approximations

In this section, approximate expressions for the singular values of Y_i^{CL} and Z_{of} are derived based on the knowledge of the physical properties of the system. The three phase rectifier, as mentioned before, regulates i_q to a reference value to provide unity power factor at the input. This reference value is determined as a function of the real power P, supplied by the rectifier and the input voltage. It provides a tightly regulated DC output and hence constant power for a given load. Thus, a simplified model of the rectifier that is valid at low frequencies can be represented as shown in Figure 7.12.

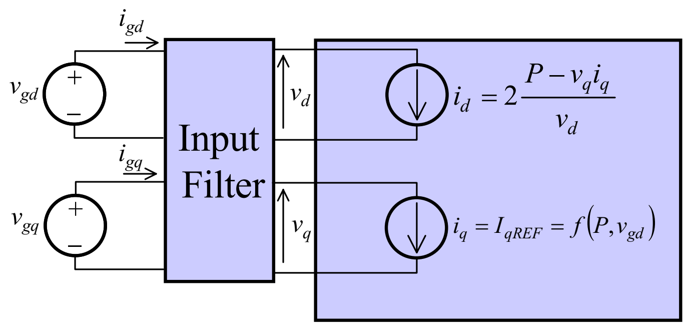

Figure 7.12. Low frequency model of 3-Φ rectifier with input filter

The function f, in Figure 7.12, used to determine I_q is static with no time dependent dynamics. Hence, the input admittance of the rectifier and its singular values according to Figure 7.12 are then given by,

$$Y_i^{CL} \approx Y_i^{DC} = \begin{bmatrix} Y_{dd} & Y_{dq} \\ 0 & 0 \end{bmatrix} = \begin{bmatrix} -2\frac{P - V_q I_q}{V_d^2} & 2\frac{I_q}{V_d} \\ 0 & 0 \end{bmatrix} \tag{7.28}$$

$$\bar{\sigma}\left(Y_i^{CL}\right) \approx \bar{\sigma}\left(Y_i^{DC}\right) = \sqrt{\left|Y_{dd}\right|^2 + \left|Y_{dq}\right|^2}$$

The output impedance of the input filter, from Equation (7.21), is given by,

$$Z_{of} = \begin{bmatrix} M(s) & N(s) \\ -N(s) & M(s) \end{bmatrix} \tag{7.29}$$

$$\begin{aligned}\bar{\sigma}(Z_{of}(j\omega)) &= \sqrt{|M(j\omega)|^2 + |N(j\omega)|^2 + 2\left|\mathrm{Im}\left(M^*(j\omega)N(j\omega)\right)\right|} \\ &\leq |M(j\omega)| + |N(j\omega)|\end{aligned}$$

M(s) and *N(s)* are as defined in Equation (7.21) with the appropriate choice of B_f and C_f matrices. It can be easily shown that the imaginary parts of the eigenvalues of the *dq*-model of the filter are symmetrically displaced from the values for the single phase model by the angular frequency ω_s of the input voltages.

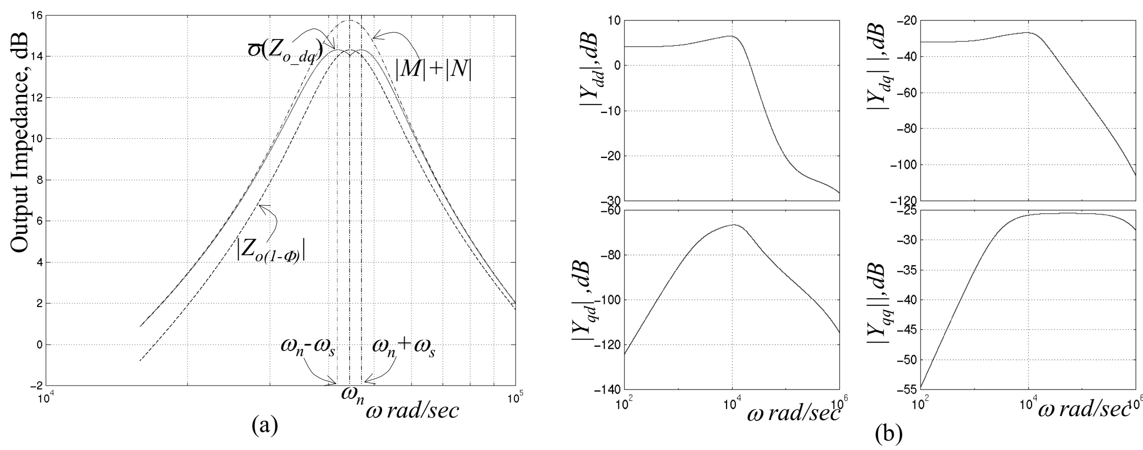

Figure 7.13. (a) Output Impedance of Input Filter (b) Input Admittance of Boost Rectifier

Figure 7.13 shows the input admittance and output impedance transfer functions of the boost rectifier and input filter respectively to illustrate the approximations made in Equations (7.28) and (7.29).

7.6.2 Simulation Results

The interaction between the input filter and the converter is shown in Figure 7.14 for two sets of parameter values for the input filter, one that results in appreciable impedance overlap and hence strong interaction Figure 7.14a) and another with no impedance overlap and minimal interaction (Figure 7.14b). The singular values of the input admittance and output impedance of the rectifier and the filter respectively are plotted as a function of frequency. The voltage loop gain of the rectifier with and without the input filter is also shown in Figure 7.14 to illustrate the effect of the interaction due to the input filter. It can be seen that the voltage loop gain of the rectifier is unaffected by the input filter when the impedance overlap is minimal. On the other hand, a significant impedance overlap results in an appreciable degradation of the voltage loop gain of the rectifier. However, this does not necessarily cause the system to become unstable because the impedance ratio criterion is only a sufficient condition for stability.

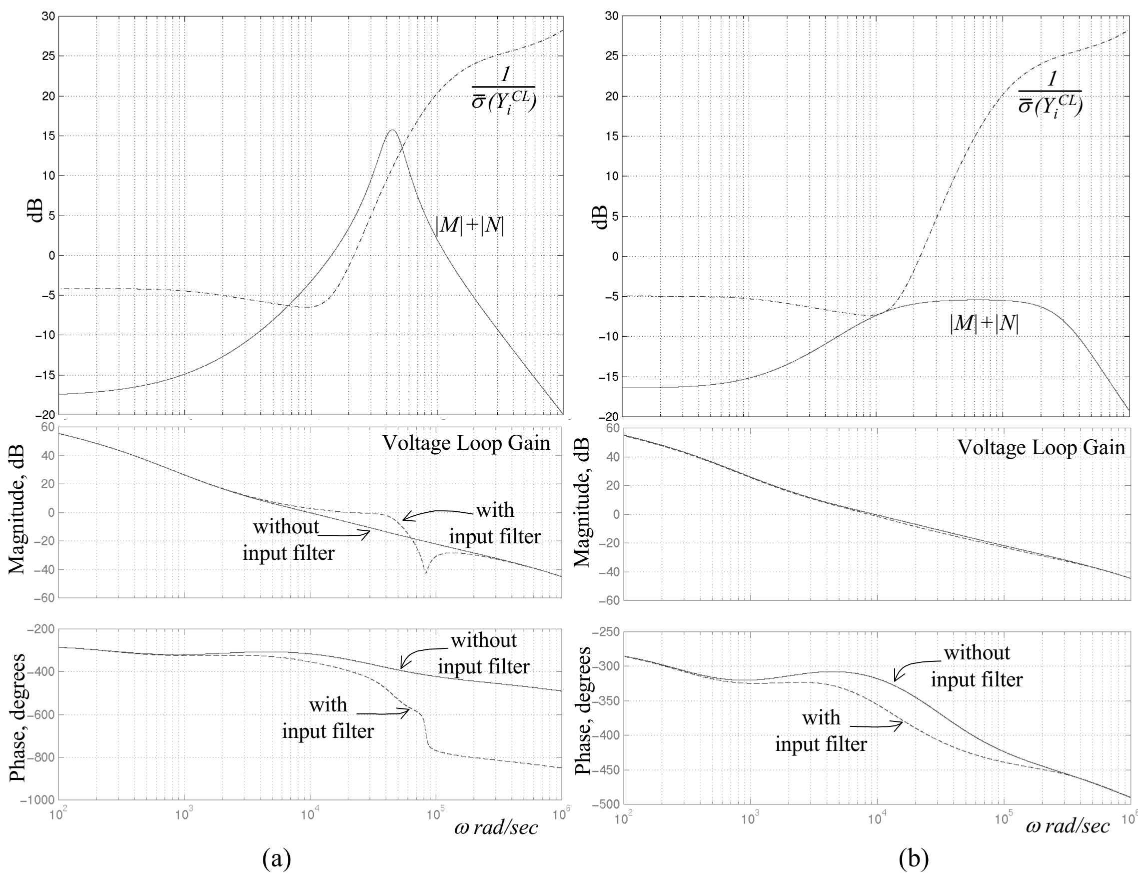

Figure 7.14. Impedance overlap and voltage loop gain of the rectifier system with and without input filter (a) Strong Interaction (b) Minimal interaction

7.7 SUMMARY

The problem of input filter interaction in three phase AC-DC converters was addressed in this chapter. An input filter topology was chosen and its effect on the performance indices of a three phase boost rectifier represented by its *dq*-average model was presented. A multivariable stability criterion based on the "minor loop gain" was determined. The stability of the minor loop gain and hence of the integrated system was guaranteed by ensuring that the product of the singular values of the impedance matrices of the rectifier and the filter was less than unity. The criterion was then reduced to a sufficient condition for stability bases on the singular values of the input admittance and output impedance matrices of the rectifier and the input filter respectively. Simplifying approximations based on the physical properties of the system were made to make the stability criterion more amenable to practical design. Simulation results to illustrate the results of the analysis were presented.

8 STABILITY UNDER BIDIRECTIONAL POWER FLOW

8.1 INTRODUCTION

The impedance ratio criterion used to guarantee minimal interaction and stability of interconnected systems is based on the linearized models of subsystems around a nominal operating point. It guarantees only local stability in a small neighborhood of the equilibrium point. Hence, the behavior of the system when subjected to a large disturbance cannot be predicted using such linear analysis techniques. Methods that accommodate the nonlinear characteristics of the system must then be used to obtain a global understanding of the system behavior. The use of nonlinear methods for the stability and subsystem interaction analysis of interconnected systems is discussed in this chapter.

It was shown in Chapter 6 that the piezoelectric actuator could actively damp the mechanical structure by controlling the actuator current to be proportional to the acceleration of the structure. It was also shown that the actuator, in actively damping the structure, absorbs the mechanical energy fed from the external disturbance force and redirects it back to the electrical source. As a result, there is a net flow of real power back to the DC bus from the actuator in addition to the circulating reactive power due to the capacitive nature of the actuator. It is critical to determine if this regenerative power has any detrimental effects on the stability of the drive amplifier. To this end, the analysis of the stability of an integrated system consisting of a regulated power converter with an input filter under bidirectional power flow in presented in this section. The analysis is simplified in that it is assumed that there is no circulating reactive power at the converter output. It is found that the forward direction of power flow is more critical from a stability point of view. In other words, the flow of power in the reverse direction does not destabilize the system if stability is maintained in the forward direction.

8.2 STABILITY UNDER BIDIRECTIONAL POWER FLOW

A simple nonlinear system consisting of a regulated power converter modeled as a constant power load followed by an input filter is used for the study [50]. Figure 8.1 shows a simplified schematic of a regulated power converter with an input filter.

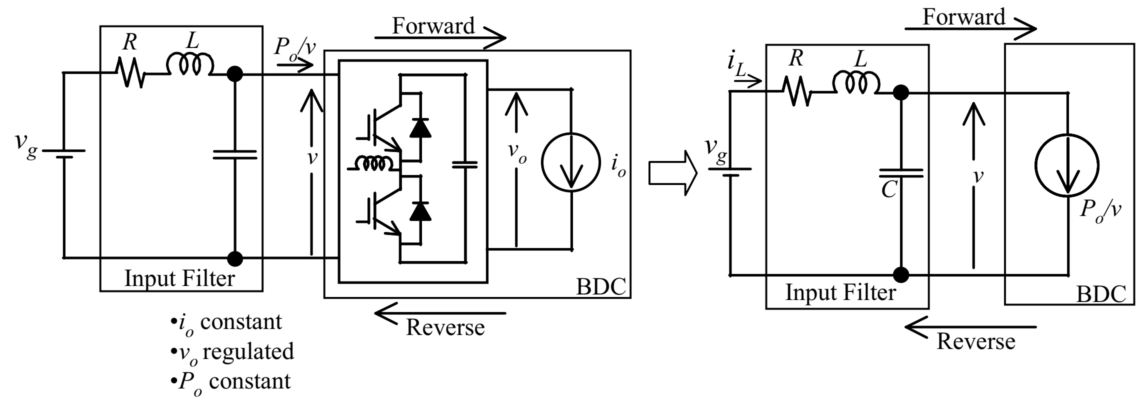

Figure 8.1. Regulated Converter with Input Filter

The stability of this interconnected system under conditions of bidirectional power flow will be investigated in this section. This system consists of a regulated bidirectional power converter connected to a source through an input filter. The output of the converter is connected to an ideal load modeled by a current source. Under constant load conditions, the power delivered to the load is constant because the output voltage of the converter is regulated. The regulated converter thus appears as a constant power load to a system that is connected at its input. The constant power curve of this converter is shown in Figure 8.2 by the solid curve when the power is flowing to the load. When the load is regenerating power, the constant power curve is shown by the dotted line in the fourth quadrant of the graph. The constant power curves in Figure 8.2 show that the system in Figure 8.1 is fundamentally a nonlinear system, and that the converter and load appears as a negative impedance to the source when the power is flowing in the forward direction as shown. When the direction of power flow reverses, the input impedance of the converter subsystem changes sign as can be clearly observed in Figure 8.2.

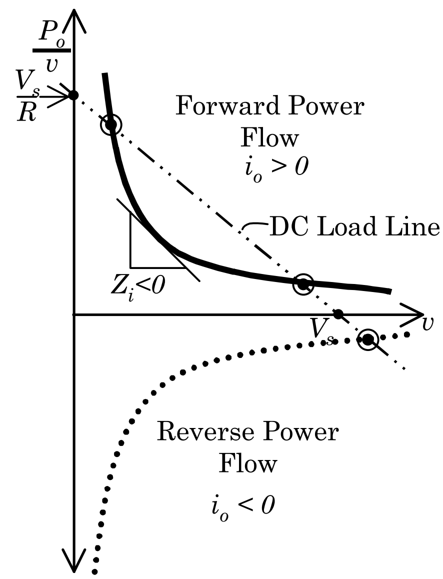

Figure 8.2. Constant Power Characteristics of a Regulated Power Converter

The state equations for the system shown in Figure 8.2 are given below:

$$L\frac{di_L}{dt} = v_g - Ri_L - v \qquad (8.1)$$
$$C\frac{dv}{dt} = i_L - \frac{P_o}{v}$$

The equilibrium solutions for the system are given by:

$$I_{Le} = \frac{P_o}{V_e}$$
$$V_e = \frac{V_g}{2}\left(1 \pm \sqrt{1 - 4R\frac{P_o}{V_g^2}}\right) \qquad (8.2)$$

The equilibrium points for the system are also determined from the points of intersection between the DC load line and the constant power characteristics of the power converter. This is illustrated in Figure 8.2. Equilibrium solutions exist as long as the load line intersects the constant power curve. In the forward direction, the load lines for $R \le V_g^2 / 4P_o$ intersect the constant power curve. Equilibrium points do not exist for $R > V_g^2 / 4P_o$. On the other hand, there exist equilibrium points for all values of R in the reverse direction. This can be inferred from the expressions for the equilibrium solutions in Equation (8.2). Real equilibrium solutions for V_e exist only for $R \le V_g^2 / 4P_o$. However, for reverse power flow when P_o is negative equilibrium solutions exist for all values of R.

The stability of the equilibrium points depends on the parameter values. To make the stability analysis practical meaningful, the constant power characteristic of the regulated power converter is redrawn to have a finite area under it as shown in Figure 8.3 [50,51].

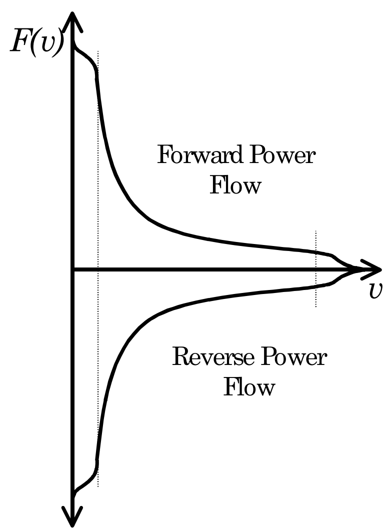

Figure 8.3. Constant Power Characteristics of a Regulated Power Converter

Definition Complete Stability [50]: A system is said to be "completely stable" if there exist finitely many equilibrium solutions and every solution for the system equations approaches an equilibrium solution.

The criterion for complete stability is given below:

Theorem (Brayton and Moser): A dynamic system described by the state equations

$$\begin{aligned} \dot{x} &= -Ax + Bu \\ \dot{y} &= Dx - f(y) \end{aligned} \tag{8.3}$$

with the following conditions,

1. A is symmetric and positive definite
2. $B = -D^T$
3. The Jacobian df/dy is symmetric

and $B^T A^{-1} y + f(y) = Grad\ G(y)$,if,

$$1. \left\| A^{-1}B \right\| < 1 \qquad (8.4)$$
$$2. G(y) \to \infty \text{ as } |y| \to \infty$$

The system is completely stable.

To fit the system in Figure 8.1 within the framework of the theorem given above, the following definitions are made.

$$x := i_L \qquad y := \sqrt{\frac{C}{L}}(v - V_g)$$
$$A := -\frac{R}{L} \quad B = -D = -\frac{1}{\sqrt{LC}} \qquad (8.5)$$
$$f(y) = \frac{1}{\sqrt{LC}} F\left(\sqrt{\frac{L}{C}} + V_g\right)$$

where, $F(v)$ is as shown in Figure 8.3.

Test for Stability:

$$1. \quad \left\| A^{-1}B \right\| < 1 \Rightarrow \sqrt{\frac{L}{C}} < R$$
$$2. \quad G(y) = \frac{1}{2RC} y^2 + \frac{1}{\sqrt{LC}} \int_0^y F\left(\sqrt{\frac{L}{C}}\sigma + V_g\right) \cdot d\sigma \qquad (8.6)$$

If $F(v)$ is as shown in Figure 8.3, $G(y) \to \infty$ as $|y| \to \infty$ and complete stability is ensured if

$$\sqrt{\frac{L}{C}} < R \qquad (8.7)$$

Thus, the stability region can be defined for the forward direction as shown in Figure 8.4. The forward direction of power flow is hence, most critical from the stability standpoint (i.e.) as long as stability is guaranteed in the forward direction, it is preserved in the reverse direction upto the same power level. The reversal of power flow results in the input impedance of the converter system changing sign. The reasons for potential instability due the negative input impedance of the converter thus cease to exist during regeneration.

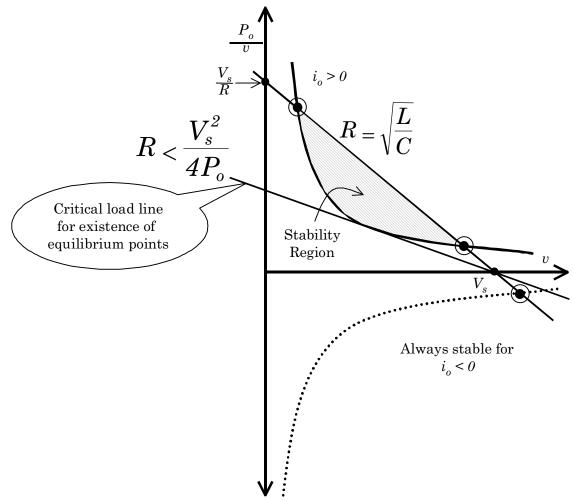

Figure 8.4. Stability of Equilibrium Solutions

This result can be further corroborated by the impedance ratio criterion. Nyquist contours of the loop gain $Z_{o1}Y_{i2}$ are shown in Figure 8.5 as a function of the load current.

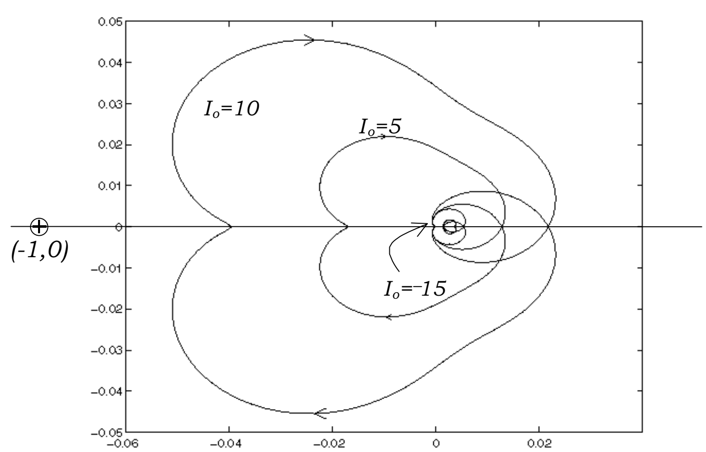

Figure 8.5. Stability of Interconnected System under reversal of power flow

Z_{o1} and Y_{i2} represent the output impedance and the input admittance respectively of the input filter and power converter respectively. It can be seen that the Nyquist plots move further away from the (*-1,0*) as the load current changes sign and hence reverses the power flow. The foregoing analysis thus suggests that the overall system stability is determined by the stability of the system when the power is flowing in the forward direction.

8.3 SUMMARY

A simplified analysis to determine the stability properties of an interconnected system under regenerative power flow conditions is presented. The interconnected system consists of a regulated DC-DC converter, modeled as a constant power load, preceded by an EMI input filter. It is shown that the forward direction of power flow is more critical to the stability of the system than the reverse direction when the load current is flowing back to the source. If this result extends to more complicated models, it suggests a simplification in the design process by reducing the complexity of the stability tests.

9 BIFURCATION METHODS

9.1 INTRODUCTION

The use of nonlinear methods to study the global stability and interaction behavior of interconnected systems is continued in this chapter with the application of bifurcation methods. The term “Bifurcation” is used to indicate a qualitative change in the properties of a system as a function of one or more parameters known as bifurcation parameters. The changes typically are in the number, type and stability of solutions to the dynamic equations that describe system behavior. Typically, a system is said to bifurcate when its equilibrium point loses stability at a given operating condition. These analysis methods are then primarily concerned in the post-bifurcation behavior of the system. That is, they provide information about the characteristics of the system after the equilibrium point loses stability. Linear analysis methods, however, can only predict the loss of stability of the equilibrium point.

In bifurcation problems, it is useful to consider a space comprising the state variables and the bifurcation parameters. Bifurcation points are identified in this space by observing changes in system properties as a function of a chosen set of bifurcation parameters. A physical understanding of the subsystem being analyzed motivates the choice of bifurcation parameter(s).

The use of bifurcation methods for the study of global stability is demonstrated using two examples of interconnected systems. The interaction between a regulated DC-DC buck converter and an EMI input filter is studied first. The buck converter is represented by its average model in order to capture only the system level, low frequency interactions with the input filter. The damping resistance in the input filter is chosen as the bifurcation parameter. The bifurcation behavior of the system is studied as the damping resistance varies. The results are then compared with those obtained from the application of the impedance ratio criterion. The second example deals with the study of interaction at the DC bus of a simplified power distribution represented as a single source-single load system. The source subsystem is a three-phase boost rectifier that feeds the 270V DC bus of the power distribution system. The rectifier is represented by its average model in rotating *dq* coordinates synchronized with the input line voltages. The load subsystem is a regulated DC-DC buck converter with a front-end input filter. The load converter is modeled as a constant power load similar to that studied in [50]. The voltage controller gain of the three phase boost rectifier is chosen as the bifurcation parameter as it is directly related to the voltage regulation bandwidth of the rectifier. The dependence of the bifurcation behavior of the system as a function of the total power at the DC bus is discussed. The applicability of these methods to a practical design procedure is explored.

9.2 INPUT FILTER INTERACTION

The circuit schematic of a regulated DC-DC buck converter with an input filter is shown in Figure 9.1 [53].

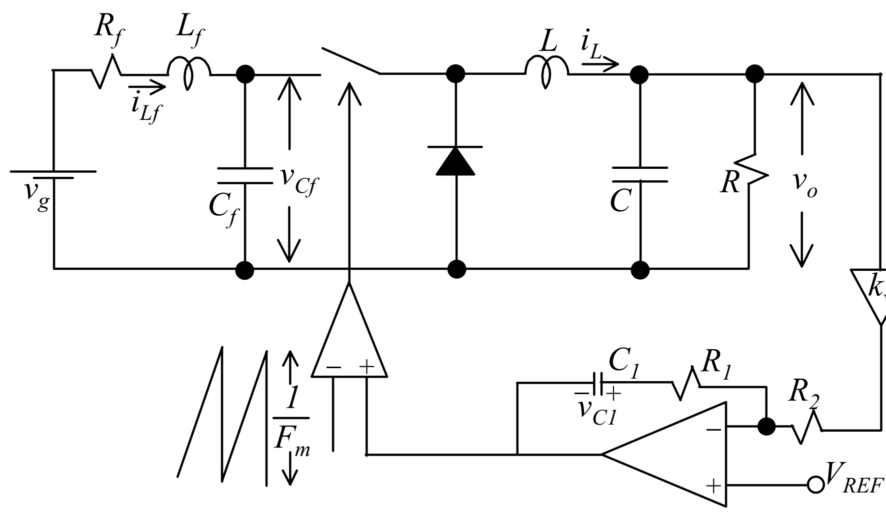

Figure 9.1. DC-DC Buck Converter with Input Filter

The resistance R_f in the input filter is chosen as the bifurcation parameter and the system behavior as a function of R_f is studied. The converter is regulated by a simple PI voltage controller as shown in 9.1. The integrated filter converter system with the PWM switch in Figure 9.1 replaced by its average model is shown in Figure 9.2. Since the bifurcation analysis is performed on the average model of the converter, interactions with frequencies in the switching frequency range between the converter and the filter cannot be captured by this method.

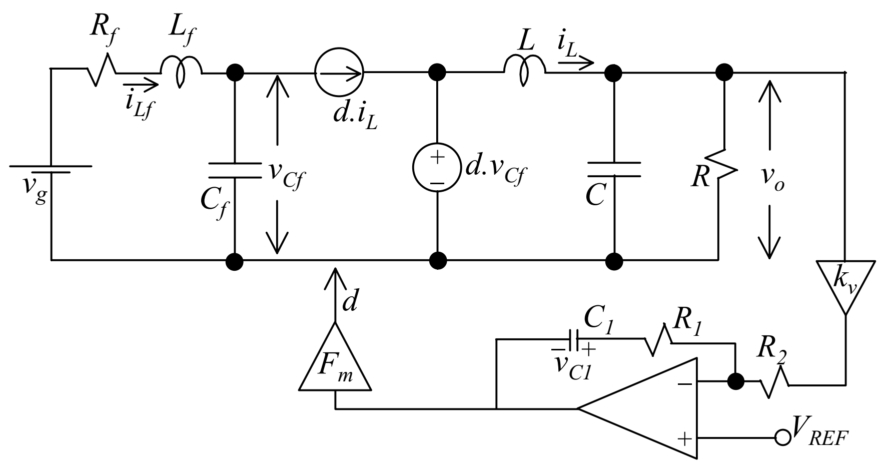

Figure 9.2. Average Model of DC-DC Buck Converter with Input Filter

Denoting the gain R_1/R_2 by h_o, the dynamic state space equations of the average model shown in Figure 9.2 are given below:

$$
\begin{aligned}
&L\frac{di_L}{dt} = (1+h_o)F_m V_{REF} v_{Cf} - h_o k_v F_m v_o v_{Cf} - F_m v_{C1} v_{Cf} - v_o \\
&C\frac{dv_o}{dt} = i_L - \frac{v_o}{R} \\
&L_f \frac{di_{Lf}}{dt} = v_g - R_f i_{Lf} - v_{Cf} \\
&C_f \frac{dv_{Cf}}{dt} = i_{Lf} - (1+h_o)F_m V_{REF} i_L + h_o k_v F_m i_L v_o + F_m v_{C1} i_L \\
&C_1 \frac{dv_{C1}}{dt} = \frac{1}{R_1}(k_v v_o - V_{REF})
\end{aligned}
\tag{9.1}
$$

The duty cycle d, is given by:

$$d = [(1+h_o)V_{REF} - h_o k_v v_o - v_{C1}]F_m \tag{9.2}$$

To reduce notational clutter, the state equations for the system are written as:

$$\dot{x} = f(x; R_f) \tag{9.3}$$

where, x, represents the state vector $[i_L\ v_o\ i_{Lf}\ v_{Cf}\ v_{C1}]^T$. The equilibrium solutions $x_e=[I_{Le}\ V_{oe}\ I_{Lfe}\ V_{Cfe}\ V_{C1e}]^T$ for the system are determined by setting the state derivatives in Equation (9.1) equal to zero and solving the resulting system of algebraic equations.

$$0 = f(x;R_f) \Rightarrow x = x_e \tag{9.4}$$

The equilibrium solutions are given by:

$$\begin{aligned}
I_{Le} &= \frac{V_{REF}}{k_v}\cdot\frac{1}{R}\\
V_{oe} &= \frac{V_{REF}}{k_v}\\
I_{Lfe} &= \frac{\left(\dfrac{V_{REF}}{k_v}\right)^2\cdot\dfrac{1}{R}}{V_g \pm \sqrt{V_g^2 - 4\dfrac{R_f}{R}\left(\dfrac{V_{REF}}{k_v}\right)^2}}\\
V_{Cfe} &= V_g \pm \sqrt{V_g^2 - 4\frac{R_f}{R}\left(\frac{V_{REF}}{k_v}\right)^2}\\
V_{C1e} &= V_{REF} - \frac{V_{REF}}{k_v}\cdot\frac{1}{V_g \pm \sqrt{V_g^2 - 4\dfrac{R_f}{R}\left(\dfrac{V_{REF}}{k_v}\right)^2}}
\end{aligned} \tag{9.5}$$

The loci of the equilibrium solutions as a function of R_f is shown in Figure 9.3.

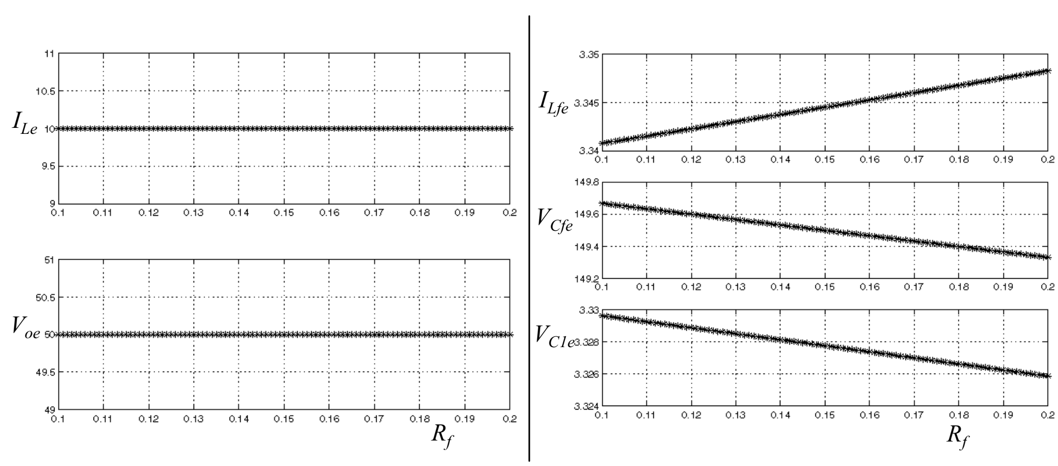

Figure 9.3. Loci of Equilibrium Solutions as a Function of R_f

The linearized system equations around the equilibrium solutions defined by Equation (9.5) are given by Equation (9.6). The location of the eigenvalues of the linearized system determines the stability of the system in the neighborhood of the equilibrium point x_e.

$$J(x_e; R_f) = \left.\frac{\partial f(x; R_f)}{\partial x}\right|_{x=x_e} \tag{9.6}$$

As the eigenvalues move in the complex plane as a function of the control parameter, the system loses stability for a particular value of R_f in one of two ways as shown in Figure 9.4.

An eigenvalue moves to the right half plane through the origin. This is called a static bifurcation.

A pair of complex conjugate eigenvalues moves to the right half plane with non-zero imaginary parts. This is called a dynamic or Andronov-Hopf bifurcation.

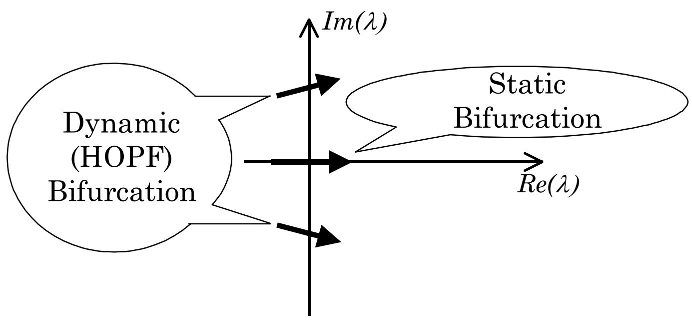

Figure 9.4. Loss of System Stability

The loci of eigenvalues of the linearized system for the DC-DC buck converter with input filter is shown in Figure 9.5. It can be seen that a pair of complex conjugate eigenvalues λ_1 and λ_2, move to the right half of the complex plane with non-zero imaginary parts. The system thus suffers a dynamic Andronov-Hopf bifurcation. An Andronov-Hopf bifurcation indicates the existence of periodic solutions. The stability of the periodic solutions near the bifurcation point is determined by the type of bifurcation.

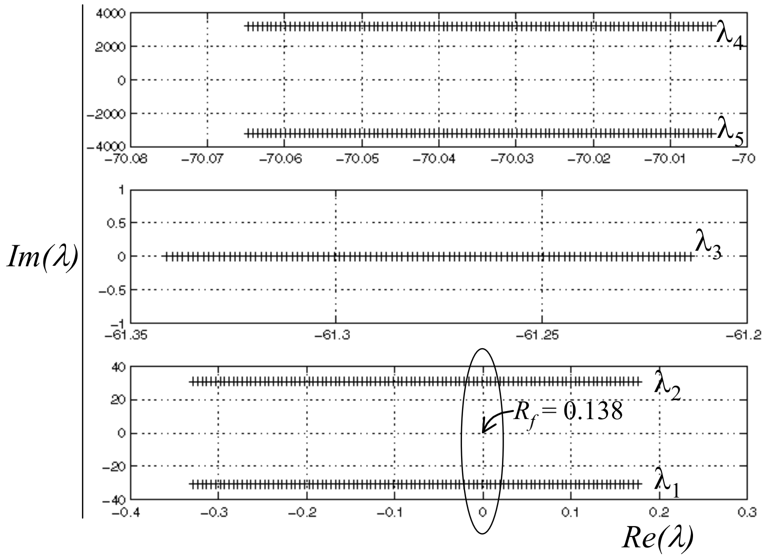

Figure 9.5. Loci of Eigenvalues of Linearized System as a function of R_f

A Hopf bifurcation is further classified as supercritical and subcritical. By using perturbation methods, "Normal Form" equations [61] that describe the behavior of the system near the bifurcation points are derived. The generic normal form equations for a Hopf bifurcation are given below:

$$\dot{a} = \mu a + \alpha a^3 \qquad (9.7)$$
$$\dot{\theta} = \omega + \beta a^2$$

Depending on the sign of α, the bifurcation is supercritical or subcritical. A negative α indicates a supercritical Hopf and a positive α, a subcritical Hopf. A subcritical Hopf bifurcation is characterized by unstable periodic solutions bifurcating from the Hopf point. A supercritical Hopf bifurcation would, on the other hand, have stable periodic solutions bifurcating from the Hopf point. For the system under study, the bifurcation was found to be subcritical. The complete bifurcation diagram of the DC-DC buck converter with input filter is shown in Figure 9.6. The periodic solutions that bifurcate from the Hopf point are numerically constructed using shooting methods. A branch of periodic solutions as a function of the control parameter R_f can then be traced using one of several methods such as sequential, arc-length or pseudo arc-length continuation. The stability of the bifurcating periodic solutions is determined using Floquet theory. The construction, branch continuation and determination of stability of periodic solutions is explained in detail in the following section.

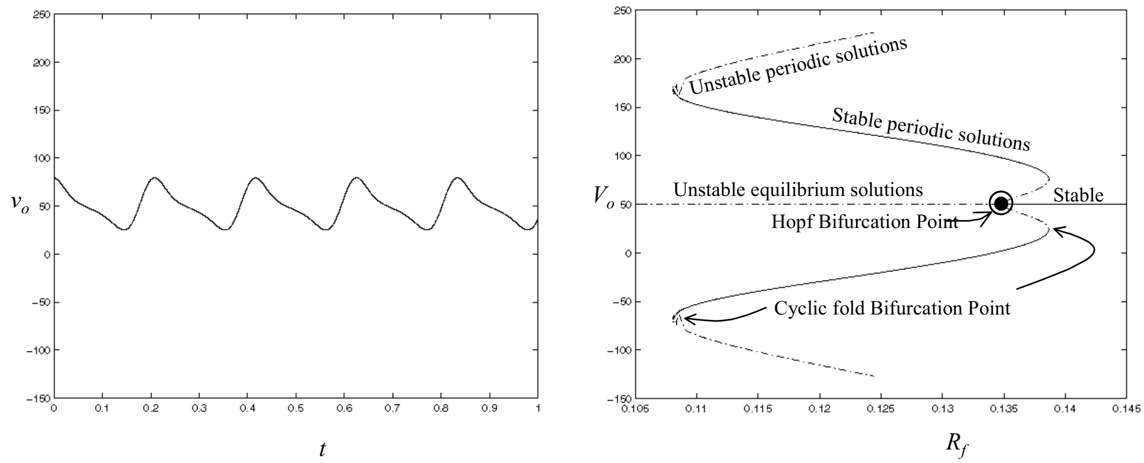

Figure 9.6. Bifurcation Diagram of DC-DC Buck Converter with Input Filter

9.2.1 Construction and Stability of Periodic Solutions

The construction of periodic solutions basically involves the determination of initial conditions, x_o and a solution, $x(t;x_o)$ with a minimal period T for the system equations (Equation (9.1)) such that $x(T;x_o) = x_o$. To absorb the problem of determining the minimal period T of the periodic solutions into that of the initial conditions x_o, the following transformations are performed on the state equations.

$$
\begin{aligned}
&t = \tau T \\
&\frac{dx}{dt} = \frac{dx}{d\tau} \cdot \frac{d\tau}{dt} = \frac{1}{T}\frac{dx}{d\tau} \\
&\Rightarrow x' = \frac{dx}{d\tau} = T\frac{dx}{dt} = T \cdot \dot{x} = T \cdot f(x; R_f)
\end{aligned}
\tag{9.8}
$$

The augmented state equations with initial conditions are given below in Equation (9.9)

$$
\begin{aligned}
x' &= Tf(x;R_f) \\
T' &= 0
\end{aligned}
\qquad
\begin{bmatrix} x(1;x_o) - x_o \\ x_k(0) - \eta \end{bmatrix} = 0
\tag{9.9}
$$

The initial condition, $x_k(0) = \eta$ in Equation (9.9) represents a phase condition for one of the state variables to account for additional state equation that was introduced due to the normalization.

To trace a branch of periodic solutions as a function of the control parameter R_f, the initial condition x_o and the minimal period T need to be determined with R_f as the continuation parameter along the branch. On the other hand, subsequent values of R_f at appropriate intervals along the branch of the periodic solutions can be determined by the continuation algorithm itself if the arc length s, is chosen as the continuation parameter. Hence, R_f is added as an additional state variable to the transformed state equations. The augmented state vector and the dynamic equations are denoted by an underscore as shown in Equation (9.10).

$$\begin{array}{ll} x' = Tf(x;R_f) & \\ T' = 0 & \begin{bmatrix} x(1;x_o) - x_o \\ x_k(0) - \eta \\ p(x_o,T,R_f,s) \end{bmatrix} = 0 \\ R_f' = 0 & \end{array} \tag{9.10}$$

$$\underline{x}' = \underline{f}(\underline{x}) \quad G(\underline{x}_o) = 0$$
$$\underline{x} = [x^T \quad T \quad R_f]$$

The initial conditions x_o, minimal period T and, R_f are determined as a solution to a two-point boundary value problem [61,62]. The problem to be solved is given by Equation (9.10). The additional boundary condition in Equation (9.10) is given by:

$$\begin{aligned} p(x_o,T,R_f,s) &= \varsigma \sum_{i=1}^{5} \left(x_{oi} - x_{oi}(s_j)\right)\frac{dx_{oi}}{ds} + \varsigma\left(T - T(s_j)\right)\frac{dT}{ds} \\ &\quad + (1-\varsigma)\left(R_f - R_f(s_j)\right)\frac{dR_f}{ds} - (s - s_j) \end{aligned} \tag{9.11}$$

The required initial condition $\underline{x}_o=[x_o^T\ T\ R_f]^T$ is that for which $G(x_o,T,R_f,x(1;x_o))$ given by Equation (9.12) is equal to zero.

$$G(x_o,T,R_f,x(1;x_o)) = G(\underline{x}_o, x(1;\underline{x}_o)) = \begin{bmatrix} x(1;x_o) - x_o \\ x_k(0) - \eta \\ p(x_o,T,R_f,s) \end{bmatrix} \tag{9.12}$$

A Newton-Raphson iterative procedure explained below is used to determine the initial conditions. A initial guess $\underline{x}_o^{(i)}$ is used as a starting point. The subsequent solutions are found as follows:

$$
\begin{aligned}
&G^{(i+1)} = G^{(i)} + \left(\underline{x}_o^{(i+1)} - \underline{x}_o^{(i)}\right)G'^{(i)} = 0 \\
&\Rightarrow \underline{x}_o^{(i+1)} = \underline{x}_o^{(i)} - \left[G'^{(i)}\right]^{-1} G^{(i)}
\end{aligned}
\tag{9.13}
$$

where, $G^{(i)}=G(\underline{x}_o^{(i)},x(1;\underline{x}_o^{(i)})$. The gradient of G at the i^{th} initial condition is given by:

$$
\begin{aligned}
G'^{(i)} &= \frac{\partial G}{\partial \underline{x}_o^{(i)}} + \frac{\partial G}{\partial x} \cdot \frac{\partial x(1;\underline{x}_o^{(i)})}{\partial \underline{x}_o^{(i)}} \\
&= B_o + B_1 \cdot Y(\tau)\Big|_{\tau=1}
\end{aligned}
\tag{9.14}
$$

The matrices B_o and B_1 are defined below assuming that the index k in the phase condition in Equation (9.12) is chosen as 4:

$$
B_o = \begin{bmatrix}
1 & 0 & 0 & 0 & 0 & 0 & 0 \\
0 & 1 & 0 & 0 & 0 & 0 & 0 \\
0 & 0 & 1 & 0 & 0 & 0 & 0 \\
0 & 0 & 0 & 1 & 0 & 0 & 0 \\
0 & 0 & 0 & 0 & 1 & 0 & 0 \\
0 & 0 & 0 & 1 & 0 & 0 & 0 \\
\frac{dx_{o1}}{ds} & \frac{dx_{o2}}{ds} & \frac{dx_{o3}}{ds} & \frac{dx_{o4}}{ds} & \frac{dx_{o5}}{ds} & \frac{dT}{ds} & \frac{dR_f}{ds}
\end{bmatrix}
\tag{9.15)a}
$$

$$
B_1 = \begin{bmatrix}
-1 & 0 & 0 & 0 & 0 & 0 & 0 \\
0 & -1 & 0 & 0 & 0 & 0 & 0 \\
0 & 0 & -1 & 0 & 0 & 0 & 0 \\
0 & 0 & 0 & -1 & 0 & 0 & 0 \\
0 & 0 & 0 & 0 & -1 & 0 & 0 \\
0 & 0 & 0 & 0 & 0 & 0 & 0 \\
0 & 0 & 0 & 0 & 0 & 0 & 0
\end{bmatrix}
\tag{9.15)b}
$$

The derivatives in the last column of the matrix B_o are determined as follows. Assuming that the initial condition x_o, minimal period T and the control parameter R_f have been found on a particular point on a branch we have,

$$G(x_o, T, R_f, s) = 0$$
$$\Rightarrow \frac{\partial G}{\partial x_o} \cdot \frac{\partial x_o}{\partial s} + \frac{\partial G}{\partial T} \cdot \frac{\partial T}{\partial s} + \frac{\partial G}{\partial R_f} \cdot \frac{\partial R_f}{\partial s} = 0$$
$$\Rightarrow \begin{bmatrix} \frac{\partial x_o}{\partial s} \\ \frac{\partial T}{\partial s} \\ \frac{\partial R_f}{\partial s} \end{bmatrix} = -\begin{bmatrix} \begin{bmatrix} \frac{\partial G}{\partial x_o} & \frac{\partial G}{\partial T} \end{bmatrix}^{-1} \frac{\partial G}{\partial R_f} \\ 1 \end{bmatrix} \frac{\partial R_f}{\partial s} \tag{9.16}$$

The partial derivatives in Equation (9.16) are determined in terms of $\partial R_f / \partial s$. The vector is then normalized to have unit length. The quantities on the right hand side of Equation (9.16) are defined below.

$$\frac{\partial G}{\partial x_o} = I - \frac{\partial x(1; x_o, R_f)}{\partial x_o} \tag{9.17}$$
$$\frac{\partial G}{\partial T} = f(x(1), x_o, R_f)$$

The matrix $Y(\tau) = \frac{\partial x(\tau; \underline{x}_o^{(i)})}{\partial \underline{x}_o^{(i)}}$ in Equation (9.17) is the n×n fundamental solution defined by:

$$Y'(\tau) = A(\tau) Y(\tau) \quad 0 < \tau < 1 \tag{9.18}$$
$$Y(0) = I \qquad A(\tau) = \frac{\partial f(\underline{x}(\tau); \underline{x}_o)}{\partial \underline{x}(\tau)}$$

$A(\tau)$ represents the Jacobian of the linearized system around the constructed periodic solution. In the actual computation, the $A(\tau)$ and the solution $\underline{x}(\tau; \underline{x}_o)$ are replaced by their numerical approximations obtained by solving the problem with the initially guessed solutions.

After computing $Y(\tau) = \left. \frac{\partial x(\tau; \underline{x}_o^{(i)})}{\partial \underline{x}_o^{(i)}} \right|_{\tau=1}$, it is substituted in Equation (9.17) for the gradient of G, which in turn yields the new solution from Equation (9.16). The procedure is repeated until a convergence condition is met and continued as a function of the arc length s. The stability of the bifurcating periodic solutions is determined using Floquet theory [61]. After a periodic solution $x(t;x_o)$ with minimal period T is constructed, a by-product of the construction algorithm is the monodromy matrix Φ given by:

$$\Phi = \frac{\partial \underline{x}(1;\underline{x}_o)}{\partial \underline{x}_o} \tag{9.19}$$

The location of the eigenvalues of the monodromy matrix determines the stability of the periodic solution. If the eigenvalues of the monodromy matrix are inside the unit circle, the periodic solution is stable. As the control parameter R_f is varied, the eigenvalues of Φ move in the complex plane and may exit the unit circle in one of three ways as shown in Figure 9.7.

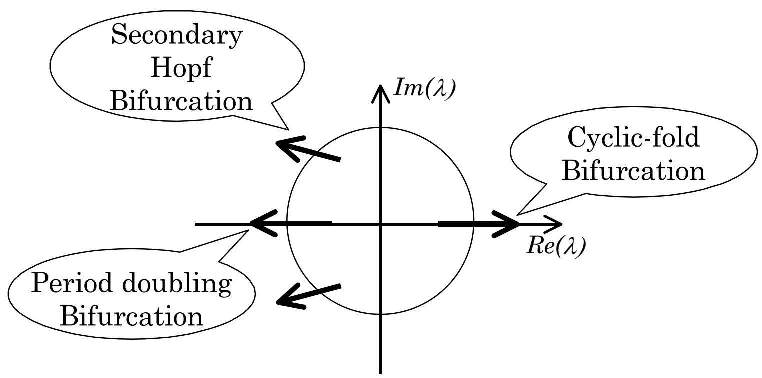

Figure 9.7. Bifurcation of Periodic Solutions

For the DC-DC buck converter with input filter, the eigenvalues of the monodromy matrix leave the unit circle through the (*1,0*) point. The system suffers a cyclic-fold bifurcation wherein a stable branch of periodic solutions loses stability and continues as an unstable branch of periodic solutions (Figure 9.6).

9.2.2 Comparison with Linear Analysis

Figure 9.8 illustrates the application of the impedance ratio criterion. It can be seen that, according to Equation (9.37) the system is guaranteed to be stable for $R_f > 0.25$. The linear analysis technique provides information only about system stability as the control parameter is varied. Information regarding the type and multiplicity of solutions as provided by the bifurcation diagram cannot be obtained from linear analysis. Figure 9.9 shows a comparison between the linear and bifurcation analyses results.

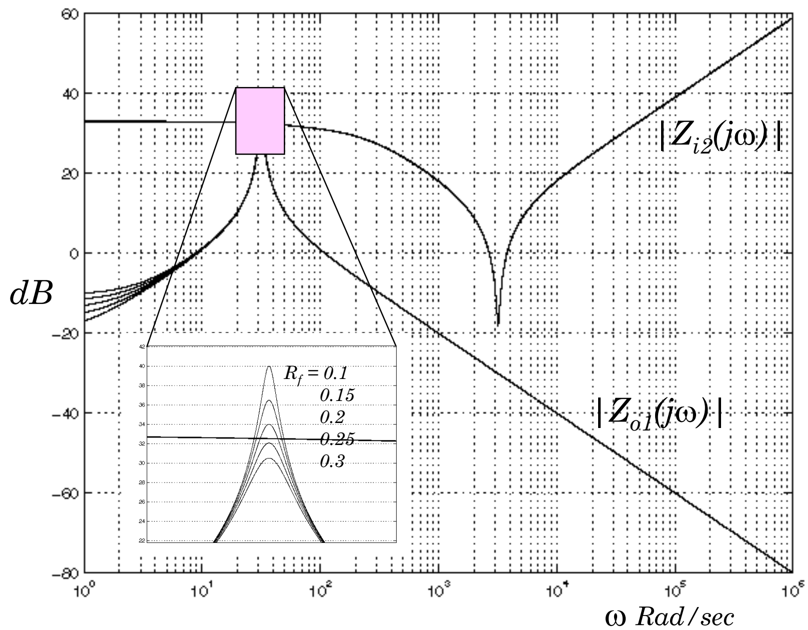

Figure 9.8. Middlebrook Criterion

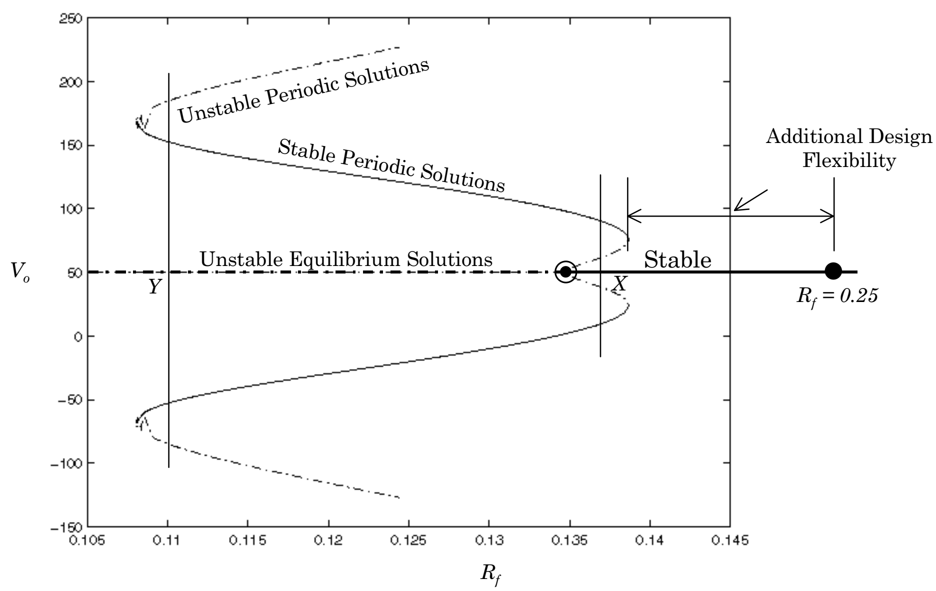

Figure 9.9. Comparison between Linear and Bifurcation Analysis

It is important to note from Figure 9.9 that a stable equilibrium solution (say X) can be perturbed strongly enough to drive the system to a periodic solution. On the other hand, an unstable equilibrium point (say Y) does not lead to catastrophic results when perturbed but only ends up in a stable periodic solution. Such an observation cannot be made from conventional linear analysis methods such as the Middlebrook Impedance Ratio Criterion. In addition, linear analysis provided a conservative estimate of system stability in this case. The Hopf point is at $R_f = 0.138$ where the equilibrium solution loses stability whereas the Middlebrook criterion provides a lower bound of $R_f = 0.25$. A clearer understanding of the system aided by the use of nonlinear analysis methods can hence help in newer design rules, control laws that optimize performance, cost, size and reliability.

9.3 INTERACTION AT THE DC BUS

The interaction at the DC bus, shown in Figure 9.10, between the bus regulator and a load converter is discussed in this section. The load subsystem represented by Subsystem 2 in Figure 9.10 is a regulated DC-DC converter with a front-end input filter. The other loads on the DC bus are modeled by a current source, negative impedance (other regulated power converters) or a simple resistance.

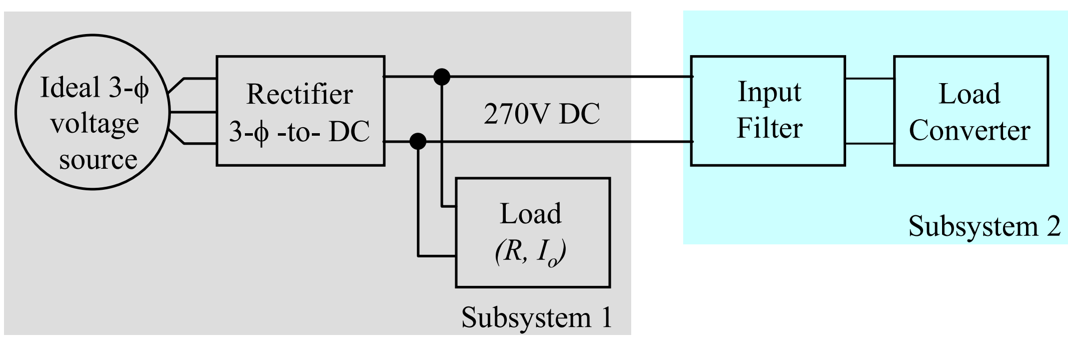

Figure 9.10. Simplified Power System Architecture

The three-phase boost rectifier is represented by its average model in rotating *dq*-coordinates synchronized with the input line voltages [47]. The load converter is also represented by its corresponding average model.

9.3.1 Stability Analysis

The circuit schematic of the simplified power system is shown in Figure 9.11.

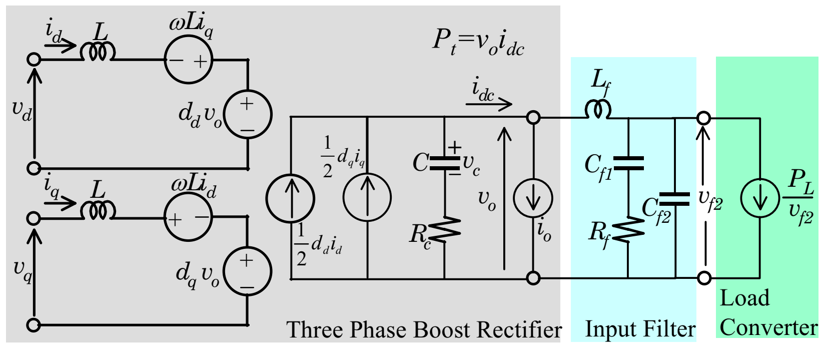

Figure 9.11. Circuit Schematic of Simplified Power System

The total power supplied by the boost rectifier is given by $P_t=v_o i_{dc}$ (Figure 9.11). The DC-DC converter in subsystem 2 is represented by a constant power load with the same modifications as in [50]. The input filter is a two-stage configuration with the damping resistance in a shunt path to minimize the power loss.

The first step in the analysis of the baseline system is the determination of the control parameter(s) for the bifurcation analysis. The three phase boost rectifier feeds the DC distribution bus of the baseline power system with a stiff regulated voltage of 270V. A control block diagram of the three phase boost rectifier is shown in Figure 9.12.

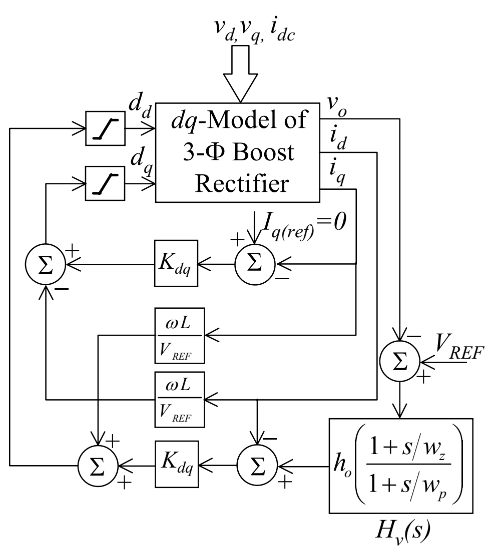

Figure 9.12. Control block diagram of three-phase boost rectifier

One of the critical performance indices of the rectifier is its bandwidth of regulation. This parameter can be related to the transient response and disturbance rejection properties of the rectifier. In addition, the bandwidth is intimately related to the stability of the rectifier and hence of the baseline system. The gain h_o of the voltage controller $H_v(s)$ (Figure 9.12) is directly related to the bandwidth of the rectifier and hence is chosen as the control parameter for the bifurcation analysis of the baseline system. The stability analysis proceeds as follows: The stability of the equilibrium solutions of the baseline system is determined as a function of the control parameter, h_o. The total power P_t, supplied by the boost rectifier is divided equally between the constant current load i_o, and the constant power load P_L/v_{f2}. The complete bifurcation diagram for the baseline system for $P_t=8kW$ is shown in Figure 9.13a.

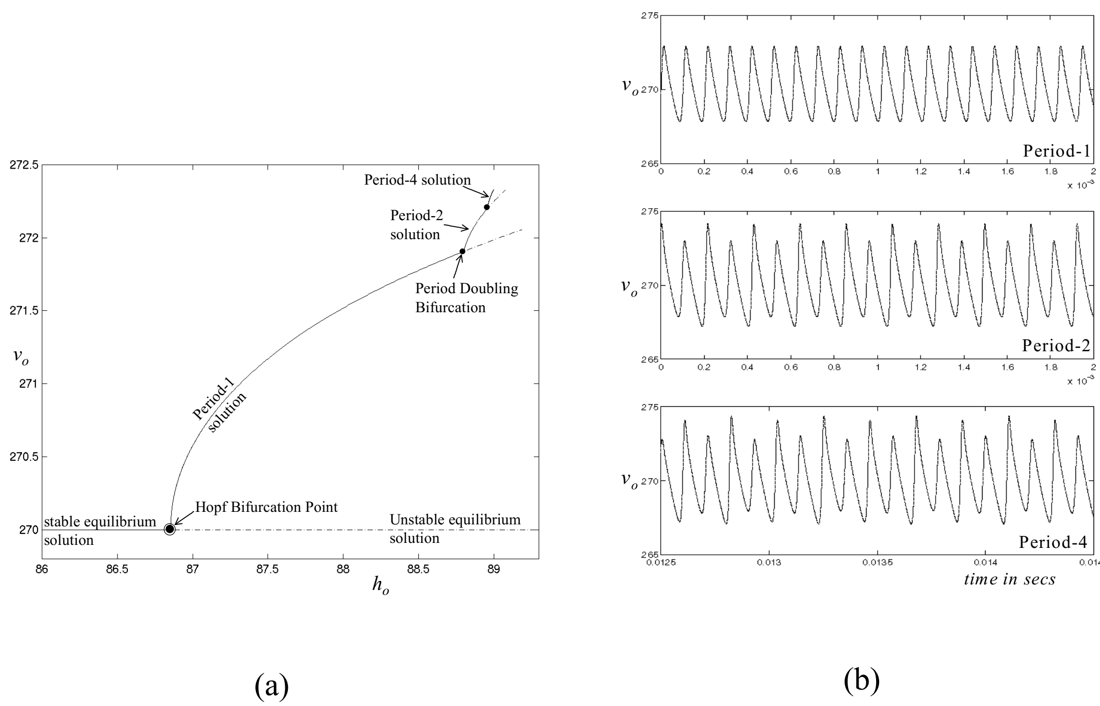

Figure 9.13. (a) Bifurcation Diagram of Baseline System as a function of h_o for $P_t=8kW$ (b) Periodic Solutions of Baseline System

The equilibrium point loses stability through a Hopf bifurcation at $h_o=86.8295$ for $P_t=8kW$. The normal form equations (Equation (9.7)) of the system at the Hopf point indicate that the bifurcation is supercritical (i.e.) the bifurcating periodic solutions are stable as shown in Figure 9.13a. The branch of periodic solutions is followed using the pseudo-arc length continuation procedure described in the previous section. The stability of the constructed periodic solutions is monitored by observing the corresponding Floquet multipliers. As mentioned in the previous section, the floquet multipliers move in the complex plane as a function of the control parameter and may exit the unit circle in one of three ways as shown in Figure 9.7. A period doubling bifurcation occurs at $h_o=88.7904$ where, one Floquet multiplier exits the unit circle through (-1,0). This is followed by another period doubling bifurcation to a period-4 solution. These periodic solutions are shown in Figure 9.13b.

9.3.2 Dependence on Parameter Values

The baseline system considered in this paper consists of two interconnected nonlinear subsystems namely, the three phase boost rectifier and the regulated load converter with input filter. The analysis method presented above considers the stability of the baseline system as a whole, regardless of the stability of the individual subsystems. To this end, as the control parameter is varied, the stability of the three phase boost rectifier as a standalone system terminated by the load P_t, is determined, in addition to that of the baseline system. The parameter values that yield the results shown in Figure 9.13 are such that, the equilibrium point of the boost rectifier as a standalone system loses its stability before that of the baseline system (i.e.) for $h_o<86.8295$. Such a situation is only of academic interest as it defeats the entire purpose of subsystem integration in that an unstable system (the boost rectifier) is integrated with a stable system (the filter-load converter subsystem) to form the stable baseline system. However, a different set of parameter values can result in an unstable baseline system while preserving the stability of the individual subsystems. It is the parameters of the boost rectifier that determine the manner in which the baseline system loses stability.

Since, the load on the DC bus is not constant at all times, the rectifier should provide “good” regulation of the DC bus voltage at all load levels. Since the baseline system is essentially nonlinear, the bandwidth of the regulator can be expected to change significantly with the load. Hence, it becomes important to study the effect of the regulation bandwidth of the rectifier on the stability of the baseline system for different values of power P_t. The values of h_o for which the baseline system loses stability were determined for different values of power P_t. For each value of P_t, the type of the Hopf bifurcation was determined by obtaining the normal form equations of the baseline system. The values of α_2 in the normal form equations are given in Table 9.1 for different values of power P_t.

Table 9.1. α_2 for Case 1 and Case 2.

P_t (kW)	***Case 1***		***Case 1***	
	α_2	$h_{o(hopf)}$	$\alpha_2(10^{-6})$	$h_{o(hopf)}$
8	*-0.01213*	*86.8295*	*26.9384*	*19.5325*
16	*-0.00818*	*45.8968*	*12.6145*	*8.5091*
24	*-0.00733*	*31.9366*	*4.6564*	*5.4051*
32	*-0.00854*	*24.6799*	*-3.0179*	*4.0491*
40	*-0.00773*	*19.9758*	*-6.4271*	*3.3109*
48	*-0.00214*	*16.5835*	*4.6585*	*2.8485*
56	*0.005724*	*14.0965*	*38.5256*	*2.5291*

In Table 9.1, case 1 is identified as the situation where the baseline system preserves its stability in spite of the boost rectifier being unstable, and that wherein the baseline system loses its stability with the individual subsystems being stable is identified as case 2. It can be seen from Table 9.1 that, the type of bifurcation for case 2 changes from subcritical to supercritical and back as the power is increased. Further investigation is necessary to identify the reasons for such a behavior. However, the normal form equations provide an idea about the post-bifurcation behavior of the system, which can be used to design fault-clearing systems in the event of an instability. In addition, it can be seen from Table 9.1, that the values of h_o for which the baseline system loses stability, decrease with increasing power. Hence, with the knowledge of the maximum possible load on the DC bus, h_o can be chosen such that the equilibrium solutions are stable at all load power levels or can be adaptively varied as a function of the load for optimal performance of the converter.

9.4 SUMMARY

Bifurcation methods were used to study the stability of a DC-DC converter with an input filter. The results obtained were then compared to the linear analysis results. The bifurcation analysis was extended to study the interaction at the DC bus between the bus regulator and a load converter in the presence of other loads in the system. Two distinct cases of loss of stability were identified and the dependence of system stability on parameter values was discussed. It was found that nonlinear methods provide information about the global behavior of the system. Knowledge of the system characteristics after the equilibrium point loses stability can be useful in designing fault-clearing mechanisms.

10 OPTIMAL PARAMETER UPDATE

10.1 INTRODUCTION

The bifurcation analysis results that were obtained in the previous chapter provide an improved understanding of the global behavior of the system compared to linear analysis techniques, which provide local information. However, they do not lend themselves very easily to incorporation into a design procedure or an optimization problem. In this section, we investigate the applicability of a simple design methodology used in power systems, based on bifurcation analysis, [63,64] to the design of subsystem components in the aircraft power distribution system. It was shown in the last chapter that as the bifurcation parameter was varied, the interconnected systems lose stability through a Hopf bifurcation. A Hopf bifurcation indicates the presence of oscillatory solutions. The stability of these solutions is determined from the normal form equations of the system at the bifurcation point. The design methodology presented in this section deals with the determination of an optimal direction in which the parameters of the system can be varied such that a Hopf bifurcation and hence oscillations of the system can be avoided thus improving the robustness of the nominal design. The potential that this method holds for extension to an optimization formulation is discussed.

10.2 BIFURCATION MARGIN

The system used to demonstrate the design methodology is based on that shown in Figure 9.10, however, with considerable simplifications. The 3-Φ to DC boost rectifier is replaced by a DC-DC boost converter and the load on the DC bus is lumped into a single DC current source. A block diagram of this simplified system is shown in Figure 10.1.

The boost converter is represented by its average model for the following analysis. The schematic of the average model of a DC-DC boost converter is shown in Figure 10.2. It can be seen that the duty cycle *d*, in Figure 10.2 is the duty cycle of the diode and not of the switch.

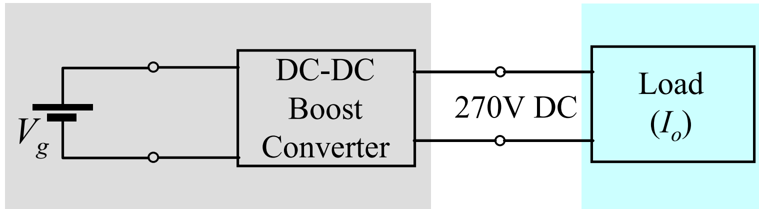

Figure 10.1. System block diagram

The converter is controlled using a multiloop controller consisting of an outer voltage loop and an inner average current loop.

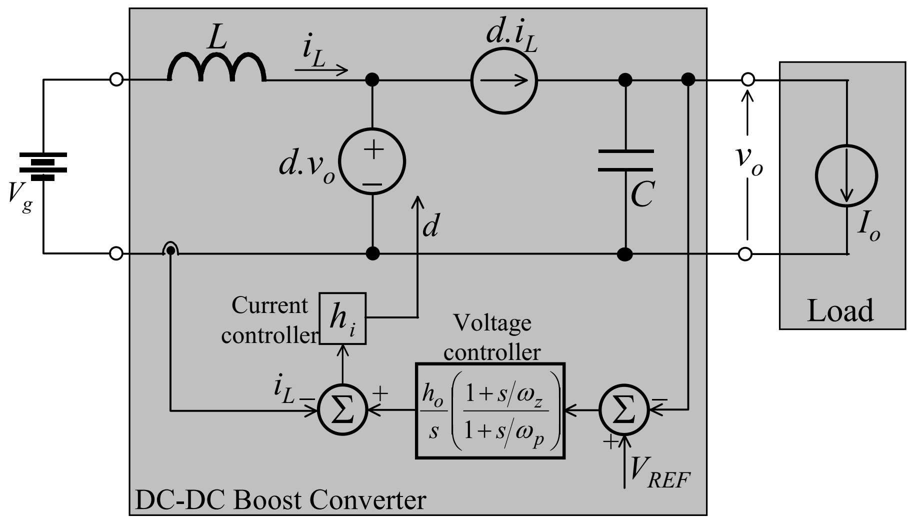

Figure 10.2. Average model of DC-DC boost converter with multiloop controller

The load current I_o is chosen as the bifurcation parameter as a function of which the stability of the system is monitored. The design variables of the system are chosen to be the voltage and current controller gains, namely h_o and h_i respectively. The design variable vector is defined as $p = [h_o\ h_i]$. The remaining parameters of the system are considered fixed in the analysis.

A control parameter vector $\lambda = [I_o, h_o, h_i]$ of the system, consisting of the bifurcation parameter and the design variable vector is defined. At the nominal operating point of the system, the control parameter vector is denoted by $\lambda_{nom} = [I_{o,nom}, h_{o,nom}, h_{i,nom}]$. The system suffers a Hopf bifurcation point at $\lambda_{hopf} = [I_{o,hopf}, h_{o,hopf}, h_{i,hopf}]$, with a simple pair of complex eigenvalues of the linearized system on the imaginary axis. The proximity of the nominal design to the Hopf bifurcation is measured by a bifurcation margin M. The bifurcation margin is defined as the distance between the bifurcation point and the nominal operating point. Hence, M is given by

$$M = \left\| \lambda_{hopf} - \lambda_{nom} \right\| \tag{10.1}$$

where, the distance measure in Equation (10.1) is the conventional Cartesian distance measure [63]. If only the bifurcation parameter I_o is varied with the design variables fixed at their nominal operating values, the bifurcation margin reduces to

$$M = \left\| I_{o,hopf} - I_{o,nom} \right\| \tag{10.2}$$

The goal of the design methodology is to determine the optimal direction of first order change in the design variable vector p such the bifurcation margin M is increased. The bifurcation margin is regarded as a function of the controller parameter vector and the gradient or the sensitivity $M_{\lambda/\lambda nom}$ of the margin M is computed such that the design may be incrementally improved by changing parameters in the direction $M_{\lambda/\lambda nom}$. The gradient $M_{\lambda/\lambda nom}$ is given by

$$M_{\lambda/\lambda_{nom}} = \left. \begin{bmatrix} \dfrac{\partial M}{\partial I_o} \\ \dfrac{\partial M}{\partial h_o} \\ \dfrac{\partial M}{\partial h_i} \end{bmatrix} \right|_{\lambda_{nom}} \tag{10.3}$$

Since the bifurcation paramater I_o cannot be controlled, the optimal direction of change is along the projection of the gradient $M_{\lambda/\lambda nom}$, on the design variable space. This projection $M_{p/pnom}$ is given by

$$M_{p/p_{nom}} = \left. \begin{bmatrix} \dfrac{\partial M}{\partial h_o} \\ \dfrac{\partial M}{\partial h_i} \end{bmatrix} \right|_{p_{nom}} \tag{10.4}$$

The computation of the gradient $M_{\lambda/\lambda nom}$, and hence the projection $M_{p/pnom}$, is described in the following section.

10.3 COMPUTATION OF THE GRADIENT

The computation of the gradient of the bifurcation margin for the DC-DC boost converter is presented in this section. The nonlinear state equations of the system shown in Figure 10.2 are given below

$$\dot{x} = \frac{d}{dt}\begin{bmatrix} i_L \\ v_o \\ v_{C1} \\ v_{C2} \end{bmatrix} = f(x,\lambda) = \begin{bmatrix} \left(v_g - d v_o\right)\frac{1}{L} \\ \left(d i_L - I_o\right)\frac{1}{C} \\ \left(v_{C2} - v_{C1}\right)\omega_z \\ \left[\left(v_o - V_{REF}\right)h_o - \left(v_{C2} - v_{C1}\right)\right]\omega_p \end{bmatrix} \tag{10.5}$$

where, the duty cycle d is given by,

$$d = \left(V_{REF} - v_{C2} - i_L\right)h_i \tag{10.6}$$

The variables v_{C1} and v_{C2} in Equations (10.5) and (10.6) correspond to the states in the voltage controller.

The Hopf bifurcation hypersurface is determined by the vanishing real parts of the eigenvalues of the linearized system. Specifically, Σ^{hopf} is defined as the space of control parameter vectors λ_{hopf} = [$I_{o,hopf}$, $h_{o,hopf}$, $h_{i,hopf}$] such that the system described by Equations (10.5) and (10.6) suffers a Hopf bifurcation. That is, with $\lambda = \lambda_{hopf}$ the Jacobian of the system given by

$$f_x(x,\lambda) = \frac{\partial f}{\partial x} = \begin{bmatrix} h_i\frac{v_o}{L} & -h_i\frac{\left(V_{REF} - v_{C2} - i_L\right)}{L} & 0 & h_i\frac{v_o}{L} \\ h_i\frac{\left(V_{REF} - v_{C2} - 2i_L\right)}{C} & 0 & 0 & -h_i\frac{i_L}{C} \\ 0 & 0 & -\omega_z & \omega_z \\ 0 & h_o\omega_p & \omega_p & -\omega_p \end{bmatrix} \tag{10.7}$$

when evaluated at the equilibrium solution (x_{hopf}, λ_{hopf}) has a simple pair of eigenvalues $\pm j\omega_{hopf}$, and all other eigenvalues with nonzero real parts. The bifurcation hypersurface for the system under consideration is the load current $I_{o,hopf}$ for which the system undergoes a Hopf bifurcation plotted as a function of the design variables h_o and h_i as shown in Figure 10.3.

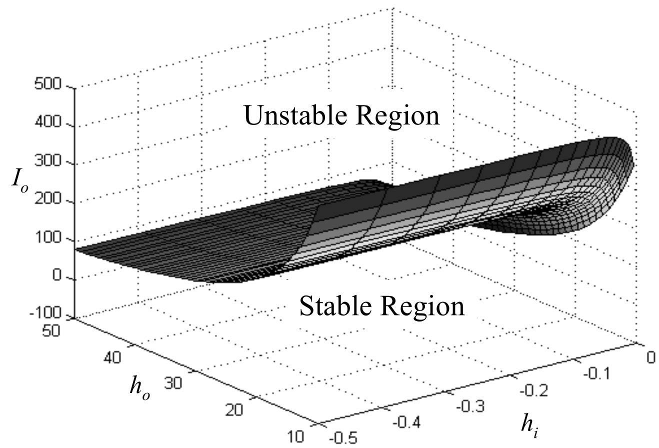

Figure 10.3. The Hopf bifurcation hypersurface.

It is shown in [63] that the gradient $M_{\lambda/\lambda nom}$ given by Equation (10.3), is essentially a function of the normal vector to the Hopf bifurcation hypersurface Σ^{hopf}. The normal vector, in turn is given by the sensitivity or the gradient of the real part of the eigenvalues of the linearized system with respect to the control parameter vector λ at the bifurcation point as given by

$$N(\lambda_{hopf}) = \frac{d}{d\lambda}\left[\mathrm{Re}(\mu(\lambda))\right]\Big|_{\lambda_{hopf}} \tag{10.8}$$

where, $\mu(\lambda)$ represents the simple pair of complex eigenvalues whose real part goes to zero at $\lambda = \lambda_{hopf}$. The determination of the normal vector is described in the following. To start with, the equilibrium solutions $\mu(\lambda)$ of the system described by Equations (10.5) and (10.6) are given by

$$u(\lambda) = \begin{bmatrix} I_L \\ V_o \\ V_{C1} \\ V_{C2} \end{bmatrix} = \begin{bmatrix} I_o \dfrac{V_{REF}}{V_{dc}} \\ V_{REF} \\ V_{REF} - I_o \dfrac{V_{REF}}{V_{dc}} - \dfrac{V_{dc}}{V_{REF}} \dfrac{1}{h_i} \\ V_{REF} - I_o \dfrac{V_{REF}}{V_{dc}} - \dfrac{V_{dc}}{V_{REF}} \dfrac{1}{h_i} \end{bmatrix} \tag{10.9}$$

Let the right and left eigenvectors of the Jacobian given by Equation (10.7), corresponding to $\mu(\lambda)$ be denoted by $w^T(\lambda)$ and $v(\lambda)$ respectively. The eigenvectors are normalized according to $|\, v(\lambda)|=1$ and $w^T(\lambda)\, v(\lambda)=1$. Using this normalization, it can be easily shown that

$$\mu(\lambda) = w^T(\lambda) f_x(u(\lambda),\lambda) v(\lambda) \tag{10.10}$$

Differentiating $\mu(\lambda)$ with respect to the control parameter vector λ,

$$\begin{aligned} \frac{d}{d\lambda}[\mu(\lambda)] &= \frac{d}{d\lambda}\left[w^T f_x(u,\lambda) v\right] \\ &= w^T \frac{d}{d\lambda}(f_x(u,\lambda))v + \frac{d}{d\lambda}\left(w^T\right) f_x(u,\lambda)v + w f_x(u,\lambda)\frac{d}{d\lambda}(v) \\ &= w^T \frac{d}{d\lambda}(f_x(u,\lambda))v + \mu \frac{d}{d\lambda}\left(w^T v\right) \\ &= w^T \frac{d}{d\lambda}(f_x(u,\lambda))v \end{aligned} \tag{10.11}$$

The dependence on λ of the variables in Equations (10.11) is intentionally omitted to avoid notational clutter. Taking the real part of Equation (10.11) and using

$$\left.\frac{d}{d\lambda}[\mathrm{Re}(\mu(\lambda))]\right|_{\lambda_{hopf}} = \left.\mathrm{Re}\left[\frac{d}{d\lambda}(\mu(\lambda))\right]\right|_{\lambda_{hopf}} \tag{10.12}$$

the normal vector to the hypersurface, according to Equation (10.8), is obtained as

$$N(\lambda_{hopf}) = \left.\mathrm{Re}\left[w^T(\lambda)\frac{d}{d\lambda}(f_x(u(\lambda),\lambda))v(\lambda)\right]\right|_{\lambda_{hopf}} \tag{10.13}$$

Expanding the derivative of the Jacobian with respect to the control parameter in Equation (10.13), the normal vector is given by

$$N(\lambda_{hopf}) = \begin{bmatrix} n_{I_o} \\ n_{h_o} \\ n_{h_i} \end{bmatrix} = \mathrm{Re}\left.\begin{bmatrix} w^T(\lambda)\left[\frac{d}{dI_o}(f_x(u(\lambda),\lambda))\right]v(\lambda) \\ w^T(\lambda)\left[\frac{d}{dh_o}(f_x(u(\lambda),\lambda))\right]v(\lambda) \\ w^T(\lambda)\left[\frac{d}{dh_i}(f_x(u(\lambda),\lambda))\right]v(\lambda) \end{bmatrix}\right|_{\lambda_{hopf}} \tag{10.14}$$

The partial derivatives in Equation (10.14) are given by

$$\frac{d}{dI_o}\left(f_x\left(u(\lambda),\lambda\right)\right)=\begin{bmatrix} 0 & 0 & 0 & 0 \\ -\frac{1}{C}\frac{h_i V_{REF}}{V_g} & 0 & 0 & -\frac{1}{C}\frac{h_i V_{REF}}{V_g} \\ 0 & 0 & 0 & 0 \\ 0 & 0 & 0 & 0 \end{bmatrix} \tag{10.15)a$$

$$\frac{d}{dh_o}\left(f_x\left(u(\lambda),\lambda\right)\right)=\begin{bmatrix} 0 & 0 & 0 & 0 \\ 0 & 0 & 0 & 0 \\ 0 & 0 & 0 & 0 \\ 0 & \omega_p & 0 & 0 \end{bmatrix} \tag{10.15)b$$

$$\frac{d}{dh_i}\left(f_x\left(u(\lambda),\lambda\right)\right)=\begin{bmatrix} \frac{V_{REF}}{L} & 0 & 0 & \frac{V_{REF}}{L} \\ -\frac{1}{C}\frac{I_o V_{REF}}{V_g} & 0 & 0 & -\frac{1}{C}\frac{I_o V_{REF}}{V_g} \\ 0 & 0 & 0 & 0 \\ 0 & 0 & 0 & 0 \end{bmatrix} \tag{10.15)c$$

According to [63], the gradient $M_{\lambda/\lambda nom}$ of the bifurcation margin (Equation (10.2)) with respect to the control parameter vector λ is given by

$$M_{\lambda/\lambda_{nom}}=-\left(N\left(\lambda_{hopf}\right)^T\begin{bmatrix}1\\0\\0\end{bmatrix}\right)^{-1}N\left(\lambda_{hopf}\right)=-\frac{1}{n_{I_o}}\begin{bmatrix}n_{I_o}\\n_{h_o}\\n_{h_i}\end{bmatrix} \tag{10.16}$$

The geometric interpretation of Equation (10.16) is that the optimum direction to increase the distance with respect to the bifurcation parameter, namely I_o of a nominal design point λ_{nom} to the bifurcation hypersurface is antiparallel to the outward normal to the hypersurface. Hence, the optimum direction to vary the design variable vector is along the projection of the gradient given by Equation (10.16) on the design variable space. This projection can be obtained as

$$M_{p/p_o}=-\left(\frac{1}{n_{I_o}}\right)\begin{bmatrix}n_{h_o}\\n_{h_i}\end{bmatrix} \tag{10.17}$$

10.4 SIMULATION RESULTS

Simulation results of the DC-DC boost converter are presented in this section to demonstrate the proposed design methodology. Specifically, a nominal design is taken through a fixed number of design iterations to illustrate the incremental improvement in the design. The nominal operating condition is specified in terms of the nominal load current $I_{o,nom}$, and nominal design variable vector $p_{nom} = [h_{o,nom}\ h_{i,nom}]$. The nominal control parameter vector is hence, given by $\lambda_{nom} = [I_{o,nom}\ h_{o,nom}\ h_{i,nom}]$. The remaining variables in the converter are assumed fixed throughout the design process. For the given design variable vector p_{nom}, the load current $I_{o,hopf}$, for which the system suffers a Hopf bifurcation is determined from the bifurcation hypersurface shown in Figure 10.3. The corresponding control parameter vector on the bifurcation hypersurface is then $\lambda_{hopf} = [I_{o,hopf}\ h_{o,nom}\ h_{i,nom}]$. The projection of the normal vector to the hypersurface at λ_{hopf}, on the design variable space is determined from Equation (10.17). The nominal design is then incrementally improved by modifying the design variable vector $p_{nom} = [h_{o,nom}\ h_{i,nom}]$ along the projection. Figure 10.4 shows the optimal trajectory of the design variable vector from a given nominal design.

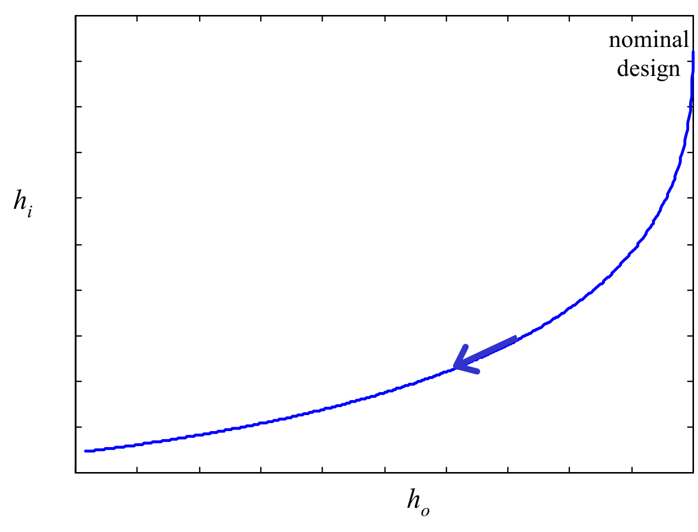

Figure 10.4. Optimal trajectory of design variable vector

At each point on the trajectory, the control parameter vector on the bifurcation hypersurface is determined. The projection on the design variable space, given by

Equation (10.17), of the normal vector to the bifurcation hypersurface at the control parameter vector is determined. The new design variable vector is then determined by modifying the previous vector, by an incremental magnitude, in the direction of the projection. The optimal trajectory informs the designer as to which of the parameters in the design variable vector, the stability of the system is more sensitive to. The direction of the arrow indicates the direction in which the design variables are modified. From Figure 10.4, it can be seen that the variation in h_i is greater than that of h_o initially. The phase margin of the linearized system is determined at each design point and is plotted in Figure 10.5 to illustrate that the robustness of the linearized system improves along the trajectory.

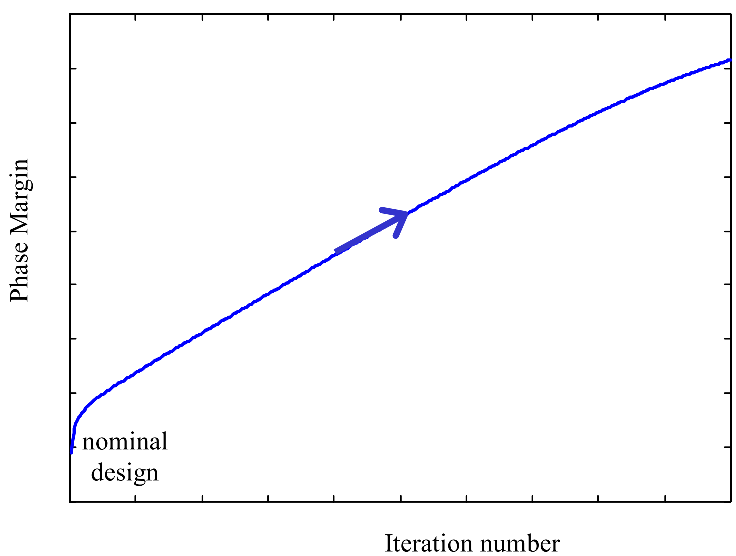

Figure 10.5. Phase Margin of linearized system

10.5 SUMMARY

A nonlinear design methodology used to determine the optimal direction to modify the design variables of a system such the instability through a Hopf bifurcation can be avoided was demonstrated on a DC-DC boost converter in this chapter. The load current of the converter was chosen as the bifurcation parameter. The voltage and current controller gains were chosen as the design variables with the other parameters in the system considered fixed. The Hopf bifurcation hypersurface was determined and the optimal direction to modify the design variables was found. This method can be incorporated into an optimization formulation by searching for the minimum weight design along the optimal direction.

11 CONCLUSIONS AND SUGGESTIONS FOR FUTURE RESEARCH

The research reported in this dissertation has focused on the development of optimization tools for the design of subsystems in a modern aircraft power distribution system. To this end, a baseline power distribution system was developed in collaboration with Lockheed Martin Control Systems. The baseline power system is built around a 270V DC distribution bus. The baseline system consists of bidirectional power converters that convert, control and condition the electrical power between the sources and the loads, electrical driven flight control actuators for maneuvering the control surfaces, structurally integrated smart actuators and other typical aircraft loads. The regeneration of energy from the flight control actuators under certain operating conditions was identified to be one of the distinguishing features of the power distribution system in that it requires the system to be able to process power both in the forward direction from the sources to the loads and in the reverse direction from the loads to the sources.

It was shown that the regenerative power from these flight control actuators occurs as a transient disturbance on the DC bus resulting in undesirable voltage swings of the DC bus voltage. On analysis of the actuator models and the process of regeneration, it was found that, under certain assumptions, the actuation loads could be represented by regulated power converters. The regenerative disturbance could then be equivalently modeled as a transient load disturbance to the regulated converter. Under these directions, a sample system consisting of a regulated DC-DC buck converter preceded by an EMI input filter was identified. The regenerative power was modeled as a transient load disturbance to the buck converter.

A well defined optimization methodology was developed for a sample system. The optimization methodology developed, however, is quite general in that it can be extended with minor modifications to other subsystems in the power distribution system.

The optimized design of the input filter was presented. This methodology is then extended to the regulated DC-DC buck converter, taking into account the increase in complexity of the converter. The procedure is then extended to the sample system as a whole to address system wide design considerations. Stability of the global system is insured, and the effects of regenerative power flow are minimized. It was shown that optimizing the integrated system as a whole results in a lesser weight than integrating the individually optimized systems.

Another source of regenerative energy in the power distribution system was identified to the structurally integrated smart actuators. The operating characteristics of these actuators are significantly different from the flight control actuators such as the EMA and the EHA. Hence, a significant portion of the dissertation was devoted to the study of piezoelectric actuators. This study included the development of a detailed electromechanical model of the piezoelectric actuator coupled to a simple mechanical structure. The model included the anhysteretic nonlinearity between the polarization and the electric field of the actuator. Using this model of the actuator, the optimized design of an amplifier that can be configured to synthesize a given reference current command into the actuator was formulated. This optimization procedure accounted for the actuator nonlinearity and yielded physically meaningful designs in a time efficient manner. Finally, a control law based on controlling the current into the actuator to be proportional to the acceleration of the structure in order to actively damp the structure was proposed. This control law resulted in the actuator absorbing the mechanical power injected into the structure by the external disturbance force to be redirected back to the electrical source. A detailed analysis of the electromechanical power transfer characteristics between the actuator and the drive amplifier was presented. Estimates of the peak current and voltage in the actuator were provided to enable design of the amplifier.

The optimization methodologies for the subsystems in the aircraft power distribution system must include constraints that guarantee the internal stability of each subsystem. In addition to ensuring the stability of individual subsystems, it is necessary to guarantee minimal interaction between interconnected subsystems and avoid unstable operation due to the integration of subsystems. The optimization formulation of the sample system described in Part I of the dissertation use linear stability constraints to guarantee the internal stability of subsystems. The classical Middlebrook impedance ratio criterion is used to ensure stability of interconnected subsystems by requiring that the terminal impedances of the individual subsystems at the interconnection be sufficiently separated.

The impedance ratio criterion is extended to a multivariable setting to make it applicable to three phase and single-phase AC interfaces. The multivariable impedance ratio criterion is defined in terms of the singular values of the terminal impedance matrices at the interconnection. The multivariable criterion is demonstrated in the study of the interaction between a three phase input filter and a three phase boost rectifier. This criterion, however, is based on linearized models and can only guarantee local stability. In order to study the stability of the subsystems under regenerative power flow conditions, a simplified analysis was presented that proved that the stability of an interconnected system consisting of a regulated power converter and an input filter is unaffected if the load current, in steady state, is flowing in the reverse direction towards the source.

To predict the global behavior of interconnected systems, bifurcation methods were used to provide information about the nature, stability and multiplicity of the solutions of the system as a function of a bifurcation parameter. Specifically, bifurcation methods were used to study the interaction between an input filter and a regulated DC-DC buck converter and at the DC bus between a bus regulator and a regulated load converter system. These bifurcation methods, despite providing information about the global stability characteristics of the system, are not immediately applicable to a design procedure and hence an optimization formulation. To this end, a simple design methodology based on bifurcation methods and widely used in the field of utility power systems, is investigated. This design procedure involves the determination of an optimal direction of updating the design variables of a system such that potential instabilities due to bifurcations are avoided. A simple DC-DC boost converter, represented by its average model, with a multiloop controller is used to demonstrate this design methodology.

11.1 Suggestions for Future Work

Power Distribution System Optimization

The optimization results of the sample system presented in Chapter 3 showed that the integrated optimization of the sample system as a whole resulted in a lower objective function than when the individually optimized designs were integrated. That is, the optimizer was able to utilize the interactions between the input filter and the converter and provide a lighter design. Hence, it appears advantageous to integrate the subsystems together and optimize the entire power distribution system as a whole. This approach, however, is not computationally feasible due to the significant increase in the number of design variables and constraints.

A novel multi-level optimization technique, commonly used in structural optimization, called global-local optimization can be used to optimize the power distribution as a whole yet, at a considerably lower computational cost. According to this method, the power distribution system is optimized at two levels, namely the local level and the global level, which interact with each other. The system to be optimized at the global level is the overall power distribution system. The subsystems at this level are represented by simplified, reduced order models with a minimal number of design variables and constraints. However, it is critical that the reduced order models at the global level capture, with reasonable accuracy, important performance characteristics of the power distribution system such as the effects of regenerative power, for example. The responses of the global system are then passed over the local level as interface quantities.

At the local level, the subsystems are represented by their detailed models with all the required complexity. On obtaining the interface quantities from the global model, the local optimizer performs a detailed optimization of the local subsystem for the given interface quantities and returns the corresponding objective function, namely the weight of the subsystem to the global level. The weights of the individual subsystems obtained from the local level, are then added to obtain the weight of the overall power distribution system. The global level optimizer iterates over the design variables of the global models such that the overall weight of the power distribution system is minimized. Since, the global level optimizer would go through a number of design iterations, it would be computationally expensive for the local level optimizers for each of the subsystems to determine the optimal local design for the interface quantities from the global level at each iteration. To alleviate this problem, the family of optimal designs can be developed at the local level for each subsystem for a reasonable range of interface quantities for each subsystem. These local level optimal designs can then be represented in the form of a response surface that returns the optimal weight as a function of the interface variables. This technique becomes even more powerful because of the presence of generic subsystems such as bidirectional power converters and EMI filters which are duplicated with minor modifications at several points in the power distribution system. Once these generic subsystems are identified, a series of local level optimizations can be performed and the response surfaces can be generated and stored in a design database, which can interact with the global level to provide fast and physically meaningful designs.

The challenge is however, the development of reduced global level models such that they are simple enough to be integrated to form the overall power distribution system, at the same time, being able to capture the essential performance characteristics of the power system. Another direction of research is the determination of interface quantities that are passed from the global level to the local level. The number of interface quantities cannot be so high that a prohibitive number of local optimization runs are required to generate the response surface.

The proposed optimization methodology for the sample system can be extended, with minor modifications, to include realistic actuator models. The flow of the regenerative energy can be traced and suitable control schemes can be devised to maximize the benefits and minimize its detrimental effects. Multiple actuator models can be included to study the transfer of energy between actuator when some are regenerating while the others are drawing power from the DC bus.

Piezoelectric Actuators

The optimization formulation for the design of the drive amplifier for the piezoelectric actuator can be extended to accommodate the control law proposed. The formulation presented in the dissertation assumes that the external disturbance force is zero. According the control law, however, the peak current and voltage in the actuator are dependent on the amplitude of the external force. An optimization problem can be formulated to design the amplifier, the current controller and the structural feedback constant. Inclusion of the current controller in the optimization formulation imposes limits on the maximum damping that can be added to the structure. The bandwidth of the amplifier current control loop is required to be significantly higher than that of the structural control loop so that the amplifier could be considered as an ideal current source and sink by the actuator. This difference in bandwidth was assumed in the analysis presented in Chapter 6. However, the optimization formulation can impose this bandwidth separation requirement as a performance constraint. This performance constraint would limit the acceleration feedback constant and hence the level of allowable damping that the actuator can add to the structure.

The nonlinearity can be included in the model of the actuator and estimates of real and reactive power can be obtained similar to those determined using the linear model. Due to the nonlinearity, it was shown that the voltage across the actuator consists of the fundamental, third and fifth harmonic components. Since the actuator current was sinusoidal, the duty cycle of the amplifier consists of the fundamental, third and fifth harmonics. The input current to the amplifier is a product of the duty cycle and the actuator current. Hence, the input current consists of a DC component to account for the real power flow from the actuator, and second, fourth and sixth harmonic components. This oscillatory component of the input current can cause considerable distortion of the DC bus voltage, which might not be acceptable for the satisfactory operation of other subsystems connected to the DC bus. The drive amplifier is commonly preceded by an

EMI input filter to attenuate the switching frequency noise from entering the DC bus. The input filter can also be sized to circulate the reactive power from the amplifier and not let it affect the DC bus. However, this makes the input filter heavier than when it had to attenuate only the switching frequency noise. Another option is to use additional power converters called bus conditioners at the input of the amplifier that can used to provide the circulating reactive power to the amplifier instead of the DC bus. Optimization methods can be used to explore the tradeoffs in weight, size and complexity between using input filters and bus conditioners to handle the reactive power on the DC bus from these actuators.

Stability Analysis

It was shown that nonlinear bifurcation methods were better than linear stability analysis methods in predicting the large signal stability properties of interconnected systems. However, these methods need to be simplified so that they provide physically meaningful results at a reduced computational cost and hence be used in the formulation of stability constraints for an optimization based design methodology. The nonlinear design methodology used to determine the optimal direction to update the design variable vector in order to incrementally improve the robustness of the system can be applied to an optimization methodology by searching for the minimum weight design along the optimal direction.

12 REFERENCES

1. MIL-STD-704E, Military Standard, *Aircraft Electric Power Characteristics*, May 1, 1991

2. Glennon T. F., "Fault tolerant generating and distributing system architecture", *IEE Colloquium on All Electric Aircraft*, June 1998, pp. 4/1-4/4.

3. Quigley R. E. J., "More Electric Aircraft", *Proceedings of the 8th Annual Power Electronics Conference and Exposition*, March 1993, pp. 906-911.

4. Elbuluk-Me, Kankam-Md, "Potential starter/generator technology for future aerospace application", *IEEE Aerospace and Electronics Systems Magazine,* vol. 11, no. 10, October 1996, pp. 17-24.

5. Richter E., Ferreira C., "Performance evaluation of a 250kW switched reluctance starter/generator", *Conference Record of the 1995 IEEE Industry Applications Conference*, vol. 1, October 1995, pp. 434-440.

6. Skvarenina TL, Wasynczuk O, Krause PC, Won Zon Chen, Thibodeaux RJ, Weimer J, "Simulation and analysis of a switched reluctance generator/More Electric Aircraft power system", *Proceedings of the 31st Intersociety Energy Conversion Engineering Conference*, vol. 1, August 1996, pp. 143-147.

7. Skvarenina TL, Pekarek S, Wasynczuk O, Krause PC, Thibodeaux RJ, Weimer J, "Simulation of a More Electric Aircraft power system using an automated state model approach", *Proceedings of the 31st Intersociety Energy Conversion Engineering Conference*, vol. 1, August 1996, pp. 133-136.

8. Skvarenina TL, Pekarek S, Wasynczuk O, Krause PC, Thibodeaux RJ, Weimer J, "Simulation of a switched reluctance, More Electric Aircraft power system using a graphical user interface", *Proceedings of the 32nd Intersociety Energy Conversion Engineering Conference*, vol. 1, August 1997, pp. 580-584.

9. Weimer J. A, "Power management and distribution for the More Electric Aircraft", *Proceedings of the 30th Intersociety Energy Conversion Engineering Conference*, vol. 1, July 1995, pp. 273-277.

10. Weimer J. A, "Electrical power technology for the More Electric Aircraft", *12th AIAA/IEEE Digital Avionics Systems Conference*, October 1993, pp. 445-450.

11. Maldonado MA., Shah NM, Cleek KJ, Walia PS, Korba GJ, "Power management and distribution for the More Electric Aircraft (MADMEL)-program status", *Proceedings of the 31st Intersociety Energy Conversion Engineering Conference*, vol. 1, August 1996, pp. 148-153.

12. Maldonado MA., Shah NM, Cleek KJ, Walia PS, Korba G, “Power management and distribution for the More Electric Aircraft (MADMEL)-program status”, *Proceedings of the 32nd Intersociety Energy Conversion Engineering Conference*, vol. 1, August 1997, pp. 274-279.

13. Ponnappan P.R., “Efficient cooling of MCT and IGBT using venturi flow”, *Proceedings of the 30th Intersociety Energy Conversion Engineering Conference*, vol. 1, July 1995, pp. 561-568.

14. Homeyer W. G., “Advanced power converters for More Electric Aircraft applications”, *Proceedings of the 31st Intersociety Energy Conversion Engineering Conference*, vol. 1, August 1996, pp. 137-142.

15. Cheng K.W.E., “Comparative Study of AC/DC converters for More Electric Aircraft”, *Seventh International Conference on Power Electronics and Variable Speed Drives*, September 1998, pp. 299-304.

16. Reinhardt K. C., “Wide bandgap power electronics for the More Electric Aircraft”, *Proceedings of the 31st Intersociety Energy Conversion Engineering Conference*, vol. 1, August 1996, pp. 137-142.

17. Varshney U., “Monolithic magnetic modules for aerospace power electronics applications”, *Proceedings of the 32nd Intersociety Energy Conversion Engineering Conference*, vol. 1, August 1997, pp. 370-374.

18. Fronista G. L. “ An electromechanical actuator for a transport aircraft spoiler surface”, *Proceedings of the 32nd Intersociety Energy Conversion Engineering Conference*, vol. 1, August 1997, pp. 694-698.

19. Gribble J.J., “Feasibility study of a large switched reluctance spoiler actuator system”, *IEE Colloquium on All Electric Aircraft*, June 1998, pp. 6/1-6/13.

20. Fen Chan, Cai, X. S, “Multi-objective design optimization technique for switching regulators using mixed-discrete programming”, *Proceedings of the 20th Annual IEEE Power Electronics Specialists Conference*, June 1989, pp. 526-533.

21. Ridley R. B., Zhou. C., Lee. F. C., “Application of nonlinear design optimization for power converter components”, *IEEE Transactions on Power Electronics*, vol. 5. no. 1., January 1990, pp. 29-39.

22. Kragh H, Blaabjerg F, Pederson. J, “An advanced tool for optimized design of power electronic circuits”, *Conference Record of the 1998 IEEE Industry Applications Conference*, vol. 1, October 1998, pp. 991-998.

23. Hopkins D. C., Sarkar. M., Cull. R., “A mathematical approach to minimize the total mass of a space based power system by using multivariate non-linear optimization”, *Proceedings of the 29th Intersociety Energy Conversion Engineering Conference*, vol. 1, August 1994, pp. 185-189.

24. Moses, R. W, “Vertical Tail Buffeting Alleviation Using Piezoelectric Actuators-Some Results of the Actively Controlled Response of Buffet-Affected Tails (ACROBAT) program,” *Proceedings of SPIE’s 4th Annual Symposium on Smart Structures and Materials, Industrial and Commercial Applications of Smart Structures Technologies, Conference 3044*, San Diego, CA, March 4-6, 1997.

25. Clingman, J. D. “Drive Electronics for large piezoactuators,” *Proceeding of SPIE's 1997 North American Symposium on Smart Structures and Materials: Industrial and Commercial Applications of Smart Structures Technologies*, Janet M. Sater; Ed., Vol. 3044, San Diego, CA, March, 1997, pp. 459-467.

26. Clingman. D.J, Gamble. M, “High voltage switching power amplifiers [for helicopter blade actuator],” *Proceedings of the SPIE, The International Society for Optical-Engineering*, vol. 3326, 1998, pp. 472-8.

27. Zvonar, G. A., J. Luan, F. C. Lee, D. K. Lindner, S. Kelly, D. Sable, and T. Schelling, “High-Frequency Switching Amplifiers For Electrostrictive Actuators”, *Proceedings of SPIE's 1996 North American Symposium on Smart Structures and Materials: Industrial and Commercial Applications of Smart Structures Technologies*, C. Robert Crowe; Ed., Vol. 2721, San Diego, CA, February, 1996, pp. 465-475.

28. Zvonar, G. A. and D. K. Lindner, "Power Flow Analysis of Electrostrictive Actuators Driven by Switchmode Amplifiers," *Journal on Intelligent Material Systems and Structures,* special *issue on the 3rd Annual ARO Workshop on Smart Structures*, Vol. 9, 1998, No 3, pp. 210 - 222.

29. Zvonar, G. A. and D. K. Lindner, “Nonlinear Electronic Control of an Electrostrictive Actuator,” *Proceeding of SPIE's 1997 North American Symposium on Smart Structures and Materials: Industrial and Commercial Applications of Smart Structures Technologies*, Janet M. Sater; Ed., Vol. 3044, San Diego, CA, March, 1997, pp. 448-458.

30. Main, J. A, Garcia, E, Newton, D. V, “Precision position control of piezoelectric actuators using charge feedback,” *Journal of Guidance, Control and Dynamics*, Vol. 18, No. 5, Sep-Oct 1995, pp. 1068-1073.

31. Main JA, Garcia E. “Piezoelectric stack actuators and control system design: strategies and pitfalls”. Journal of Guidance Control & Dynamics, vol.20, no.3, May-June 1997, pp.479-85.

32. Newton, D. V, Main, J. A, Garcia, E., Massengill,L., “Piezoelectric actuation systems: optimization of driving electronics,” *Proceedings of SPIE’s 1996 North American Symposium on Smart Structures and Materials: Smart Structures and Integrated Systems*, Vol. 2717, San Diego, CA, February 1996, pp. 259-266.

33. Warkentin. D. J, Crawley. E.F, “Power flow and amplifier design for piezoelectric actuators in intelligent structures,” *Proceedings of the SPIE, The International Society for Optical-Engineering*, vol. 2190, 1994, pp. 283-94.

34. Leo, D.J., "Energy analysis of piezoelectric-actuated structures driven by linear amplifiers," *Proceedings of the Adaptive Structures and Materials Symposium*, ASME AD-vol. 59, November, Nashville, TN, 1999, pp. 1-10.

35. Liang C, Sun FP, Rogers CA, 1997, “Coupled electro-mechanical analysis of adaptive material systems-determination of the actuator power consumption and system energy transfer,” *Journal of Intelligent Material Systems & Structures,* vol.8, no.4, 1997, pp.335-43.

36. Liang C, Sun FP, Rogers CA., 1997, “Determination of design of optimal actuator location and configuration based on actuator power factor,” *Journal of Intelligent Material Systems & Structures,* vol.8, no.4, 1997, pp.344-52.

37. Middlebrook, R. D., “Input Filter Considerations in Design and Application of Switching Regulators,” *IEEE Industry Application Society Annual Meeting*, October 11-14, 1976, Chicago, Il.

38. Middlebrook, R. D., “Design Techniques for Preventing Input-Filter Oscillations in Switched-Mode Regulators,” *Proceedings of Powercon 5, The Fifth National Solid State Power Conversion Conference*, San Francisco, CA, May 4-6, 1978, , pp.A3/1-16.

39. Erich, Sandra Y., and William M. Polivka, “Input Filter Design Criteria for Current-Programmed Regulators,” *IEEE Transactions on Power Electronics*, vol. 7, No. 1, January 1992, pp. 143-151.

40. Jang, Yungtaek, and Robert E. Erickson, “Physical Origins of Input Filter Oscillations in Current Programmed Converters”, *IEEE Transactions on Power Electronics*, Vol. 7, No. 4, October 1992, pp. 725-733.

41. Lewis, L.R., B.H. Cho, F.C. Lee, and B.A. Carpenter, “Modeling, Analysis and Design of Distributed Power Systems,” *IEEE Power Electronics Specialists Conference,* 1989, vol I, pp. 152-159.

42. Florez-Lizarraga, Martin and A. F. Witulski, “Input Filter Design for Multiple-Module DC Power Systems,” *IEEE Transactions on Power Electronics*, Vol.11, No. 3, May 1996, pp. 472-479.

43. S. Hiti, V. Vlatkovic, D. Borojevic and F. C. Lee, “A New Control Algorithm for Three Phase PWM Buck Rectifier with Input Displacement Factor Compensation”, *Proceedings of the 11th VPEC Seminar*, September 1993, pp. 19-25.

44. Mao H, et al., “Novel reduced-order small signal model of three phase PWM rectifiers and its application in control design and system analysis”, *Proceedings of the 27th Power Electronics Specialists Conference*, June 1996, vol. 1, pp. 556-562

45. V. Vlatkovic, D. Borojevic and F. C. Lee, “Input Filter Design for Power Factor Correction Circuits”, *Proceedings of the IECON ’93*, November 1993, pp.954-958.

46. Mohamed Belkhayat, “Stability Criteria for AC power Systems with Regulated Loads”, *PhD Dissertation*, *Department of Electrical and Computer Engineering*, Purdue University, 1997.

47. S. Hiti, D. Borojevic, “Small-signal modeling and control of three-phase PWM converters”, *Proceedings of the 15th VPEC Seminar*, 1994, pp. 63-70.

48. Green, Limebeer, “Linear Robust Control”, *Prentice Hall Information and System Sciences Series*, 1995.

49. Gholdston E. W., et al., “Stability of large DC power systems using switching converters, with application to the International Space Station’, *Proceedings of the 31st Intersociety Energy Conversion Engineering Conference*, vol. 1, August 1996, pp. 166-171.

50. Abed, E.H. et al, “Stability and Dynamics of Power Systems with Regulated Converters”. *Proceedings of the IEEE Symposium on Circuits and Systems*, vol. 1, 1995, pages 143-145.

51. Belkhayat, M. et al, “Large Signal Stability Criteria for Distributed System with Constant Power Loads, *Proceedings of the 26th Annual IEEE Power Electronics Specialists Conference*, Atlanta, GA, 1995, pages. 1333-1338.

52. Ashton R. W., et al., “The design and fabrication of a reconfigurable hardware testbed for the interaction analysis of power converters in a reduced-scale Navy dc distribution system, *Proceedings of the IEEE Symposium on Circuits and Systems*, vol. 3, 1998, pp. 379-382.

53. M. Al-Fayyoumi, “Nonlinear dynamics and Interaction in Power Electronics Systems”, *M.S. Thesis, Department of Electrical and Computer Engineering*, Virginia Tech, 1998.

54. Wang, K, Chandrasekaran, S., and Cuadros, C., et al., “Quasi-Single Stage Three phase ZVZCS PWM Buck Rectifier”, *Virginia Power Electronics Center-Project Report submitted to Ericsson Components*, Sweden, March 1999.

55. Vanderplaats, G.N., *Numerical Optimization Techniques for Engineering Design: With Applications*, Vanderplaats R&D Inc., Colorado Springs, CO, 1988.

56. Haftka, R.T., and Gürdal, Z., *Elements of Structural Optimization, Third Revised and Expanded Edition*, Kluwer Academic Publishers, Dordrecht, 1992, pp. 182-186.

57. J. G. Kassakian, M. F. Schlecht, G. C. Verghese, “Principles of Power Electronics”, *Addison-Wesley*, 1991.

58. Ogata. K, “Modern Control Engineering”, *Prentice Hall, Eastern Economy Edition*, 1986.

59. Smith R.C, and C.L. Hom,. “A Domain Wall Model for Ferroelectric Hysteresis”, *Proceedings of SPIE, The International Society for Optical Engineering,* Vol.3667, 1999, pp.150-61.

60. Mohan N., T.M. Undeland, and W. Robbins, “Power Electronics-Converters, Applications and Design”, *John Wiley and Sons*, 1995.

61. Nayfeh,A.H, “Applied nonlinear dynamics”, *John Wiley*, 1995

62. Seydel Rudiger, “From Equilibrium to Chaos”, *Elsevier Science Publishing*, 1988.

63. Dobson. I, Alvarado F, De Marco C. L, “Sensitivity of Hopf Bifurcations to Power System Parameters”, *Proceedings of the 31st Conference on Decision and Control,* Arizona, December 1992, pp. 2928-2933.

64. Dobson. I., “Computing a Closest Bifurcation Instability in Multidimensional Parameter Space,” *Journal of Nonlinear Science*, Vol. 3, 1993, pp. 307-327.

65. Leonhard Werner, “Control of Electrical Drives”, *Springer*, 1997.

VITA

Sriram Chandrasekaran was born in Calcutta, India on January 23, 1972. He obtained in Bachelor of Engineering degree in Electrical and Electronics Engineering from the PSG College of Technology, Coimbatore, India in 1993 and his Master's degree (M.Sc. (Engg.)) in Electronics Design Technology from the Indian Institute of Science, Bangalore, India in 1995. He started his PhD program at Virginia Tech in the fall of 1995 as a graduate research assistant at the Center for Power Electronics Systems. His research interests are in the areas of optimization, distributed power systems, nonlinear stability analysis, piezoelectric actuators and digital control of power converters and motor drives. He will join the Rockwell Science Center at Thousand Oaks, California as a Member of the Technical Staff on graduation from Virginia Tech.